Risk Assessment and Safety Analysis of Fuel Rods in Pressurized-Water Reactors (PWRs)

by

Kisik Hong

A dissertation submitted in partial fulfillment
of the requirements for the degree of
Doctor of Philosophy
(Mechanical Engineering)
in the University of Michigan
2020

Doctoral Committee:

Professor Wei Lu, Co-Chair
Professor Michael Thouless, Co-Chair
Professor James R. Barber
Professor Jason McCormick

Kisik Hong

kisik@umich.edu

ORCID iD: 0000-0003-1132-4396

Dedication

To my parents

To my friends

Acknowledgement

First of all, I deeply appreciate my advisors Professor Michael Thouless, Professor Wei Lu, and Professor James Barber for their sincere advices and guidance throughout my graduate years. I would like to appreciate all your encouragement and contributions of time to my research. It has been an honor to be a Ph.D. student of yours. I would also like to thank Professor Jason McCormick for helpful discussions with insightful questions and comments.

I would like to appreciate the CASL program (http://www.casl.gov), an Energy Innovation Hub (http://www.energy.gov/hubs) for Modeling and Simulation of Nuclear Reactors under U.S. Department of Energy, for the financial and technical support over my graduate years.

I would also thank my colleagues Isha and Dandan not only for the insightful discussion on the research but also for the delightful moments we shared. In retrospect, My Ph.D. life at University of Michigan was one of the most enjoyable and blissful part of my life. I am grateful to all individuals who have supported and encouraged me throughout my Ph.D. period.

Lastly, I would like to express my deepest gratitude to my family for all their love and encouragement. Without the mental and emotional supports of my parents, I could not finish my Ph.D successfully. Thank you.

Table of Contents

List of Figures

Abstract

In pressurized-water reactors (PWRs), the mechanical integrity of claddings should be ensured under various loading conditions to avoid exposure of hazardous nuclear fission products to the external environment. In light of this, several problems associated with the possible failure of the cladding were studied as follows.

Cracking and spalling of the oxide layer developed under normal operation on Zircaloy-4 cladding, associated with the localized development of hydride in the cladding, were studied. Through finite-element simulations, it was found that the tensile hoop stresses develop in the outer region of the oxide after a critical thickness. The conditions for the propagation of radial cracks perpendicular to the interface, channeling along the axial direction of the cladding, and the possible subsequent spalling of the oxide, was then determined using linear-elastic fracture mechanics (LEFM). Crack channeling could be classified into three different cases, depending on the thickness of oxide layer. Finally, the spalling analysis indicated that spalling leaves a thin layer of the oxide adhered to the cladding.

An analysis was conducted for the cracking of Cr-coated Zircaloy claddings, proposed for use in accident-tolerant fuels (ATF) to reduce hydride embrittlement of bare Zircaloy claddings. Through finite-element calculations, it was found that uniform tensile hoop stresses within the Cr-coating layer develop by pellet-cladding interaction (PCI). The energy-release rate for crack channeling was then compared with the toughness of Cr to develop a design map for the critical coating thickness below which fracture will not occur at different levels of ramped power. In addition, a design protocol was proposed, which allows a simplified fracture analysis of Cr coating

using existing PCI codes. This provides a design option without the need for constructing a full finite-element modelling of the cladding and coating.

The PCI under various power histories was studied, focusing on the evolution of local hoop stresses developed at the inner surface of cladding in the vicinity of fuel cracks. If PCI is initiated either before power ramping or during the transient period of a power ramps, the local hoop stress becomes tensile, which may lead to PCI failure. On the other hand, if PCI occurs during the normal operation or steady-state portions of a power ramp, the local hoop stress becomes compressive, which suppresses possible PCI failure. These results indicate that the power history has a significant effect on possible PCI failure, which can give an insight into developing safety criteria for operation of reactors.

As part of the of analysis of PCI, the fundamental contact mechanics associated with the local stress field near the corner of contact was studied. The influence of material dissimilarity on the traction fields at the contact corners between an elastic right-angle wedge and an elastic half-plane was studied through an asymptotic analysis. It was found that possible material combinations could be classified into two distinct categories. Through asymptotic analysis, a critical friction coefficient was found at which a discontinuous change from singular to bounded local fields occurs at the leading edge. Through the finite-element simulation, it was found that the contact region shrinks to zero at the critical friction coefficient, implying the existence of a concentrated force, while the singular field associated with a point contact is retained with a further increase in the friction coefficient.

Chapter 1 Introduction

1.1 Overview

Nuclear energy provides about 11% of the world's electricity from about 450 power reactors. It is the second largest source of low-carbon power which doesn't emit greenhouse gases, such as carbon dioxide or methane, which are known for depleting Earth's atmosphere. Nuclear energy also has a large power-generating capacity and low operating costs. However, life-threatening accidents may occur if the hazardous nuclear fission products are exposed to the external environment. There is a past history of nuclear accidents, such as Three Mile Island disaster in the United States, Chernobyl disaster in the USSR, and Fukushima disaster in Japan, which are beyond-design basis or non-design basis accidents. Therefore, it is important to ensure the safety of reactor systems; this has been a major concern for plant operators.

Among different types of nuclear reactors, pressurized water reactors (PWRs) constitute the large majority of the world's nuclear power plants (about 65 %). Inside the reactor vessel of a PWR, there is a bundle of fuel rods, consisting of fuel pellets, which generate energy through fission of atoms, and the cladding that contains the fuel pellets. If the cladding fails during the operation of a reactor, which has been observed occasionally in the past after a severe power uprating, the primary coolant can be exposed to the nuclear fission products.

Based on this background, various problems associated with the possible failure of the cladding was studied as follows. First, the cracking and spalling of oxide layer developed at the outer surface of the cladding during normal operation was investigated. Although Zircaloy is a

material which exhibits relatively good oxidation resistance, a thick oxide layer can be developed at the external surface of the cladding at high burn-up. Then, if the mechanical integrity of the oxide is damaged by cracking and spalling, local embrittlement of cladding can occur near the spalled area. In line with these observations, I study how these failures of oxide occur, particularly during the normal operation, which is the focus of Chapter 2.

Second, the cracking within the coating layer of a Cr-coated Zircaloy cladding is investigated. To resolve the problem of hydride embrittlement of the cladding, a transition is occurring from traditional cladding to more accident-resistant cladding, termed accident-tolerant fuel (ATF) cladding. Among various candidates for ATF claddings, Cr-coated Zircaloy cladding has been considered as a near-term deployment option. However, owing to the brittle characteristics of Cr metal, cracks may occur during the operation of a reactor, leading to pitting corrosion of underlying Zircaloy. It then results in serious mechanical degradation of the cladding owing to hydride embrittlement. Therefore, a fracture analysis of the coating layer under normal operation and power ramping conditions is performed, which is the focus of Chapter 3.

Third, the pellet-cladding interaction (PCI) is studied associated with various power histories, including normal operation and power-ramping conditions. During the early stage of operation, a high thermal gradient is generated within the fuel, which leads to fuel fragmentation. The cracked pellet then makes contact with the cladding owing to fuel swelling and creep-down of the cladding. As a result, a local hoop stress is developed at the inner surface of the cladding in the vicinity of fuel cracks, which can cause a serious cladding failure (PCI failure). Since the phenomena involved in the PCI have different time-scales, and since frictional contact problems are inherently history-dependent, different loading histories can lead to different results. I therefore

investigate how the local hoop stress can be quantitatively different depending on different types of power history, which is the focus of Chapter 4.

Finally, the fundamental contact mechanics related to the PCI problem discussed above is studied. If an elastic body with a sharp corner is pressed against an elastic half-plane, the stress field near the corner can be characterized by an asymptotic or eigenfunction series. Previously, there have been lot of studies which deal with the asymptotic stress field. However, most of these studies have been restricted to the case of elastically similar materials, whereas contact between engineering components can occur between elastically dissimilar materials. I therefore examine the effect of elastic mismatch on the asymptotic stress field. This is discussed in Chapter 5. Through asymptotic analysis, it was found that there exists a critical friction coefficient at which a discontinuous change in the local stress field occurs at the leading edge, which has not been reported previously. Therefore, I explore this phenomenon, which seems counter-intuitive, by implementing finite-element analysis. This is the focus of Chapter 6. In the following subsections, the main contents of each chapter are briefly introduced.

1.2 Cracking and spalling of the oxide layer developed in Zircaloy-4 cladding under normal operating conditions in a PWR

The evolution of cracks from the surface of a thick oxide layer on Zircaloy-4 cladding has been analyzed for the normal operation of pressurized-water reactors. The conditions for the propagation of radial cracks towards the interface, channeling along the axis of the cladding, and the possible subsequent spalling of the oxide have been studied. The analysis was conducted by first calculating how the stresses in the oxide developed during operation, using a numerical model that incorporates multiple mechanisms such as creep, swelling and oxidation. These calculations demonstrate that the circumferential stresses within the oxide increase as oxidation proceeds, and

as the cladding expands under the effect of fuel swelling. Although the intrinsic growth stresses of the oxide are compressive, tensile stresses can eventually develop in the outer region of the oxide. Within this regime, the energy-release rate for the radial propagation of a crack was determined using the *J*-integral, along with the calculated stress profile. By assuming a suitable value of toughness for the oxide, it is possible to determine the depth to which such a radial crack can grow. A second fracture-mechanics calculation was then conducted to explore the conditions under which such a surface crack can subsequently channel along the axial direction of the cladding. A third fracture-mechanics analysis considered the possibility of oxide spalling. This showed the possibility of spalling from the radial cracks, leaving a thin layer of the oxide adhered to the metal that could result in a local cold spot responsible for hydride formation.

1.3 Cracking of Cr-coated accident-tolerant fuel during normal operation and under power-ramping conditions

An analysis is presented for the cracking of Cr-coated Zircaloy claddings proposed for use in accident-tolerant fuels (ATF). Tensile hoop stresses are induced in the coating by pellet-cladding interaction (PCI), which results from the fuel swelling under normal operation, or from additional thermal expansion of the fuel after power ramping. The hoop stress is limited by the stress relaxation associated with dislocation glide that dominates the thermal creep in the coating. The energy-release rate for crack channeling has also been calculated, and it increases almost linearly with the thickness of the coating. By comparing this energy-release rate with the toughness of Cr, I can develop a design map for the maximum coating thickness required to avoid fracture at different levels of ramped power. I also propose a design protocol for coatings based on a simplified fracture analysis, which allows existing PCI codes to be leveraged.

1.4 Effect of power history on pellet-cladding interaction

The mechanical pellet-cladding interaction (PCI) is studied under various power histories. I find that the power history significantly affects possible PCI failure. PCI during the thermal transient period of power ramping occurs in such a way that crack-mouth opening increases regardless of when contact is initiated, before or during power ramping. The crack-mouth opening continues to increase further during the thermal steady state (during the power ramp). Conversely, PCI initiated either during the thermal steady-state power ramp or during the normal operation (with no power ramp) leads to decrease in crack-mouth opening. As a consequence, PCI initiated before power ramping or during the transient period of power ramping leads to high local tensile hoop stress. In contrast, PCI initiated during the thermal steady state of power ramping or during the normal operation without power ramping leads to local compressive hoop stress. In the former case, PCI failure near the crack tip might be anticipated (by either brittle failure during the transient power ramp or failure during the steady-state power ramp), whereas in the latter case, it is suppressed.

1.5 Asymptotic stress fields for complete contact between dissimilar materials

I investigate the influence of material dissimilarity on the traction fields at the corners of a contact between an elastic right-angle wedge and an elastic half-plane. The local asymptotic fields are characterized in terms of the properties of the leading eigenvalue for cases of slip and stick as a function of the Dundurs bimaterial parameters α and β, and the coefficient of friction f. Permissible values of α and β are partitioned into two possible ranges, one where behaviour is qualitatively similar to the case where the indenting wedge is rigid $[\alpha = 1]$, and one where

behaviour is similar to the case where the materials are the same [$\alpha = \beta = 0$]. The results give insight into the high local stresses at the edge of a contact between elastically dissimilar bodies, and can also be used to evaluate the effectiveness of mesh refinement in corresponding finite-element models.

1.6 Corner stress fields in sliding at high friction coefficients

If an elastic body with a sharp corner slides over an elastic half-plane, the stress and displacement fields near the corner can be characterized by the leading term in an asymptotic [eigenfunction] series. However, there exists a critical friction coefficient $f = f_d$ at which an infinitesimal increase in f appears to imply a discontinuous change from singular to bounded local fields at the leading edge. Here, I show that this conclusion is incorrect. Instead, the contact region shrinks to zero at $f = f_d$ implying the existence of a concentrated contact force, but the singular field associated with point contact is retained for $f > f_d$. I also show that a non-linear solution using a Generalized Neo-Hookean constitutive law gives the same conclusion, and that the concentrated force generated is well predicted by the linear analysis. However, in contrast to the linear solution, the total strain energy in the non-linear solution is bounded.

Chapter 2 Cracking and Spalling of the Oxide Layer Developed in Zircaloy-4 Cladding Under Normal Operating Conditions in a PWR

2.1 Introduction

The exterior surfaces of fuel rods are exposed to the primary coolant during operation of a pressurized-water reactor (PWR). This results in oxidation of the Zircaloy cladding. A complementary process to oxidation is the formation of hydrogen, which in some cases can diffuse into the Zircaloy and form brittle hydrides. These hydrides tend to precipitate out in colder regions of the cladding [1]. Since the oxide layer serves as a thermal barrier against the coolant, local cold spots are formed where hydrides may precipitate [2], if the integrity of the oxide is compromised by cracking or spalling. Since the ductility of Zircaloy decreases dramatically with an increase in hydride [3, 4], the spalled area can become vulnerable to what is termed pellet-cladding-interaction (PCI) [5] failure. The intent of this study is to explore the mechanics of how an oxide layer might crack and spall as a result of mechanical interaction between the pellet and cladding during normal operation of a reactor. It is important to appreciate that this is a study of the radial cracks and spalls that can develop when the oxide is thick. It is not a study of the defects that appear to align parallel to the interface during early stages of oxidation, which are sometimes equated to cracks, despite the absence of significant radial tensile stresses or obvious signs of buckling.

An insight into the process is given by the results of the CABRI REP-Na program, performed by the French Institut de Radioprotection et de Sûreté Nucléaire (IRSN) in the early 90's to study what is termed a reactivity-initiated accident (RIA) with irradiated fuel rods [6–9].

An RIA corresponds to a rapid power transient in a fuel rod over a few milliseconds. This leads to extreme swelling of the fuel pellet, and a strong interaction between the pellet and cladding that can result in oxide spalling. Various efforts have been made to improve the understanding of oxide spalling during an RIA. For instance, studies were conducted to analyze the phenomenon, based on metallographic investigations of the CABRI REP-Na test rods that exhibited spalling [10, 11]. Cracking of the oxide layer was explained by implementing a shear-lag model, with a tensile circumferential stress being generated in the cladding and oxide layer because of the swelling of the pellet against the cladding, and being transferred to the oxide layer. Also, finite-element calculations were performed by assuming a partially fragmented oxide layer, with further fragmentation being assumed to occur during the power transient when the circumferential stress in the oxide reached an assumed critical value.

These analyses concentrated on the cracking and spalling of the oxide layer during a transient power spike. The simulations were conducted with pre-oxidized claddings, and the characteristics of the oxide layer that can form on fuel rods during long service in a reactor were neglected. However, the stress in the oxide layers of heavily corroded fuel rods can be quite significant, and spalling was observed on some test rods, which consists of standard Zircaloy-4 (1.5% Sn) cladding and UO_2 fuel, under normal operating conditions, before being subjected to the RIA transient [19].

It is the possible development of stresses and subsequent crack evolution in the oxide layer under normal operating conditions, rather than spalling under an RIA transit, that is studied in the present chapter. The model we present incorporates essential mechanisms such as creep, swelling, and oxidation into a finite-element simulation. A cracking analysis is performed based on the stress distribution that is obtained from the model. In contrast to the previous analysis that invoked the

concept of a fracture strength for a brittle material, we implement a more rigorous fracture-mechanics-based approach to describe the propagation of cracks within the oxide layer.

2.2 Model

The analysis of cracking in the oxide layer consists of three steps: (i) obtaining the stress state within the oxide, (ii) using this stress distribution to calculate the depth to which an incipient flaw may grow, and (iii) computing the conditions for when this flaw can channel along the oxide to form a significant crack. Therefore, three separate finite-element calculations were conducted sequentially. The first of these captured the stress evolution within the oxide layer during service, while the other two were fracture-mechanics calculations.

2.2.1 Development of stress in the oxide layer

2.2.1.1 Geometry and boundary conditions

A finite-element model for the fuel rod, including the fuel pellet and cladding, was constructed using the commercial software program, ABAQUS. As shown in Fig. 2-1, a simplified, axisymmetric model was implemented, based on the approximate dimensions of a fuel rod in a PWR. First-order, coupled temperature-displacement, axisymmetric elements with reduced integration were used in an implicit calculation. During the simulation, the displacement and temperature fields were solved simultaneously using nonlinear thermomechanical calculations, to ensure an appropriate relationship between them.

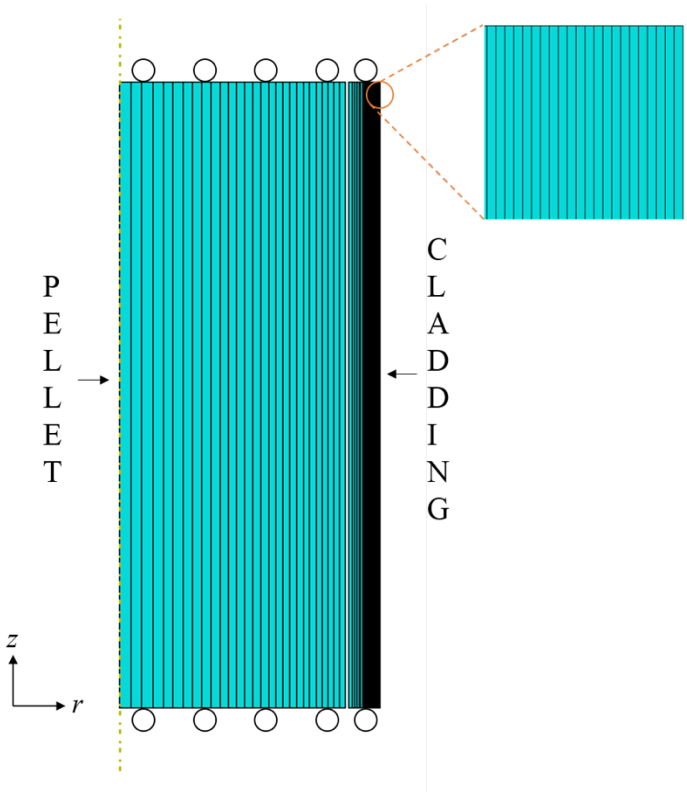

Figure 2-1: A simplified axisymmetric model for the fuel rod including fuel pellet and cladding. Dimensions are implemented based on approximate values for a fuel rod in a PWR. The displacement along *z*-direction was constrained. There is an internal pressure between the pellet and cladding because of helium gas, and an external pressure outside of the cladding because of the primary coolant.

The displacements along the axis of the cylinder corresponding to the fuel rod (the *z*-direction) were constrained so that the results varied only along the radial *r*-direction, and the analysis was axisymmetric. An initial gap of 80 μm between the pellet and cladding was assumed to be filled with helium gas. The pressure of this internal gas was set to 4 MPa, and a pressure of 16 MPa associated with the primary coolant [22] was applied to the outer surface of the cladding. Any contact between the pellet and cladding was assumed to be axisymmetric, with a normal-hard-contact, finite-sliding, and surface-to-surface formulation. To prevent penetration between the surfaces, the direct method was used for enforcing the constraint in the normal direction.

Thermal boundary conditions were established by assuming that the fuel rod was initially at 300 K. A uniform power generation of 20 kW/m, a typical value for a PWR [23], was applied to the fuel as a body heat flux. The temperature of the outer surface of the cladding was held at a constant value of 600 K, corresponding to the temperature of the primary coolant.

2.2.1.2 Model of oxidation and other deformation mechanisms

Oxidation of zirconium leads to an increase of volume, the ratio of the oxide volume to the corresponding volume of the metal (the Pilling-Bedworth ratio) being 1.56 [24]. If the unconstrained volume increase is assumed to be isotropic and the material behaviour elastic, constraint by the metal substrate would result in unrealistically high in-plane compressive stresses (around 56 GPa) immediately after oxidation. Many experiments have been designed to estimate the stress in zirconium oxide layers, based on curvature measurements [25], XRD [16, 17], and Raman spectroscopy [28]. These authors report experimental values of in-plane compressive stress in the range 2 ± 0.2 GPa at the early stages of the oxidation, implying that yield has occurred immediately after oxide formation. We therefore assume that the newly formed oxide starts from a condition of in-plane compressive stress at 2 GPa. For the simulation, this was achieved by assigning an appropriate in-plane initial strain in the oxide layer. Out-of-plane strain, associated with the dimensional change in radial direction, was assigned so as to maintain the correct Pilling-Bedworth ratio.

In the model, the area near the outer surface of the cladding was partitioned into fine elements, each of equal thickness as in Fig. 2-1. The oxidation process was incorporated into the simulation by the following steps. First, the oxide interface was assumed to advance by the thickness of one element, and the material properties of the element were changed from those of Zircaloy to those of zirconia. This was implemented into the calculation using field variables with

the USDFLD subroutine. Eigenstrains described above were assigned to the transformed element, using the UEXPAN subroutine. Second, creep, thermal expansion and swelling, as appropriate, of the UO_2 pellet, Zircaloy, and oxide layer were implemented through the UEXPAN and CREEP subroutines. The time steps for the calculations were determined by dividing the element thickness by the oxidation rate corresponding to the current oxide thickness. The process was repeated for each subsequent layer of elements as oxidation proceeds. The appropriate thickness of the elements was determined by a mesh-sensitivity test. It was found that a mesh size of 1 μm for the particular geometry and conditions used in this study was more than adequate to ensure convergence of the stresses in the oxide to a mesh-independent value, within acceptable limits of numerical uncertainty.

Zircaloy exhibits cubic oxidation with periodic breakaway [29], resulting in an approximately constant oxidation rate [20, 21]. The appropriate oxidation rate for Zircaloy-4 was estimated from experimental data [19], which indicates that the oxide grows to about 80 μm after 54 months at a burn-up level of 60 GWd/t, corresponding to a rate of 1.48 μm/month.

The creep calculations for Zircaloy-4 were based on a recent deformation-mechanism map that was developed from many decades of experimental creep data [32]. The creep parameters for UO_2 were taken from an earlier deformation-mechanism map [33]. The creep models for both Zircaloy and UO_2 incorporated multiple creep mechanisms, including dislocation creep, diffusional creep, and power-law creep. The numerical approach developed in Ref. [32] was used, whereby micromechanics models were incorporated into the FEM code, allowing all possible creep mechanism to act simultaneously, with the dominant mechanism evolving naturally as a function of local stress and temperature. Obtaining suitable parameters for creep of the oxide was more difficult owing to the lack of appropriate experimental studies. The only available

experimental data appear to be for yttria-stabilized zirconia [24–26], focusing on diffusional creep at relatively high temperatures ($T > 1200\,\mathrm{K}$) and low stresses ($\sigma < 300\,\mathrm{MPa}$). Using the parameters from these studies, it appears that creep of the oxide may have a negligible effect on the evolution of stresses within it, so oxide creep was ignored in these calculations. While it is noted that this neglect of oxide creep may influence the details of the stresses in the oxide, the broader conclusions of the results presented here will not be affected.

The grain sizes of the Zircaloy, UO_2 and zirconia (where needed for the creep calculations) were assumed to be 50 μm, 10 μm and 25 nm, respectively. In addition, the model for swelling of UO_2, which arises from the accumulation of fission products within the pellet, and the thermal conductivity of the helium in the gap between the pellet and cladding were taken from the MATPRO model [37]. Other parameters needed for the analysis, including the elastic properties, specific heat, density, thermal conductivity, and thermal expansion coefficients were also taken from MATPRO [37].

2.2.2 Analysis of the oxide fracture

2.2.2.1 Geometry and boundary conditions

The geometry of the cladding corresponding to a fixed time and thickness of oxide was imported into a new model to calculate the fracture mechanics. In the geometry for this model, a radial surface crack was assumed to extend from the surface to a depth *a* within the oxide. It was assumed that the length of this crack along the axis of the cladding was much greater than the crack depth, so a two-dimensional model, as in Fig. 2-2, could be used. The calculations were performed under plane-strain conditions, with crack-tip elements and a refined mesh being used near any prospective contact areas, to improve their accuracy. The material properties were assigned fixed values appropriate for a temperature of 600 K.

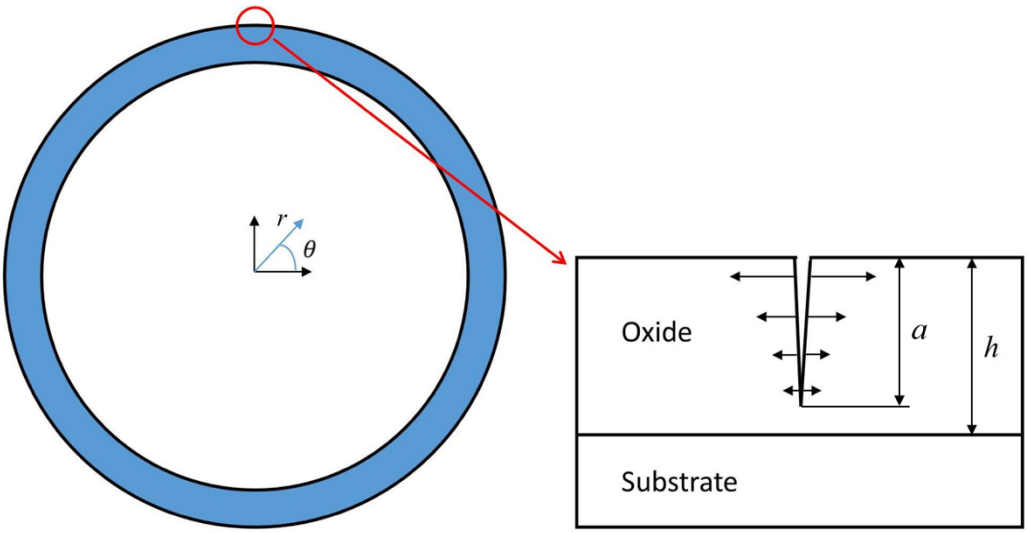

Figure 2-2: A 2D model of cladding in the r-θ plane with a radial crack introduced to the oxide layer of thickness h at $\theta = 90°$ (left). The radial crack is subjected to an internal pressure corresponding to the stress calculated from the uncracked model (right). This configuration is used to calculate the strain-energy values for the cracking analysis.

Since, the calculations in this section were concerned with the energetics of brittle fracture, creep was not included in the fracture calculations. The radial distribution of circumferential stresses at the corresponding time of interest was imported from the analysis described in the previous section. This distribution was represented as a function of radial position by using a polynomial fit, and was applied as tractions (of the opposite sign) to both surfaces of the crack, using the subroutine DLOAD. Only mode-I fracture was considered since no shear stresses were developed along the plane of the crack within the oxide. This approach of representing a residual stress distribution by a corresponding traction over the crack surface is a well-established technique in fracture mechanics to calculate crack-driving forces that can be used to assess the propensity of a coating or layer to fracture under residual stresses.

2.2.2.2 Fracture-mechanics calculations

Two distinct calculations are required to compute the conditions for crack channeling in a coating with a varying distribution of stresses. The first is to compute the depth to which a radial

crack might grow perpendicular to the surface (Fig. 2-3a). The second is to compute whether a crack of this depth can channel along the film, parallel to the surface (Fig. 2-3b).

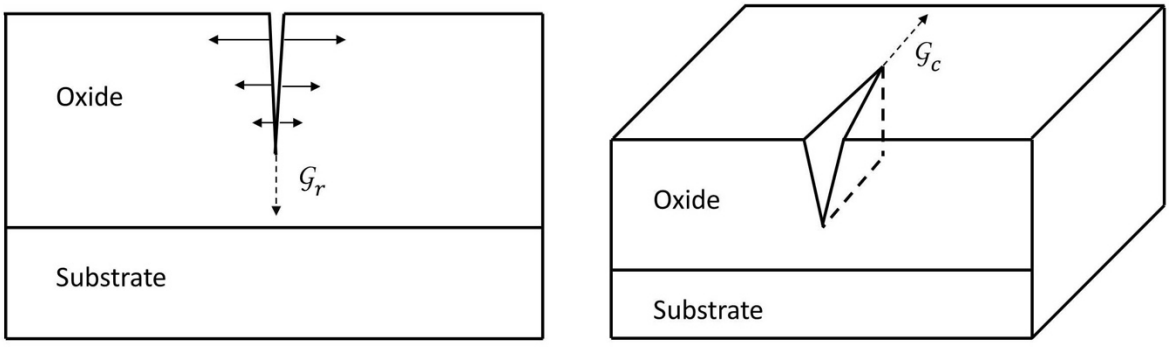

(a) (b)

Figure 2-3: The geometry considered for the crack analysis. (a) The propagation of a radial crack towards the metal-oxide interface (b) The propagation of a channeling crack in the axial direction along the oxide.

The energy-release rate for radial growth was determined by calculating the value of the *J*-integral associated with a crack with the corresponding tractions on its surface. The equilibrium depth can then be computed by finding the crack depth for which the energy-release rate equals the toughness of the oxide. Once the depth to which a surface crack could grow in a radial direction has been established, the conditions for channeling along the length of the cladding (Fig. 2-3b) were computed by a second analysis. Calculations for the energy-release rate of steady-state channeling along a coating can be done by one of two approaches. One approach is to compare the elastic strain energies between an uncracked region far ahead of the channel crack (Fig. 2-4a) and a cracked region (Fig. 2-4b) far behind the crack tip [38]. An alternative, and more direct, approach that we use here, is to compute the energy-release rate from the work done by the equivalent tractions on the surfaces of the crack that correspond to the circumferential stress being relaxed by the crack, as illustrated in Fig. 2-4c [39]. The conditions for whether channeling occurs or not can then be computed by comparing this energy-release rate to the toughness of the oxide.

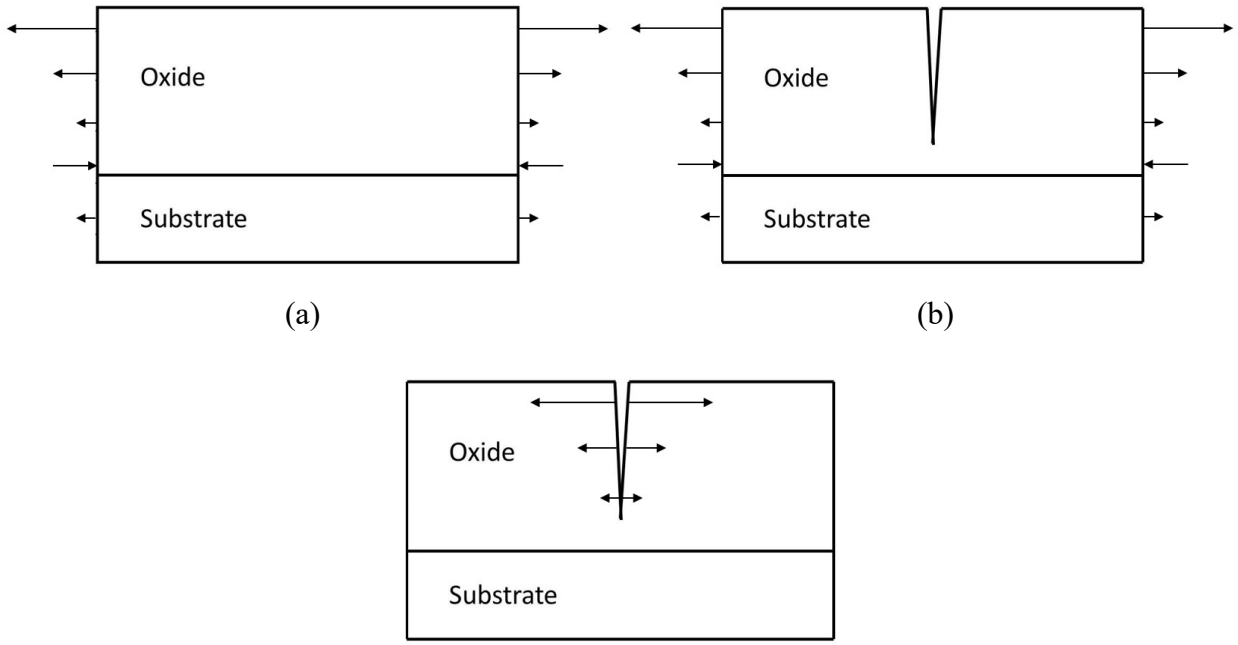

Figure 2-4: The geometry considered for the crack-channeling analysis. (a) The configuration of an uncracked region far ahead of the channel crack. (b) The configuration of a cracked region. (c) The configuration of a crack with an internal pressure which corresponds to the stress field in the uncracked configuration. The difference in elastic energy, (a) – (b), can be directly calculated with (c).

Unfortunately, values for the toughness of the oxide appear to be focused on the toughened structural material of yttria-stabilized zirconia [30, 31], which may not be very relevant to a thermal oxide. Therefore, the fundamental results have been presented in terms of the energy-release rates. We have subsequently provided an illustrative example using an estimated value for the toughness that would be typical for a ceramic. But, it is a fairly simple exercise for a reader who may have access to more definitive data to calculate what would happen with different values of toughness. In particular, we note that the broad conclusions are not affected by the details of the toughness. The conditions for cracking, channeling and spalling are met over a relatively narrow window of oxide thickness for a broad range of toughness values.

2.3 Results and discussion

2.3.1 Development of stresses in the oxide layer

2.3.1.1 Contact between the fuel and cladding

During the initial assembly of a fuel rod, there is a gap of about 80 μm between the fuel pellet and the interior surface of the cladding. This gap reduces to about 46 μm immediately after the fuel rod enters service, owing to thermal expansion and the elastic effects induced by the pressure of the coolant acting on the outer surface of the cladding. During service, fission products lead to swelling of the fuel pellet, while creep leads to shrinkage of the cladding. Both of these effects cause the gap to decrease with time and, eventually, close. Further swelling of the fuel pellet then increases the contact pressure, and the pellet pushes the cladding radially outward. Under the influence of this swelling, the cladding expands by creep of the Zircaloy. It is this creep of the Zircaloy that can eventually lead to fracture of the oxide. Using the parameters and models discussed in Section 2.2.2.1, finite-element results for how the gap and contact pressure evolve with time are given in Fig. 2-5.

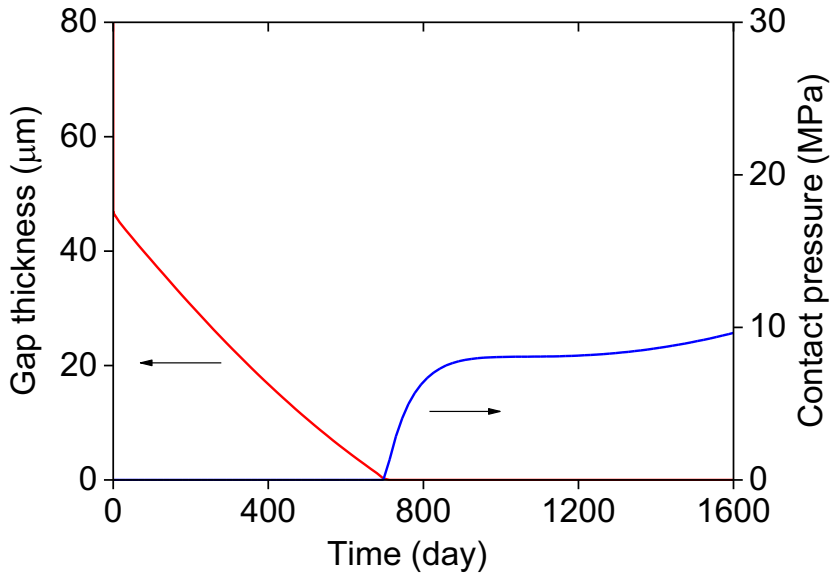

Figure 2-5: Evolution of the gap thickness and contact pressure with time

2.3.1.2 Stress in the oxide layer

The effect of interactions between creep, fuel swelling and oxidation can be seen in the plot of Fig. 2-6, which shows how the circumferential stress in the outer layer of the oxide changes as oxidation proceeds to a thickness of 100 μm. Initially, the stress in the outer layer is dominated by the compressive growth stress, and the creep-down of the cladding increases the magnitude of the compression. However, once contact between the fuel pellet and the cladding occurs, the outwards expansion of the cladding contributes to the development of tension in the outer regions of the oxide.

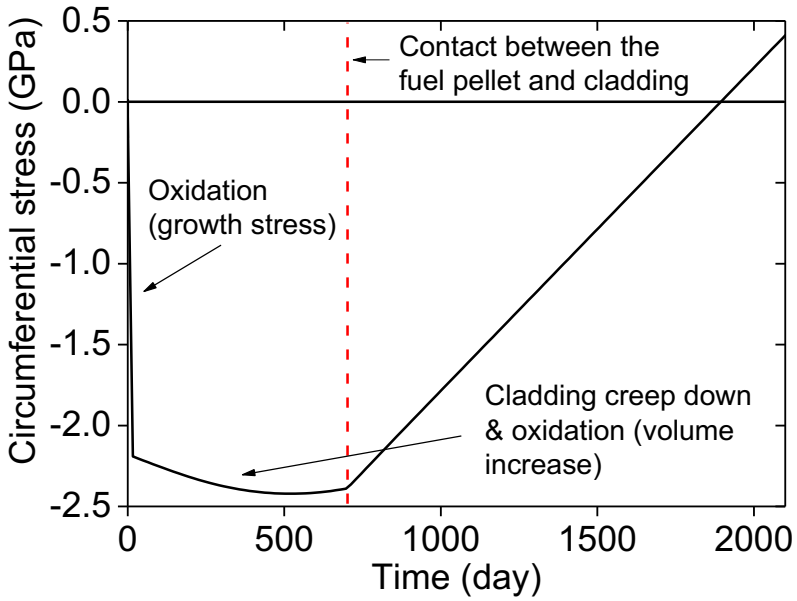

Figure 2-6: Development of the circumferential stress at the outermost oxide surface with time until the oxide thickness reaches 100 μm.

Besides the above mechanisms, there are less obvious phenomena that induce changes in the stress in the outer regions of the oxide. Immediately after the fuel rod goes into service, thermal expansion increases the circumferential stress at the outer surface of the cladding, while elastic effects resulting from the external pressure reduce the stress. Since the effect of the coolant

dominates over that of thermal expansion, the outermost surface of the cladding becomes slightly compressive before oxidation occurs. The increase in volume associated with the formation of new oxide at the interface with the metal forces the outer oxide layers outwards, in the radial direction. This generates circumferential tension within the outer layers. A separate calculation showed that this contribution to the accumulation of the tensile stress in the outermost layer of the oxide is about half the contribution from the fuel swelling for an oxide layer with a thickness of 100 μm.

The radial distribution of the circumferential, $\sigma_{\theta\theta}$, and axial, σ_{zz}, components of the stresses, when the oxide layer is 100 μm thick, is shown in Fig. 2-7. This illustrates a tensile circumferential stress of just under 0.5 GPa at the outmost surface of the oxide layer, as seen in Fig. 2-6, after the corresponding length of time. Figure 2-7 also illustrates how the circumferential stress varies with thickness. There is a large compressive stress associated with growth at the metal-oxide interface, and the circumferential stress becomes tensile at about 40 μm away from the interface. Similar plots for how the circumferential stress varies with radial distance from the metal-oxide interface at different stages in the oxidation process are shown in Fig. 2-8 for oxide layers in the range of 80 to 120 μm thick. It will be seen from this figure that if the oxide is thicker than about 80 μm, sub-surface regions of tensile stresses develop, whereas if the oxide is thicker than about 90 μm, the outer region of the oxide layer also develops tensile circumferential stresses. In even thicker oxides, the tensile stresses become quite large. It will be shown in the following section that the tendency for the oxide film to crack increases dramatically above a critical thickness. There is a narrow range of thicknesses below which any reasonable value of oxide toughness would not lead to cracking, and above which any reasonable value of oxide toughness would lead to extensive crack channeling, multiple cracking, and spalling.

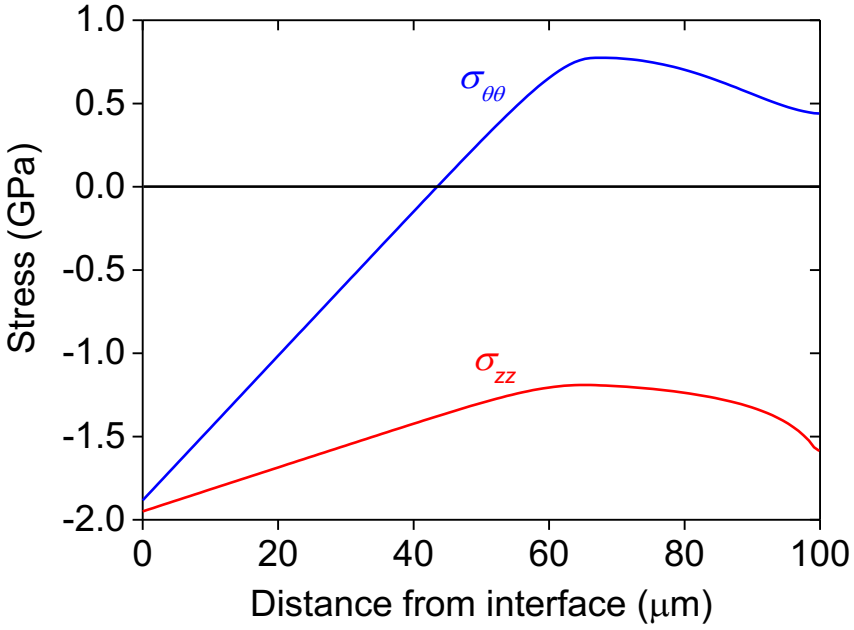

Figure 2-7: Stress distribution in an oxide layer of 100 μm thickness: circumferential stress ($\sigma_{\theta\theta}$) and axial stress (σ_{zz}).

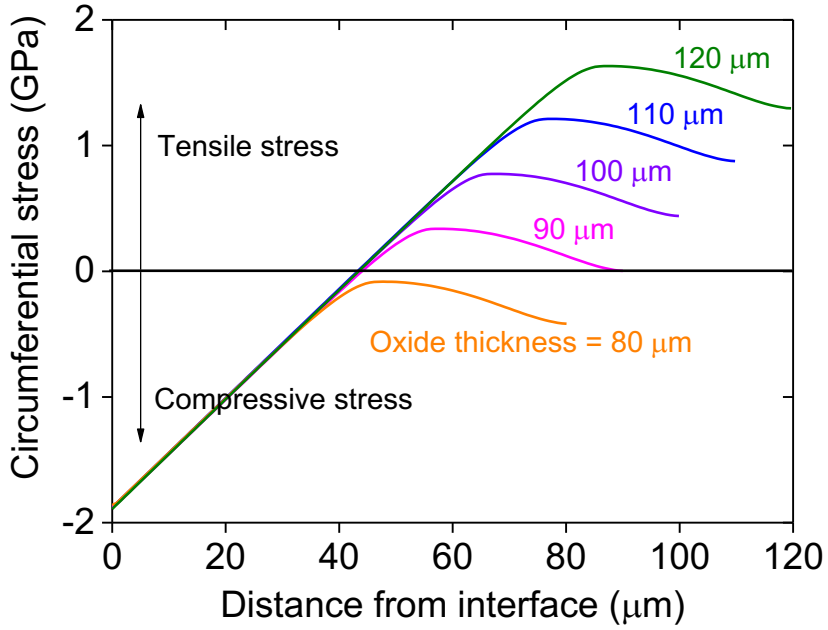

Figure 2-8: Distribution of the circumferential stresses in oxide layers with different thicknesses.

2.3.2 Fracture analysis of the oxide cracking

2.3.2.1 Crack channeling

As described earlier, the first step in calculating the fracture mechanics of crack channeling is to compute the depth of the channel cracks. This is done by computing the depths at different oxide thicknesses to which a radial crack might grow in the oxide under the influence of the circumferential stresses. The change in potential energy available for crack growth can be computed directly from the work done by tractions (of the opposite sign to the stresses) applied to the surface of a crack. Specifically, we calculated the *J*-integral resulting from the application of the tractions, and equated this to the energy-release rate. As will be apparent from the plots of energy-release rate against crack depth (Fig. 2-9), the energy-release rate initially increases with crack depth, reaches a maximum, and then drops if a crack becomes long enough to be influenced by the compressive stresses deep within the oxide. The minimum flaw that could propagate in a radial direction can be found from the smallest crack size for which the energy-release rate exceeds the toughness. Similarly, the depth to which a crack propagates can be found from the largest crack size for which the energy-release rate exceeds the toughness.

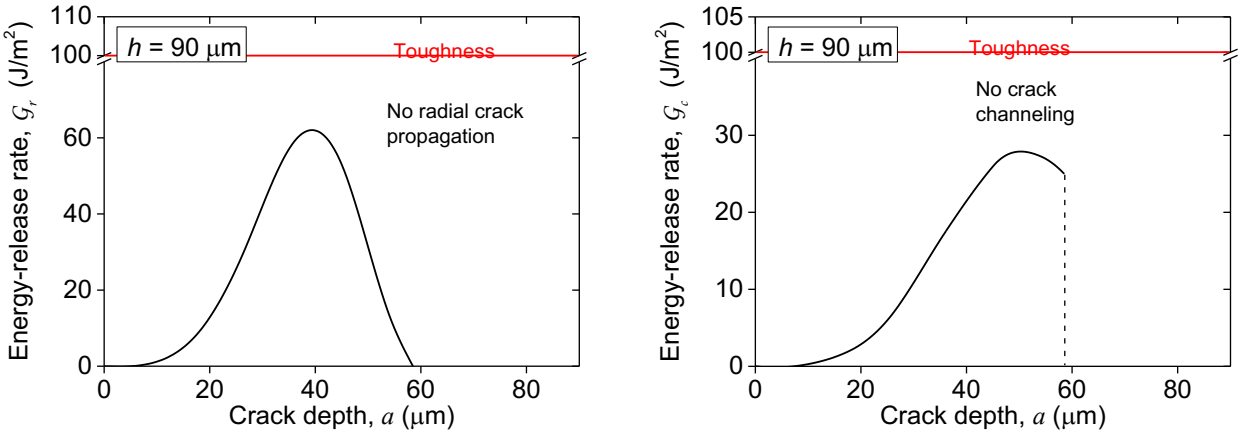

(a)

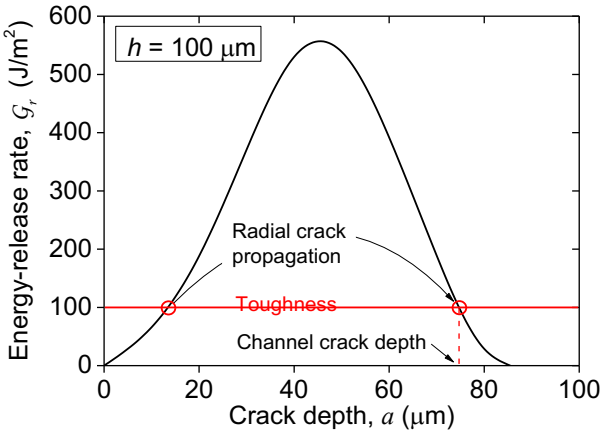
h = 100 μm
Energy-release rate, $\mathcal{G}_r$ (J/m^2)
Radial crack propagation
Toughness
Channel crack depth
Crack depth, a (μm)

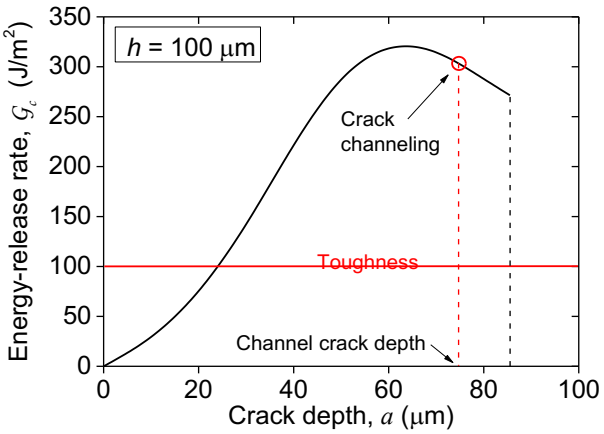
h = 100 μm
Energy-release rate, $\mathcal{G}_c$ (J/m^2)
Crack channeling
Toughness
Channel crack depth
Crack depth, a (μm)

(b)

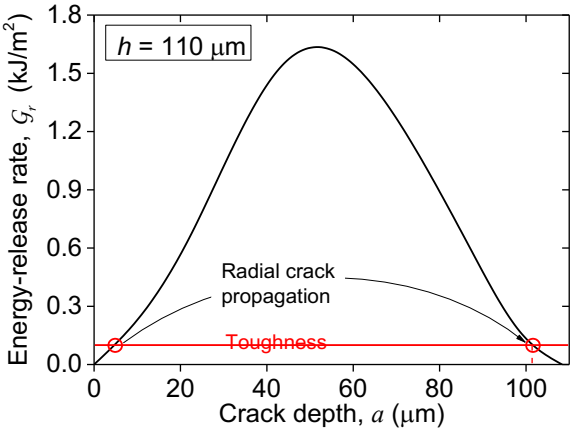
h = 110 μm
Energy-release rate, $\mathcal{G}_r$ (kJ/m^2)
Radial crack propagation
Toughness
Crack depth, a (μm)

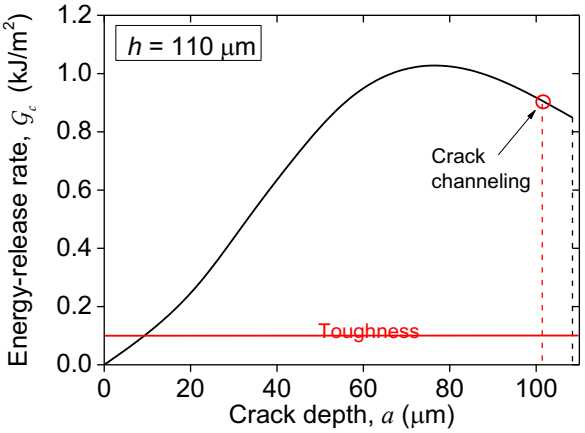
h = 110 μm
Energy-release rate, $\mathcal{G}_c$ (kJ/m^2)
Crack channeling
Toughness
Crack depth, a (μm)

(c)

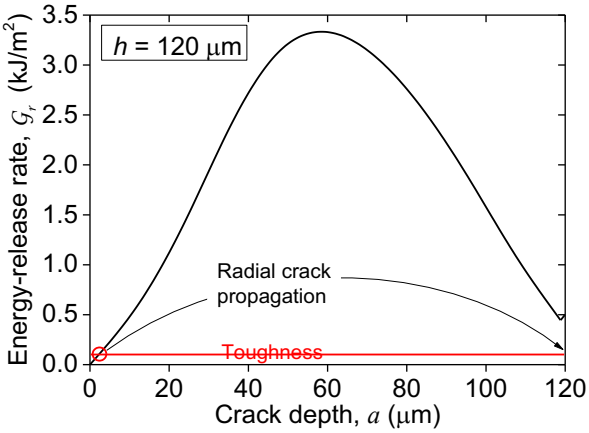
h = 120 μm
Energy-release rate, $\mathcal{G}_r$ (kJ/m^2)
Radial crack propagation
Toughness
Crack depth, a (μm)

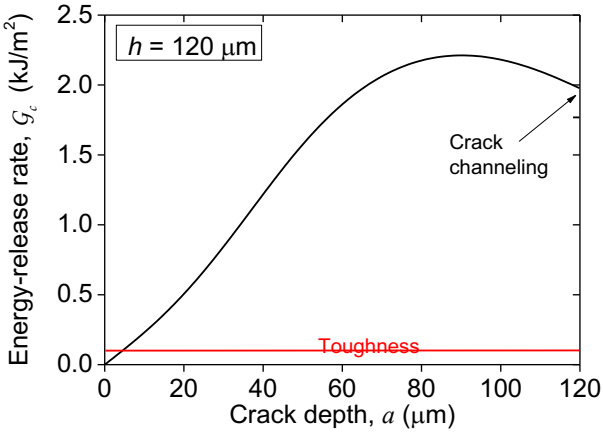
h = 120 μm
Energy-release rate, $\mathcal{G}_c$ (kJ/m^2)
Crack channeling
Toughness
Crack depth, a (μm)

(d)

Figure 2-9: Energy-release rates for a crack propagating from the surface towards the interface, to calculate the depth of a channel crack (left), steady-state energy-release rates for crack channeling (right) at different oxide thicknesses: (a) 90 μm, (b) 100 μm, (c) 110 μm, and (d) 120 μm. The horizontal line corresponds to toughness 100 J/m^2.

In these calculations, it was assumed that all the cracks extended from the surface. We did not consider the possibility of sub-surface channeling. As can be seen from Fig. 2-8, there is only a very narrow range of oxide thicknesses, between 80 and 90 μm, for which there is a sub-surface region of tension with compression on the surface, and for which sub-surface channeling might be expected. Plots of the energy-release rate, $\mathcal{G}_r$, are shown in Fig. 2-9 (left) as a function of crack depth below the surface for four different thicknesses of oxide, h, corresponding to 90 μm, 100 μm, 110 μm, and 120 μm. The energy release rates are calculated for putative cracks of any size that extend from the oxide surface (0) to the metal interface (h). As the thickness of the oxide increases, the values of the energy-release rate increase dramatically. In particular, for oxide thickness greater than about 110 μm, the energy-release rate is positive for cracks that extend all the way to the interface. Since the modulus of the Zircaloy is less than the modulus of the oxide, one would expect a singular energy-release rate if the crack tip reaches the interface [39], so that under these conditions the crack will be drawn slightly into the metal. This effect could just be resolved with the size of mesh used in these calculations for the case of an oxide thickness of 120 μm. It is possible to see a small kink at the end of the plot for the energy-release (Fig. 2-9d (left)) for a crack depth of just less than 120 μm.

Once the depth of a channel crack has been determined, the conditions under which it might propagate by extending along the axial direction of the cladding is computed. By assuming that the crack is much longer than its depth, a steady-state energy balance can be used to compute the energy-release rate for crack channeling $\mathcal{G}_c$. This is plotted in Fig. 2-9 (right) as functions of different crack depths. In a similar fashion to radial crack evolution, the energy-release rate

increases initially with crack depth, but decreases for deeper cracks, under the effect of the compressive stresses near the metal-oxide interface. As expected, the energy-release rate increases significantly as the oxide layer thickens. In Fig. 2-9a-c, the plot for the energy-release rate for crack channeling, $\mathcal{G}_c$, is truncated for the depth at which the crack tip becomes compressive.

The results of the calculations given above allow one to deduce crack depths, and conditions for channeling if the toughness of the oxide is known. Unfortunately, data for the toughness of a native-grown oxide of Zircaloy do not seem to exist in the literature. Most data for the toughness of zirconium oxide are for the partially-stabilized forms designed to have a high toughness. Therefore, owing to the lack of experimental data, we assume a toughness of 100 J/m^2, which is not unreasonable for a poly-crystalline ceramic [42], and use this value to illustrate the behavior. With this value of toughness, no flaws can propagate within an oxide thinner than 90 μm. Provided there are initial flaws greater than about 13 μm, cracks can grow and channel to a depth of about 74 μm for a 100 μm thick oxide. Similarly, with an initial flaw size larger than about 5 μm, cracks can grow and channel to a depth of about 101 μm for a 110 μm thick oxide. For an oxide thickness of 120 μm, initial flaws deeper than 3 μm can propagate to the metal-oxide interface. These may penetrate into the substrate as discussed above, and then channel through the oxide with their tips in the cladding. As mentioned previously, the energy-release rate increases significantly with increases in the thickness of oxide layer, so different values of toughness will provide similar conclusions, although the details of the crack depths will be different. Not considered in this analysis is what happens when the energy-release rate for channeling becomes sufficiently large for multiple channels to propagate [43]–[46], as observed in the cross-section metallography of CABRI REP-Na test rods [21].

2.3.2.2 Spalling analysis

A radial crack propagating down through a layer under residual tension can kink and propagate parallel to the interface, causing spalling [47]. The depth at which this spalling will occur can be determined by finding the depth at which the crack-tip phase angle of a circumferential crack originating from a radial crack is zero [47]. The phase angle can be expressed as $\psi = \tan^{-1}(K_{II}/K_I)$, where K_I and K_{II} are the mode-I and mode-II stress-intensity factors, respectively. A mode-II component of the stress-intensity factor will tend to drive the crack out of the plane in which it is propagating. Therefore, by finding the depth at which the phase angle is zero, the depth of the steady-state trajectory can be found [47].

The effects of the tractions required to relax the circumferential stresses, $\sigma_{\theta\theta}$, that act on the surface of the radial crack can be expressed in terms of an equivalent load, P, and an equivalent moment, M (Fig. 2-10a):

$$P = \int_{h-d}^{h} \sigma_{\theta\theta}\, dr \tag{2.1}$$

$$M = \int_{h-d}^{h} (\sigma_{\theta\theta} - P/d) r dr \tag{2.2}$$

where d is the depth of the circumferential crack, and h is the oxide thickness. If one makes the assumption that the curvature of the circumferential crack is large compared to d, and neglects the modulus mismatch across the oxide-metal interface, the results of Ref. [47] indicate that $\psi = 0$ when $d = 2.7M/P$. As shown in Fig. 2-10b, if the crack deviates closer to the top free surface, the sign of the mode-II stress-intensity factor will drive it down. If the crack deviates closer to the oxide-metal interface, the sign of the mode-II stress-intensity factor will drive it up [47]. Therefore, this is the depth at which such a crack would propagate in a stable trajectory.

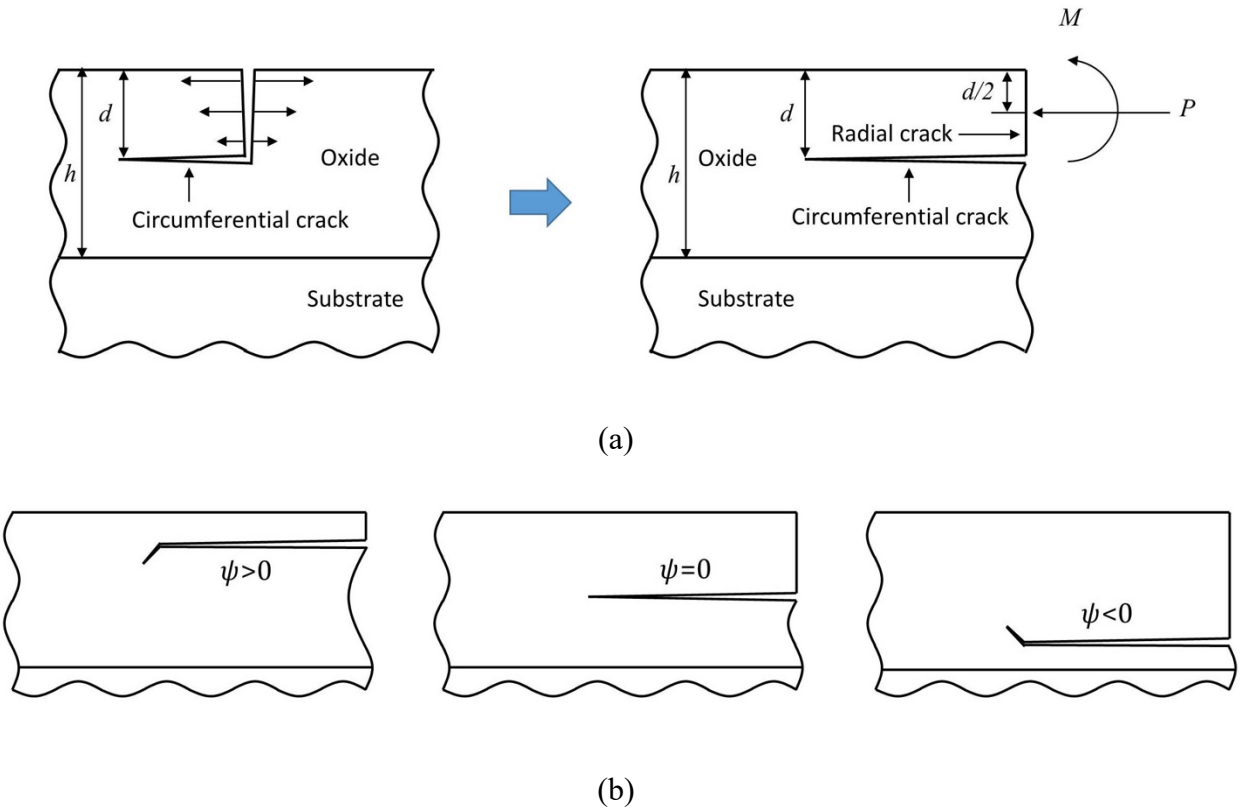

(a)

(b)

Figure 2-10: (a) A circumferential crack parallel to the interface at depth d, intersecting with a radial crack where a representative effective load and moment is applied on the surface. (b) The effects of crack tip phase angle, ψ, on the crack trajectory.

The results of these calculations are shown in Fig. 2-11 for different values of h. The intersection of the two lines shows the spall depth. For the case of an oxide thicknesses of 90 μm, the radial crack cannot propagate to the depth corresponding to the mode-II $= 0$ plane, no matter how brittle the oxide is assumed to be. So spalling would not occur for this thickness of oxide. On the other hand, the radial crack can grow below the possible spall depth if the oxide is thicker than about 100 μm. In this case, spalling can possibly occur. For example, Fig. 2-11 indicates that spalling may occur 19 μm above the metal-oxide interface for the 110 μm thick oxide and 15 μm above the interface for the 120 μm thick oxide. To determine if spalling is thermodynamically viable at the possible spall depths, we further calculated the corresponding energy-release rates [45]. Experimental observations indicate that periodic bands of high-porosity can develop in the

oxide layer parallel to the metal-oxide interface [48]. This could result in a lower fracture toughness parallel to the interface than perpendicular to the interface. This is conducive to spalling and it was found that the spalling can indeed occur based on the above calculations. It is noted that the calculated depth of the spalls is above the metal-oxide interface, leaving a thin layer of oxide adhered to the metal as sometimes observed experimentally [21].

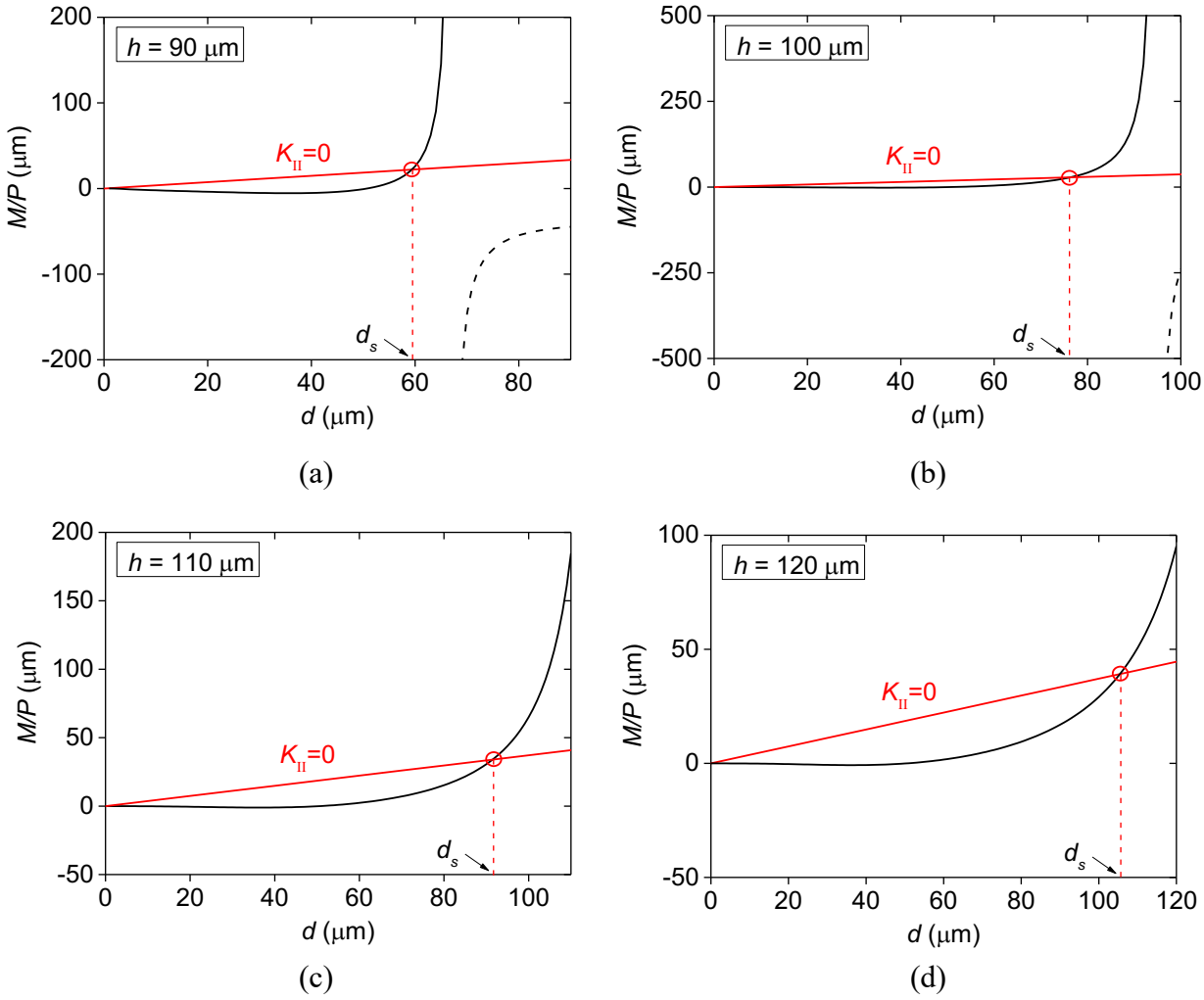

Figure 2-11: Ratio of equivalent moment to force as a function of crack depth, d, at different oxide thicknesses: (a) 90 μm, (b) 100 μm, (c) 110 μm, and (d) 120 μm. The dotted portion of the line corresponds to depths at which $K_I < 0$, owing to the compressive stresses in the oxide. The straight line corresponds to the ratio required to make $K_{II} = 0$. The intersection between the two solid lines indicates a stable spall depth [36].

2.3.3 Effect of alloy composition of the cladding

Change in alloy composition of the cladding can affect various mechanisms involved in the operation of reactors. For example, the oxidation rate and creep rate depend on the tin level of the Zircaloy cladding [39, 40]. We therefore discuss the effect of alloy composition of the cladding on the development of the stresses in the oxide layer associated with the cracking and spalling in this section.

The cracking and spalling of the oxide layer are caused by a tensile circumferential stress in the oxide layer which is generated mostly after contact between the pellet and cladding. Therefore, the cracking process depends on the thickness of the oxide layer at which contact occurs. If the contact occurs at the early stage of oxidation, a tensile stress would evolve at relatively a thin oxide layer. Assuming the swelling rate of the pellet is constant, it can be obtained by decreasing the oxidation rate or increasing the creep rate of the cladding.

If the swelling rate of the pellet and the creep rate of the cladding are set to be the same, the actual time when the contact occurs will also remain the same. Decrease in the oxidation rate then leads to a thin oxide layer at the point of contact, indicating that tensile circumferential stress can evolve at relatively a thin layer of oxide layer, which is ensured by a separate calculation. Recent experimental observation of oxide surface peeling (OSP) demonstrates this, where a thin layer of oxide is removed from the optimized ZIRLO cladding which has low oxidation rate with low level of tin content [51]. For low oxidation rate, we note that the swelling of the pellet dominates over the oxidation in developing the tensile stress in the outer oxide layer.

If the creep rate of the cladding increases (e.g. due to decrease in the grain size associated with the increase in the diffusional creep rate) while the rates of fuel swelling and the oxidation of the cladding are constant, the contact occurs earlier due to the fast creep-down of the cladding.

Since the stress relaxation of the oxide layer due to the creep of the cladding is negligible, this also leads to the development of tensile circumferential stress in relatively a thin oxide layer, which is confirmed through a separate calculation.

2.4 Conclusion

A finite-element model to study the evolution of radial cracks in the oxide that lead to spalling under normal operating conditions was constructed by incorporating the multiple mechanisms of creep, swelling and oxidation. First, an analysis of the development of stresses in the oxide was conducted. Before contact occurs between the fuel pellet and cladding, the circumferential stress in the outer oxide layer is initially very compressive owing to growth stresses. This compression increases as the cladding creeps down to the pellet. However, volume expansion associated with newly formed oxide at the interface induces a tensile contribution to the stresses in the outer regions of the oxide formed earlier. Swelling of the fuel pellet after contact with the cladding further induces a strong tension in the oxide layer by pushing the cladding outward. With the combined effects of these two phenomena, the circumferential stress in the outer region of the oxide becomes tensile after a critical thickness.

A cracking analysis in the oxide layer was performed by using the calculated values of the circumferential stress. The crack depth for crack channeling was determined by calculating the energy-release rate for extending radial cracks into the oxide. This analysis showed that energy-release rate increases dramatically as the oxide thickness increases. Subsequently, the steady-state energy-release rate for crack channeling was computed. The results indicated that this value also increases dramatically with oxide thickness. The results could be classified into three cases depending on the thickness and toughness of the oxide layer: (i) radial cracking without channeling, (ii) channel cracking within the oxide, and (iii) channel crack through the entire oxide

and possibly penetrating into the metal. Corresponding spall depths were also calculated; these indicated that spalling will leave a thin oxide layer adhered to the metal, as occasionally observed experimentally.

As distinct from previous studies that have concentrated on oxide spalling under transient conditions comparable to RIA, the present study emphasizes spalling under normal operating conditions for PWRs. This gives an explanation for cracking of the oxide layer during service. A fuller extension could be developed by introducing the concept of periodic cracking.

Chapter 2 is reproduced from the publication:

K. Hong, J. R. Barber, M. D. Thouless and W. Lu, “Cracking and spalling of the oxide layer deve loped in high-burnup Zircaloy-4 cladding under normal operating conditions in a PWR”, *Journal of Nuclear Materials*, *512*, 46-55, 2018

Chapter 3 Cracking of Cr-Coated Accident-Tolerant Fuel During Normal Operation and Under Power-Ramping Conditions

3.1 Introduction

The fuel rods in a pressurized-water reactor (PWR) operate within the oxidizing environment of the primary coolant. Oxidation of the cladding results in the complementary process of hydrogen formation, which precipitates within the cladding in the form of brittle hydrides. The mechanical degradation induced by the hydride precipitation makes the cladding more vulnerable to failure from pellet-cladding interaction (PCI) [5]. This process of hydride formation becomes even more severe when the integrity of the oxide layer is damaged by cracking and spalling, which can occur under normal operation [6], or as a result of a reactivity-initiated accident (RIA) power transient [7].

These problems have prompted the development of accident-tolerant fuel (ATF) claddings that are more resistant to oxidation. Several ATF technologies have been suggested; these include coated-Zircaloy, FeCrAl, and SiC/SiC (SiC fiber-reinforced SiC matrix composite) claddings [8]. The coated-Zircaloy cladding has an advantage over the other techniques because it does not require manufacturing a cladding with completely different materials. With its easy and economical fabrication, coated-Zircaloy claddings are considered to be a near-term option for deployment [8]–[10].

Several metals and alloys have been considered as potential candidates for coating materials that can form a protective layer against oxidation [8]. Among them, Cr exhibits excellent

performance in terms of radiation stability [11], [12] and corrosion resistance, at both the low temperatures corresponding to normal operation, and at the high temperatures corresponding to a design-basis accident (DBA) [13], [14].

The adhesion strength between Zircaloy and Cr has been investigated by *ex-situ* experiments using ring-compression and ring-tensile tests [10]. It was found that interfacial adhesion was retained, without any spalling or buckling-driven delamination, even at high compressive or tensile strains (up to 6 %). In addition, numerical analyses have been conducted to study the in-core performance of a coated cladding [52], [53]. Lee et al. (2017) calculated the development of compressive stresses in the coating in the absence of PCI. They analyzed the effects of pressure, thermal expansion, irradiation-induced axial growth, and creep. More recently, Wagih et al. (2018) investigated the tensile stress generated within the Cr coating as a result of PCI during normal operation, and as a result of transient conditions.

These previous studies have focused on the stress evolution in the coating. However, analysis of possible fracture is also essential because Cr is a relatively brittle material [54]. Fracture, in the form of channeling cracks, has been observed experimentally in a Cr coating on Zircaloy using a ring-tensile test [10]. This is of concern because, once a crack propagates to the Cr/Zircaloy interface, extremely localized oxidation, in the form of pitting corrosion, can occur in the Zircaloy near the crack tip, as has been shown in autoclave corrosion tests [55]. This further results in serious mechanical degradation of the cladding by hydride embrittlement.

In light of these observations, we have performed a fracture analysis of the Cr coating under normal operation, and under power-ramping conditions. A finite-element model that incorporates multiple deformation mechanisms, such as creep, thermal expansion, irradiation growth, and fuel swelling and sintering, has been developed. Since experiments have shown good interfacial

adhesion between Cr and Zircaloy [10], we did not consider delamination, but focused on the channeling cracks that can be induced by tensile hoop stresses, using a fracture-mechanics approach. We anticipate that our model could be used to expand existing fuel performance codes, including those being developed by the Consortium for Advanced Simulation of Light Water Reactors (CASL) [56].

3.2 Finite-Element Model

A finite-element model was developed to calculate the stress state within the Cr coating. Then, the conditions for the propagation of channel cracks within the coating were calculated using linear-elastic fracture mechanics (LEFM).

3.2.1 Geometry and boundary conditions

A finite-element model of the fuel assembly, consisting of the fuel pellet and cladding, was developed using the commercial software, ABAQUS. Because of the strong adhesion between the materials, it was assumed that the coating layer was perfectly bonded to the Zircaloy. A simplified, 1D, axisymmetric model was considered, as shown in Fig. 3-1. The dimensions used in the model were based on typical PWR fuel rods. The thickness of the Cr coating can vary from a few micrometers to tens of micrometers [57], [58]. Therefore, a parametric study of the effect of coating thickness was performed.

The initial gap between the outer surface of the pellet and the inner surface of the cladding was assumed to be 80 μm, and filled with helium. The contact between the pellet and cladding was modeled by a normal, hard contact to prevent penetration. The internal pressure induced by the helium gas was assumed to be constant at 4 MPa, while the external pressure associated with the primary coolant was set to be 16 MPa [22].

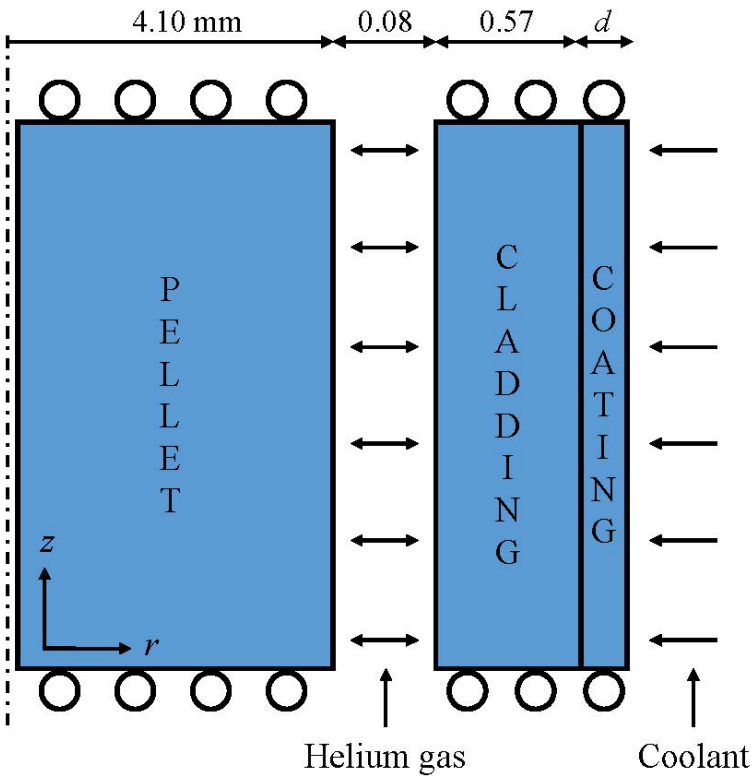

Figure 3-1: A 1D, axisymmetric model of fuel assembly. Dimensions are representative of a typical fuel rod in a PWR. Various thicknesses of the Cr-coating layer *d* were considered in the parametric study. The displacement along the *z*-direction was restricted. Along the *r*-direction, pressure boundary conditions were imposed to account for the difference between the internal pressure induced by the helium gas and the external pressure of the primary coolant.

The system was assumed to be initially at 300 K. Upon start-up, a uniform power generation of 20 kW/m (typical for a PWR under normal operation [23]) was applied to the fuel pellet as a body heat-flux. The temperature of the external surface of the cladding was set to be constant at 600 K, corresponding to the coolant temperature. Power-ramping transients were considered by parametric studies of increasing the power to various levels above 20 kW/m. The transition from normal operation to a power-ramping condition was assumed to occur in the form of a step change in the power generation.

The thermo-mechanical properties, such as elastic modulus, specific heat, density, thermal conductivity, and thermal-expansion coefficient, for the UO_2 pellet and Zircaloy cladding were obtained from the MATPRO model [37], and from Holzwarth and Stamm (2002) for the Cr coating. The temperature-dependent thermal conductivity of helium in the gap between the fuel pellets and cladding was also obtained from the MATPRO model [37]. Perfect thermal contact (temperature continuity) was assumed once the pellet and cladding came into contact.

3.2.2 Deformation mechanisms

We implemented the creep of Zircaloy into the finite-element calculations by using a mechanism-based model built upon decades of experimental data [32]. The creep of UO_2 was implemented using the deformation-mechanism map of Frost and Ashby (1982). These models incorporate multiple creep mechanisms, including dislocation creep, diffusional creep, and power-law creep, with creep strains being controlled by the von Mises effective stress. The grain sizes of Zircaloy and UO_2, which are needed for the creep calculations, were assumed to be 50 μm and 10 μm, respectively.

The creep of Cr was also implemented using the deformation mechanisms of Frost and Ashby (1982). However, the value quoted in this reference for the dislocation-glide parameter, τ_g, which is the shear strength at 0 K, corresponds to a grain size of 0.1 mm, while the grain size in the middle of the coating is expected to be much smaller at about 300 nm [10]. Since the grain size affects τ_g, its value, 1.11 GPa, was obtained from the Hall-Petch relationship [20], [60] with parameters taken from Brittain et al. (1985).

We also included irradiation-induced deformations of Zircaloy and UO_2 in the calculation, incorporating models from MATPRO [37] for irradiation creep and growth of Zircaloy, and irradiation creep of UO_2 (see Appendix 3.A.1-3.A.3).

The swelling of the UO_2 pellet, which is induced by the accumulation of fission products within the pellet, was modeled based on the MATPRO model [37]. During early irradiation, the expansion of the fuel caused by swelling can be partially compensated by the fuel densification induced by irradiation sintering. We therefore also incorporated densification by implementing the model from MATPRO [37] (see Appendix 3.A.4). The amount of densification strongly depends on the total densification that can occur, denoted as $\Delta\rho_0$ in Eq. (3.A.4), which is associated with initial pores in the fuel being eliminated by densification (DOE, 1993). We first set the value to be zero by assuming a high initial fuel density, and then increase the value to explore how it affects the result.

Oxidation of the Cr coating layer was neglected in the calculations, because it is almost negligible under the operating conditions of a PWR [9], [10], [63].

3.3. Development of stresses in the Cr-coating layer

3.3.1 Normal operation

For the case of normal operation, 3 operating cycles (1 cycle = 18 months) with a linear heat rate (LHR) of 20 kW/m were considered. Figure 3-2a shows the development of the hoop stress at the surface of a Cr coating that is 10 μm thick. As can be seen from Fig. 3-2b, the stress in the coating is essentially uniform, since the coating is much thinner than the cladding. Immediately upon start-up, the stress becomes highly compressive (around 1 GPa) owing to the external pressure from the primary coolant and the mismatch in the thermal strain. Creep results in a rapid relaxation of the stress, until a first plateau is reached when the shrinkage rate of the cladding in response to the pressure in the coolant matches the creep rate of Cr. Once the gap is closed, the cladding expands because of the fuel swelling, and the stress in the Cr coating becomes

tensile until it reaches a second plateau at which the expansion rate of the cladding matches the creep rate of Cr.

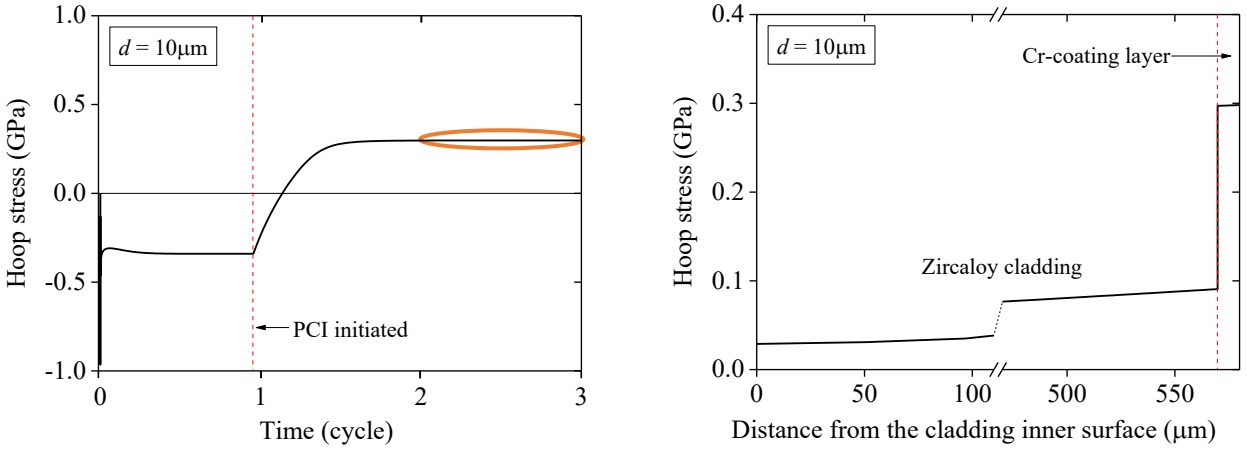

Figure 3-2: (a) Development of hoop stress at the surface of a Cr coating with a thickness of d =10 μm during 3 cycles of normal operation. There are two regimes in which the stress reaches a plateau. The first, before PCI is initiated is compressive, when the rate of the creep down of the Zircaloy matches the creep rate of the Cr. The second, after PCI is initiated is tensile, when the swelling rate of the fuel matches the creep of the Cr. The onset of PCI is indicated by the dashed line just before the end of the first cycle. (b) The steady-state stress distribution as a function of radial position within the cladding and coating after the second plateau has been reached. The stress in the coating is essentially uniform, since the coating is much thinner than the cladding.

During operation, fission gases are released from the fuel, which can increase the internal pressure within the fuel rod to a value near the coolant pressure [64]. We therefore considered the effect of increasing internal pressure up to 16 MPa, equivalent to the external pressure. Separate calculations showed that this leads to a delayed initiation of PCI owing to reduced rate at which the cladding creeps down. Similarly, if the fuel densification, $\Delta\rho_0$, increases, it delays the onset of PCI. However, neither of these has a significant effect on the maximum hoop stress in the coating.

Thermal gradients within the fuel, generated during the initial start-up or after the onset of a power ramp, can lead to radial cracking and crack-induced relocation [15]. However, these would

only produce local effects restricted to the inner surface of the cladding. For example, a companion study [65] has shown that cracked fuel leads to localized stress fields in the vicinity of fuel cracks, but their effect vanishes away from the point of contact. As a result, fuel cracks have negligible effect on the stress in the Cr coating. We also considered increase in the average contact pressure owing to fuel relocation, modeled as an overall increase of fuel diameter given in BISON [56], but its effect was found to be negligible.

By comparing the effects of different creep mechanisms in the finite-element calculations, we found that power-law creep dominates the stress relaxation, while the contribution of diffusional creep is relatively small. In particular, the effect of diffusional creep on the stress in the coating almost vanishes when the grain size is larger than 500 nm, a typical grain size experimentally observed near the surface of the coating layer [55]. Results for a range of coating thicknesses between 1 μm and 100 μm showed that the stress in the coating after three cycles was almost independent of its thickness.

We also ran a separate calculation without including irradiation-induced deformations of the Zircaloy and UO_2, and found that they do not affect the result. This suggests that the dimensional changes induced by irradiation are relatively small compared to those caused by other mechanisms, such as thermal creep.

3.3.2 Power ramping condition

To study the development of stress in the coating under power-ramping conditions, a power history with 2 cycles of normal operation (LHR = 20 kW/m, denoted as LHR_{normal}) followed by 12 hours of power ramp was implemented in the numerical model.

The evolution of the hoop stress at the surface of the coating is shown in Fig. 3-3a for a thickness of 10 μm, and a ramped power of (40 kW/m), designated as 2 LHR_{normal}. It can be

observed that the stress increases sharply after the onset of a power ramp, as a result of the thermal expansion of the pellet. The stress reaches a maximum level almost immediately (within 1 minute after the onset of a power ramp), before decreasing as a result of creep in the Cr coating (dominated by power-law creep in this particular case).

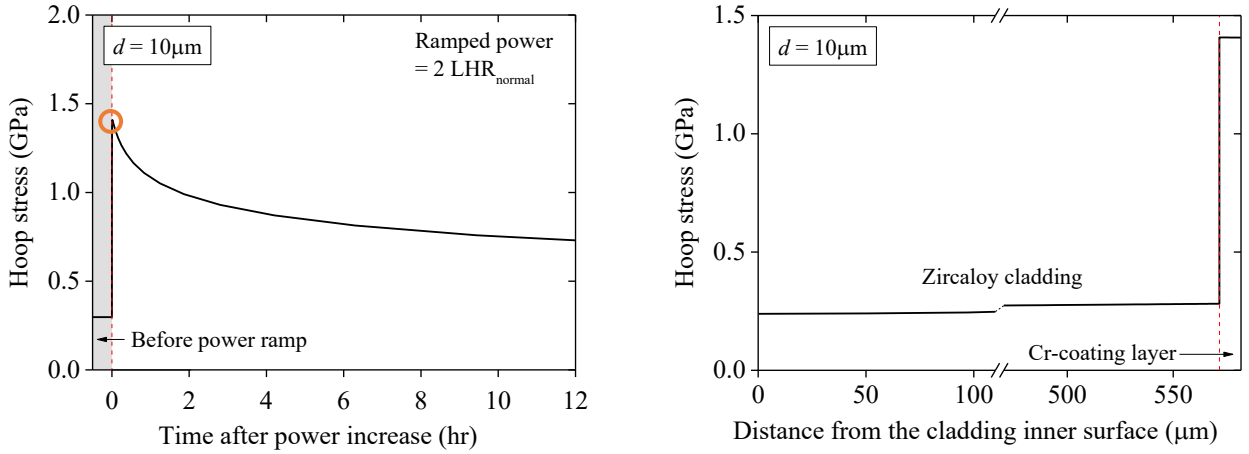

Figure 3-3: (a) Development of hoop stress in the surface of a coating layer under power ramping. The power history consists of 2 cycles of normal operation (LHR = 20 kW/m) and 12 hours of power ramp with a LHR = 40 kW/m. The shaded region shows the stress level shortly before the power ramp. (b) The stress distribution in the cladding and coating layer almost immediately after the power increase when the stress in the coating layer reaches a maximum, *i.e.*, the circled region in (a). The stress distribution in the coating layer is uniform along the radial direction.

Our interest lies in the possible fracture of the Cr coating, therefore, we focus on the maximum stress that is reached immediately after power ramping. The stress distribution in the cladding and coating at this time is shown in Fig. 3-3b. The stress in the coating is 1.4 GPa, much higher than that during normal operation. It was found that the maximum tensile stress in the coating after a power ramp is essentially independent of the coating thickness.

An increase in the power during a power ramp causes an immediate thermal expansion of the fuel pellet, leading to an elevated tensile hoop stress in the Cr coating. The ramped power is

known to be a key factor contributing to possible PCI failures [5], [16]. Therefore, the effect of different levels of ramped power on the development of the hoop stress in the Cr coating was investigated. The result is plotted in Fig. 3-4a, which shows the evolution of the hoop stress after different power ramps. As expected, a higher ramped power results in a larger hoop stress within the coating. After quickly reaching a maximum, the stress decreases with time as Cr creeps. It was found that the stress relaxation is dominated by power-law creep at low ramped powers, but is dominated by dislocation glide at high ramped powers. Figure 3-4b shows the maximum hoop stresses in the coating at different levels of ramped power. The maximum hoop stress increases with ramped power, but becomes essentially independent of power when dislocation glide becomes the dominant mechanism for stress relaxation.

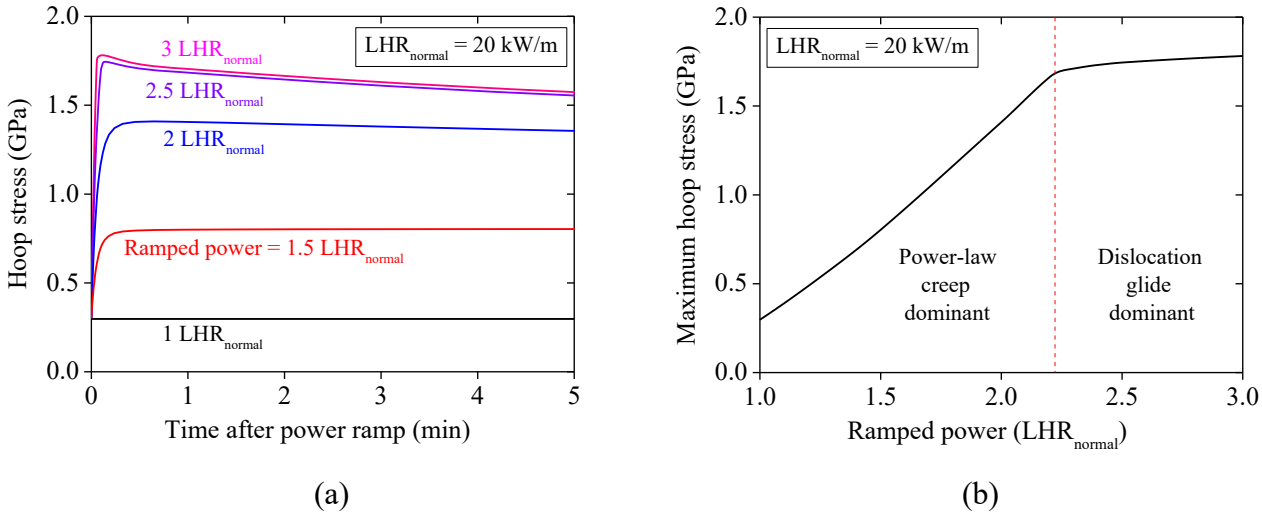

Figure 3-4: (a) Development of hoop stresses in the coating after different levels of ramped power. (b) The maximum hoop stresses in the coating layer after different levels of ramped power (in the multiple of LHR_{normal}). Stress relaxation is dominated by power-law creep at low ramped powers, but dominated by dislocation glide at high ramped powers. The maximum hoop stress increases with ramped power but becomes essentially independent of power when dislocation glide dominates stress relaxation.

3.4 Fracture analysis of crack channeling in the Cr-coating layer

Since the Cr coatings exhibit a columnar grain morphology near the surface, it is likely that suitable initial flaws for crack channeling are an inherent feature of the system, as observed in Brachet et al. (2015). Therefore, we assumed that such flaws pre-existed in the coating, and focused our attention on whether they could propagate as channel cracks under the appropriate level of hoop stress. The crack-channeling analysis was performed conservatively by assuming the crack depth to be equal to the thickness of the coating. The energy-release rate was calculated from the work done by the tractions (equal to the coating stress, but with opposite sign) applied to the assumed cracked surface. The conditions for a crack to channel were then obtained by comparing the energy-release rate to the coating toughness.

The steady-state energy-release rate for crack channeling in a layer of thickness d is given by [39]

$$G_{ss} = \frac{1}{2}\frac{\sigma^2 d}{\bar{E}}\pi g(\alpha,\beta), \tag{3.1}$$

where σ is the tensile stress in the coating layer, given here by the maximum stress after the power ramp, $\bar{E}$ is the plane-strain modulus of the layer, and $g(\alpha,\beta)$ is a function of the Dundurs' bimaterial parameters α and β [66]. For the material combination of Cr with Zircaloy, we have α = 0.56 and β = 0.14, and $g(\alpha,\beta)$ = 2.26. The energy-release rate was calculated using Eq. (3.1), which is plotted in Fig. 3-5 as a function of the coating thickness for different levels of ramped power.

With a body-centered-cubic structure, Cr exhibits a ductile-to-brittle transition temperature (DBTT) [59]. This transition temperature decreases as the grain size increases, with a value of 660 K at a grain size of 34 μm and a value of 255 K at a grain size of 225 μm, respectively [3]. Since even the smallest of these grains is bigger than those observed in the thin Cr coatings considered

here, it is reasonable to assume that the operating temperatures of a PWR are much lower than the DBTT for Cr, so that a reasonable range for toughnesses is between 0.1 and 0.3 kJ/m^2 [54], [59]. This range of Γ is indicated by the hatched region in Fig. 3-5, with crack channeling occurring if $G_{ss} > \Gamma$.

As mentioned in Section 3.3, the maximum tensile hoop stress for any given power history is almost independent of the coating thickness, at least up to 100 μm. Therefore, Eq. (3.1) indicates that the energy-release rate increases approximately linearly with the coating thickness. Figure 3-5 compares finite-element results (solid lines) with a linear approximation based on the maximum stresses for a 1 μm layer, for various power histories. The approximation differs significantly from the more accurate results only in the ranges where the energy-release rate is well above the Cr fracture toughness. We shall exploit this result to develop a simpler fracture analysis protocol in Section 3.5.

By calculating the intersection between the lines of energy-release rate and toughness, one can obtain the critical coating thickness above which a channel crack forms. Figure 3-6 shows the critical thickness as a function of ramped power. The hatched region is associated with the range of fracture toughness, Γ, for Cr, with the lower bound corresponding to Γ = 0.1 kJ/m^2, and the upper bound to Γ = 0.3 kJ/m^2. The critical coating thickness decreases with increasing ramped power and reaches a plateau between 3 μm and 8 μm when dislocation glide becomes the dominant creep mechanism for stress relaxation. The Cr-coated Zircaloy cladding should be designed with the coating thickness in the safe zone, *i.e.*, less than the critical thickness of the coating.

These results may change quantitatively in that the actual properties of a Cr coating may differ from those assumed here, since they are taken from bulk values, and they may also vary depending on the fabrication technique, chemical composition, and grain size. However, it should

be noted that the broad conclusions from the analysis are not affected by the detailed properties of the Cr coating. At the early stage of design, where *in-situ* experimental data are limited [8], this analysis will be essential for constructing experiments to investigate the performance and for the actual design of the ATF cladding.

3.5 A simplified design protocol

The Cr coating is much thinner than the Zircaloy cladding. Therefore, the stress in the coating is dominated by its interaction with the cladding. This suggests a design protocol as follows:

1. Analyze the stress in the Zircaloy cladding, assuming no coating.
2. Impose the corresponding hoop strain with time on the Cr-coating layer.
3. Use the resulting hoop stresses in the coating layer to estimate the likelihood of channeling.

Step 1 can be achieved using existing PCI codes in the industry. The hoop stress in the coating can be computed in Step 2 by incorporating the creep mechanisms of Cr. In this way, one can easily perform cracking analysis of the Cr coating. We have confirmed through a simple Matlab routine (see Appendix 3.B) that this protocol generated the same results of a full finite-element modelling of the cladding and coating together.

3.6 Conclusion

In this chapter, the growth of channeling cracks in the Cr coated on Zircaloy cladding has been analyzed under normal operation, and under power-ramping conditions. It was found that high tensile hoop stresses develop in the coating when the cladding is pushed outwards through

PCI. The maximum hoop stress increases with the ramped power, until the stress is limited by dislocation glide in the Cr coating.

The steady-state energy-release rate for crack channeling increases almost linearly with the thickness of the coating layer, allowing a critical coating thicknesses, above which cracking would occur, to be determined as a function of ramped power. This critical coating thickness decreases with the level of ramped power. The design of Cr-coated Zircaloy cladding should ensure that the thickness of the coating layer is below the critical value. A design protocol has been suggested that allows fracture analysis of the Cr coating to be developed using existing PCI codes. This provides a design option without the need for developing new finite-element codes to analyze the cladding and coating layer together.

Appendix 3.A Effect of irradiation on Zircaloy and UO_2

3.A.1 Irradiation creep for Zircaloy

The equation for the irradiation creep of Zircaloy was taken from MATPRO [37]:

$$\dot{\epsilon}_{irradiation} = C_0 \phi^{C_1} \sigma_m^{C_2}, \tag{3.A.1}$$

where $\dot{\epsilon}_{irradiation}$ is the irradiation creep strain rate, ϕ is the fast neutron flux set to be 3×10^{17} n/m^{2}s, σ_m is the von Mises effective stress, C_0, C_1, and C_2 are material constants which are 1.654×10^{-24}, 0.85, and 1, respectively [56].

3.A.2 Irradiation creep for UO_2

Combined thermal and irradiation creep of UO2 is expressed by the following equation in MATPRO [37]:

$$\dot{\epsilon} = \frac{A_1 + A_2 \dot{F}}{(A_3 + D)G^2} \sigma_m e^{-\frac{Q_1}{RT}} + \frac{A_4}{(A_6 + D)} \sigma_m^{4.5} e^{-\frac{Q_2}{RT}} + A_7 \dot{F} \sigma_m e^{-\frac{Q_3}{RT}}, \tag{3.A.2}$$

where $\dot{\epsilon}$ is the creep strain rate, σ_m is the von Mises effective stress, $\dot{F}$ is the volumetric fission rate, D is the fuel density, G is the grain size, Q_1 to Q_3 are activation energies, R is the universal gas constant, T is temperature, and A_1 to A_7 are material constants.

There is a discrepancy between the part of thermal creep in MATPRO and the deformation mechanism map by Frost and Ashby (1982). We used the latter for thermal creep since it is more comprehensive. For example, it includes grain-boundary and lattice-controlled diffusion, power-law creep induced by core diffusion and lattice diffusion, and dislocation glide, which are not explicitly included in the MATPRO equation. Therefore, we implemented irradiation creep from MATPRO (A_2 and A_7 terms associated with irradiation), and thermal creep from the deformation mechanism map. The values of irradiation parameters were set to be $D = 95$ %, $A_2 = 1.3100 \times 10^{-19}$, $A_3 = -87.7$, $A_7 = 3.72264 \times 10^{-35}$, $Q_1 = 3.76591 \times 10^5$ J/mol, $Q_3 = 2.6167 \times 10^3$ J/mol, $\dot{F} = 1.2 \times 10^{19}$ fission/m^{3}s.

3.A.3 Irradiation growth for Zircaloy

The equation for irradiation growth of Zircaloy was taken from MATPRO [37]:

$$\epsilon_i = 1.407 \times 10^{-16} \mathrm{e}^{\frac{240.8}{T}} (\phi t)^{0.5} (1 - 3f_i)(1 + 2CW), \qquad (3.\mathrm{A}.3)$$

where ϵ_i is the normal strain in the i direction, T is temperature in K, ϕ is the fast neutron flux and assumed to be 3×10^{17} n/m^{2}s, t is time in s, f_i is the fraction of grains with the c-axis oriented along the i direction, and CW is the reduction in the cross-section area caused by cold work and is set to be 25 %.

For the calculations in Section 3.3, isotropy was assumed based on random grain orientation of polycrystalline materials. As can be seen in Eq. (3.A.3), irradiation growth does not cause any dimensional change in an isotropic microstructure (f_i =1/3). To see the effects of

irradiation growth on the result, we implemented an anisotropic microstructure, where $f_r = 0.66$, $f_\theta = 0.28$, and $f_z = 0.06$ [37].

3.A.4 Fuel densification

Fuel densification induced by irradiation sintering is expressed by the following equation [67]:

$$\epsilon_D = \Delta\rho_0\left(e^{\frac{Bu\ln(0.01)}{C_D Bu_D}} - 1\right), \quad (3.A.4)$$

where ϵ_D is the densification strain, $\Delta\rho_0$ is the total densification that can occur (a fraction of the theoretical density), Bu is the burnup, and Bu_D is the burnup at full densification, which was set to be 5 MWd/kgU [64]. C_D is a temperature-dependent parameter given by $7.2 - 0.0086(T - 298.15)$ for $T < 1023.15$ and 1.0 for $T > 1023.15$, where T is temperature in K.

Appendix 3.B Matlab routine demonstrating the design protocol

```
% ------------------------------------------------------------------------
% Function Name: myplot
% Purpose: solve ODE to obtain hoop and axial stresses
% Inputs: time domain, initial axial stress, initial hoop stress
% Outputs: plot of stresses vs time
% ------------------------------------------------------------------------
function myplot(t_f,s0_a,s0_h)
s0 = [s0_a s0_h];
% Initial conditions of axial stress(s0_a) and hoop stress(s0_h)
corresponding to thermal mismatch stress
tspan = [0 t_f]; % Timespan from 0 to t_f
[t,y] = ode45(@(t,y) odefun(t,y), tspan, s0);
% ODE solver with Runge-Kutta (4,5) formula
plot(t,y(:,1),'-o',t,y(:,2),'-.') % Plot the stresses vs time
```

```
end
% ------------------------------------------------------------------------
% Function Name: odefun
% Purpose: set up ODE based on constitutive law and creep law at time t
% Inputs: time, stresses
% Outputs: derivatives of stresses
% ------------------------------------------------------------------------
function dydt = odefun(t,y)
% y(1) : axial stress, y(2) : hoop stress
v = 0.22; % Poisson ratio of Cr
E = 280000; % Elastic modulus of Cr
% Read strain-time data from FE calculation
fileID = fopen('strain_clad.txt','r');
% Text file 'strain_clad.txt' is indicated by the file identifier
formatSpec = '%d %f'; % Format of data fields
sizeA = [2 Inf]; % Dimensions of output array
A = fscanf(fileID,formatSpec,sizeA);
t_1 = A(1,:); % Time data
s_tot = A(2,:); % Strain data
s_int=interp1(t_1,s_tot,t); % Interpolate the data set(strain-time) at time t
s_r = -16; % Radial stress corresponding to pressure of primary coolant
dydt = zeros(2,1); % Create array for stress rates
dydt(1) = E/(1-v^2)*(s_int-crate(s_r,y(1),y(2))/vonmises(s_r,y(1),y(2))*((1-
0.5*v)*y(1)-(0.5-v)*y(2)-0.5*(1+v)*s_r));
% Equation for axial stress rate at time t
dydt(2) = E/(1-v^2)*(v*s_int-crate(s_r,y(1),y(2))/vonmises(s_r,y(1),y(2))*((v
-0.5)*y(1)-(0.5*v-1)*y(2)-0.5*(1+v)*s_r));
% Equation for hoop stress rate at time t
end
```

```
% ------------------------------------------------------------------------
% Function Name: vonmises
% Purpose: calculate the von Mises stress
% Inputs: radial stress, hoop stress, axial stress
% Outputs: von Mises stress
% ------------------------------------------------------------------------
function sig_vm = vonmises(sig_rr, sig_tt, sig_zz)
% sig_rr : radial stress, sig_tt : hoop stress, sig_zz : axial stress
sig_vm = (((sig_rr-sig_tt)^2+(sig_tt-sig_zz)^2+(sig_zz-sig_rr)^2)/2)^(0.5);
% von Mises stress equation
end
% ------------------------------------------------------------------------
% Function Name: crate
% Purpose: calculate the creep strain rate
% Inputs: radial stress, hoop stress, axial stress
% Outputs: creep strain rate
% ------------------------------------------------------------------------
function creeprate = crate(sig_rr,sig_tt,sig_zz)
% sig_rr : radial stress, sig_tt : hoop stress, sig_zz : axial stress
TM=2163.0; % Melting temperature
U0=126000.0; % Shear modulus under 300K
TEMP=600; % Temperature corresponding to primary coolant
U=U0*(1.0+(TEMP-300.0)/TM*(-0.50)); % Shear modulus under current temperature
ES=vonmises(sig_rr,sig_tt,sig_zz)/(1.732); % Effective stress
GS=0.3*10.0^(-6.0); % Grain size
% Diffusional creep
DEFFD=2.8*(10.0^(-5.0))*exp(-36805.39/TEMP)+ 15.71/GS*(10.0^(-15.0))*exp(-
23093.58/TEMP);
Diffusionrate=ES*36.52*DEFFD/TEMP/(GS^2.0);
```

```
% Power-law creep
DEFFP=2.8*(10.0^(-5.0))*exp(-36805.39/TEMP)+0.0016*((ES/U)^2.0)*exp(-
23093.58/TEMP);
Powerlawrate=2.355*(10.0^25.0)*U/TEMP*DEFFP*((ES/U)^4.3);
% Dislocation glide
% Obstacle-controlled glide
if (ES < 1109.03)
GlideG=10.0^(6.0)*EXP(-71331.52/TEMP*(1.0-ES/1109.03));
else
GlideG=1.0D10;
% if ES>1109.03 GlideG is very large so it should be dominated by GlideL
end
% Lattice-resistance-controlled glide
if (ES < 2180.03)
GlideL=10.0^(11.0)*((ES/U)^2.0)*EXP(-8417.12/TEMP*(1.0-
(ES/2180.03)^0.75)^(1.333));
else
GlideL=1.0D10;
% if ES>2180.03 GlideL is very large so the stress should relax almost
instantaneously
end
% Total creep rate
Drate=GlideG;
if (GlideL < Drate)
Drate=GlideL;
end
if (Powerlawrate > Drate)
Drate=Powerlawrate;
end
```

```
creeprate = (Diffusionrate+Drate)/1.732;
% Equivalent (uniaxial) deviatoric creep strain rate
end
```

Chapter 3 is reproduced from the publication:

K. Hong, J. R. Barber, M. D. Thouless and W. Lu, “Cracking of Cr-coated accident-tolerant fuel during normal operation and under power-ramping conditions”, Nuclear Engineering and Design, 353, 110275, 2019

Chapter 4 Effect of Power History on Pellet-Cladding Interaction

4.1 Introduction

Upon the initial start-up of light-water reactors, large thermal gradients are generated within the fuel pellets owing to the low thermal conductivity of UO_2. These gradients induce tensile hoop stresses at the outer surface of the pellet, which lead to fuel fragmentation [15]. As the cladding creeps down, and the fuel swells, contact between the fuel and cladding eventually occurs. The interaction between the crack edges in the pellet and the cladding introduces local singular stresses within the cladding. These local singular stresses can lead to cladding failure, which is occasionally observed during operation with significant power uprating [5], [16].

Several studies have investigated the interaction between the pellet and cladding, often termed pellet-cladding interaction (PCI). These include analytical studies conducted to predict the stress distribution [68], [69], and experimental studies to mimic PCI and to evaluate attributes associated with resistance to failure from PCI [70], [71]. Recently, finite-element simulations that incorporate various complex mechanisms, such as creep, fuel swelling, and thermal expansion have been performed to provide insight into how PCI can induce failure [72]–[75]. This recent work focused on a very specific loading scenario. However, since the phenomena involved in the PCI problem have distinct time-scales, and since frictional contact problems are inherently history-dependent, different loading histories can lead to very divergent results. Our interest in this chapter is to distinguish the types of power history that can lead to failure from PCI from the types of power history that can lead to more benign forms of PCI. We do this by modeling the evolution of

hoop stresses at the inner surface of the cladding under different loading scenarios, using detailed finite-element calculations, as described below.

4.2 Finite-element model

4.2.1 Geometry and boundary conditions

A finite-element model for a fuel rod was constructed as shown in Fig. 4-1, where the dimensions were defined at 300 K. This 2-D plane-strain model representing the middle cross-sectional plane of a fuel rod, which includes the UO_2 fuel pellet and Zircaloy cladding, was implemented using the commercial software ABAQUS. A 3-D model of the fuel rod might be ideal to capture the details of PCI, since a 2-D model does not, for example, account for the hourglass shape of pellet. However, a 2-D model can reasonably explain the interaction between the cracked fuel and cladding with a refined mesh at relatively a low computational cost.

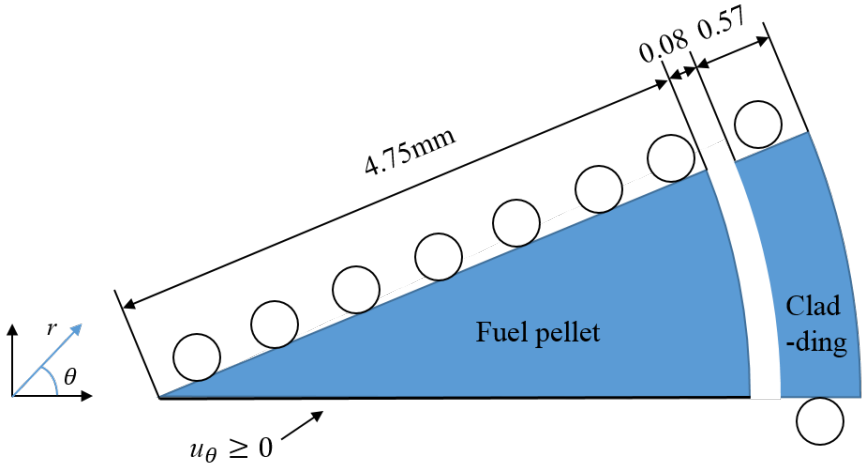

Figure 4-1: The fuel pellet was assumed to be fragmented into 8 pieces. 22.5° of the fuel assembly was modeled. A symmetrical boundary condition was applied along the $\theta = 22.5°$ plane within the fuel. A contact boundary was applied along the $\theta = 0°$ plane in the fuel (a crack plane). Thermal stresses held the crack surfaces together near the center of the pellet. Symmetry boundary conditions were applied at both $\theta = 0°$ and $\theta = 22.5°$ for the cladding.

Since experimental observations indicate that fuel pellets are fragmented into pieces during the initial start-up, with the number of pieces depending on the power level [15], we considered the case where there are 8 pieces. Therefore, we model half of a fragmented piece (so the angle in Fig. 4-1 is 22.5°) with symmetric boundary conditions. The cracked surface of the pellet $\theta = 0°$ is also a symmetry plane, and the boundary conditions there are equivalent to a frictionless hard contact with a rigid surface.

The gauge pressure on the outside of the cladding was assumed to be 12 MPa, representing the difference between the external coolant pressure and the internal helium pressure [22]. A hard-contact condition was used at the interface between the pellet and cladding to ensure no penetration. A Coulomb friction law was implemented at this contact using the Lagrange-multiplier method. The coefficient of friction between the pellet and cladding was set to be 0.7 [76]. The initial temperature of the fuel rod was set to be 300 K, but then allowed to heat up as power is generated within the fuel. The temperature of the outer surface of the cladding was set to 600 K, which is equivalent to the temperature of the primary coolant.

4.2.2 Mechanisms

The creep law for Zircaloy was taken from the deformation-mechanism map of Wang *et al*. [32], while that for UO_2 was taken from the deformation-mechanism map of Frost and Ashby [33]. Grain sizes, which affect creep, were assumed to be 50 μm for Zircaloy and 10 μm for UO_2. The swelling of UO_2, resulting from the accumulation of solid and gaseous fission products, was implemented using the MATPRO model [37]. The fuel expansion due to swelling can be partially offset during early irradiation by fuel densification induced by irradiation sintering. We therefore implemented the model from MATPRO [37] to incorporate fuel densification. The amount of

densification depends on the initial porosity of the fuel [62]. Other material parameters for the Zircaloy, UO_2, and helium were also taken from MATPRO [37].

4.2.3 Mesh refinement

We used first-order, coupled temperature-displacement, plane-strain elements with reduced integration for implicit calculations. Refined meshes were used near the corner of the cracked pellet and near the cladding inner surface at $\theta = 0°$ to capture any stress singularities near the contact between the cracked pellet and cladding. We confirmed that the mesh was fine enough by comparing the strength of singularity calculated from a finite-element simulation with analytical solutions for the geometry. Since creep relaxation causes the singularity to decrease with time, this validation was made for the case at T = 600 K, with no creep and a non-slip interface, resulting in an elastic singularity. The strength of this singularity was obtained by calculating the slope of the log-log plot of stress against the distance from the contact point along the inner surface of the cladding. The singularity from the finite-element calculation, 0.509±0.0005, agreed well with the analytical value of 0.5093 [77].

4.3 Results and discussion

The output of a nuclear power station is adjusted according to demand by the insertion of control rods into the reactor. If there is an increase in demand, the power level increases during what is known as power ramping. This leads to three possible power histories for which we consider the effects of PCI: (i) power ramping after contact has already been established between the cladding and fuel, (ii) power ramping before contact has been established, and (iii) normal operation with no power ramping. In the models presented below, the last scenario is considered as part of the first, so it is not addressed specifically in a separate section. Note that the return to

normal operation after a power ramp is specifically considered in our study.

4.3.1 Power ramping after contact

We implemented a power history based on a typical experimental protocol of power ramp tests, similar to that used for the TRANS-RAMP project [78], where a power ramp is established after a pre-conditioning period at nominal power [5]. The power history modelled in this section consists of eighteen months under normal conditions, followed by a month-long power ramp before returning to normal conditions. The thermal power generated per unit length of the fuel rod (linear heat rate (LHR) of the fuel) was assumed to be uniform and equal to 20 kW/m during normal operation, and 40 kW/m during the power ramp. The transitions between normal operation and the power ramp were assumed to occur as a step change in the power generation, considering the rapid ramp rate used for the power ramp tests [5]. However, we also considered the case with a ramp rate of 10 kW/m·min, instead of a step change. These calculations showed that a finite time-scale of the power transient has a negligible effect on the result, especially in terms of interaction between the cracked fuel and cladding, since the time-scale of heat transfer is relatively small compared to that of other mechanisms.

4.3.1.1 Opening of radial cracks within the pellet

Contact between the fragmented pellet (with a sharp corner at the crack mouth) and the cladding results in a singular stress field at the inner surface of the cladding. Since the direction of relative slip between the pellet and cladding determines the sign of the singular hoop stress, we tracked the crack-mouth opening of the radial crack in the pellet. This is shown in Fig. 4-2a, along with the corresponding gap between the pellet and cladding.

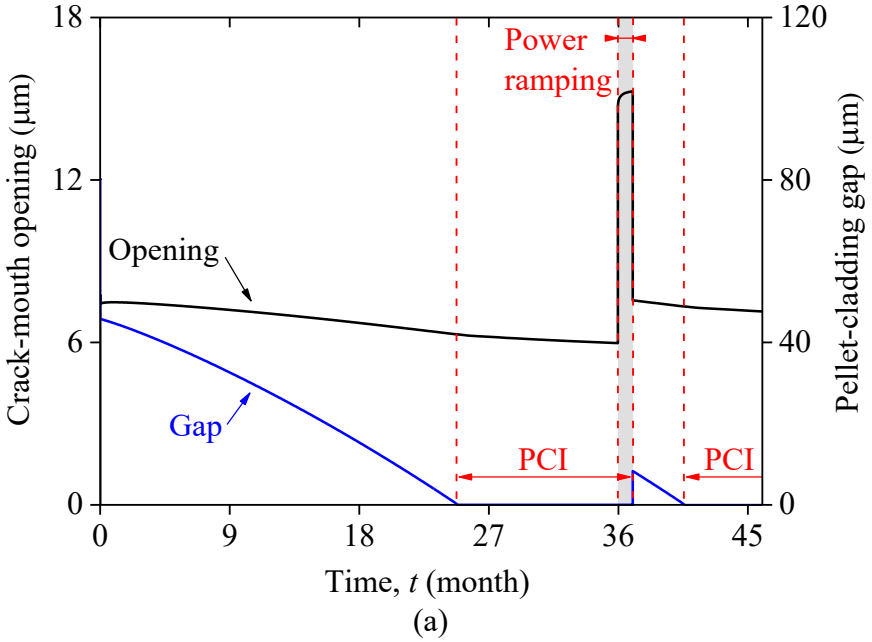

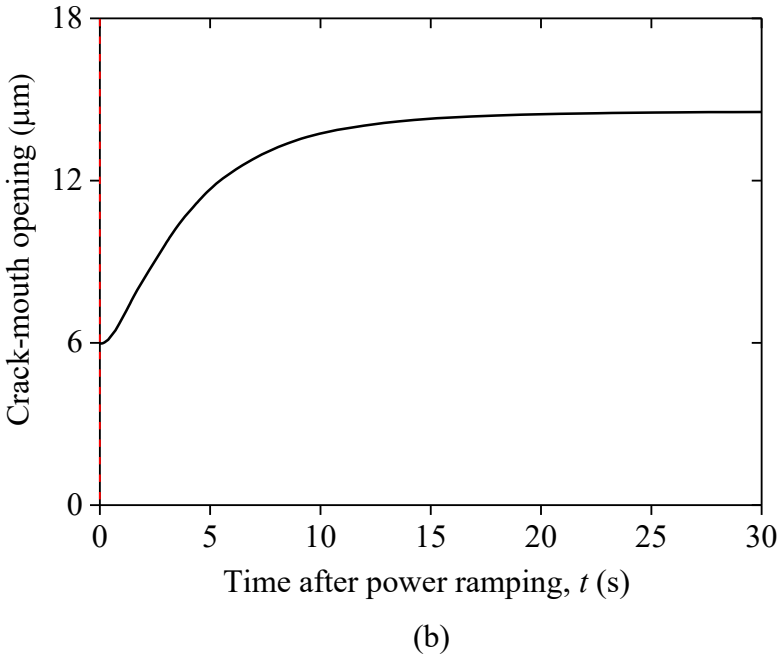

Figure 4-2: (a) The opening of the crack-mouth as a function of time for a cycle consisting of normal operation (LHR = 20 kW/m) for 36 months, a power ramp (LHR = 40 kW/m) for 1 month, and a return to normal operation. The shaded region shows power ramping. (b) A plot of crack-mouth opening as a function of time immediately after the beginning of the power ramp.

Upon start-up, the temperature within the pellet increases instantaneously and a large temperature gradient is established within the pellet. This temperature gradient leads to an immediate increase in the crack-mouth opening. (It should be noted that a uniform temperature increase (or a uniform swelling) expansion will not open up initially closed cracks). As the gap between the pellet and cladding decreases with time, owing to fuel swelling and creep-down of the cladding, the heat-transfer associated with the helium-filled gap increases. In addition, the thermal conductivity of UO_2 increases with decreasing temperature [37], so both the temperature and temperature gradient within the pellet are reduced after reaching a maximum 50 s after start-up, as shown in Fig. 4-3. These effects lead to a slight decrease in the crack-mouth opening before contact occurs at about 25 months, as shown in Fig. 4-2a.

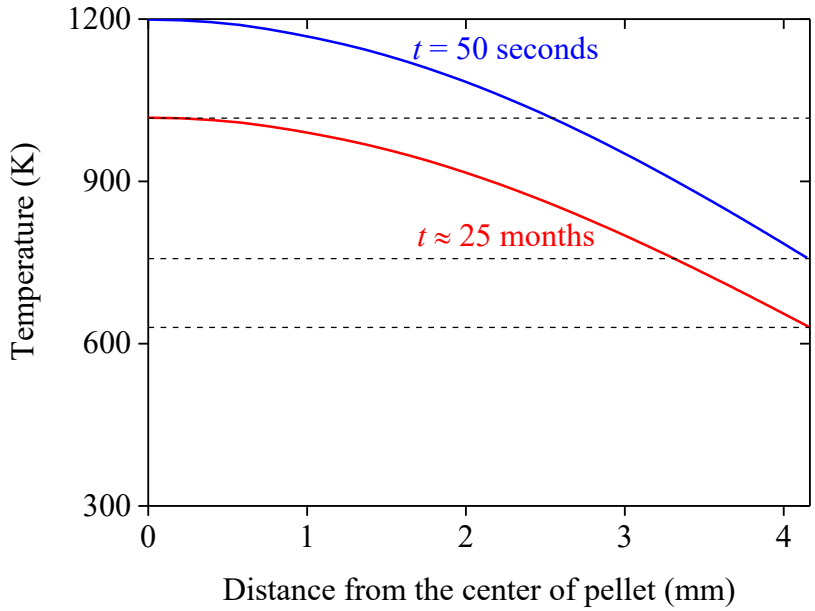

Figure 4-3: Radial temperature distribution for the pellet at different times, t, after the fuel rod is put into service. The temperature reaches a maximum at $t = 50$ seconds and decreases until contact occurs at $t \approx 25$ months.

After contact occurs, the system reaches a new thermal steady state within a minute. Although we anticipate some residual thermal contact resistance owing to the roughness of contacting surfaces after the gap closes [79], it is much lower than the thermal resistance of the helium-filled gap and is therefore neglected. We also note that this assumption makes the contact resistance change continuously between separation and contact, which ensures that the coupled thermoelastic contact problem is mathematically well-posed and stable [80]. While in contact with the cladding, the fuel swelling in radial direction is less than it would have been without contact. The contact pressure then causes lateral expansion, resulting in a decrease in the crack-mouth opening as shown in Fig. 4-2a. Though the decrease is not significant, we should note that it determines the sign of the singular stress near the contact with the crack mouth, which will be discussed in the following section.

Power ramping leads to rapid increases in both the temperature of the fuel pellet and the temperature gradient within it; this causes the crack to open up significantly during the period of the thermal transient period (within a minute), as shown in Fig. 4-2b. In addition, the thermal expansion of the pellet induces a high contact stress, which leads to enhanced creep of the cladding. As a result, the crack continues to open with time, even after the system reaches a thermal steady state; this can be seen within the power-ramping region of Fig. 4-2a.

During the period of increased power generation, the rate of fuel swelling increases, causing the cladding to creep outwards while in contact with the pellet. When the power decreases to its original level after power ramping, the thermal strains generated during the power ramp disappear; however, the permanent deformation associated with the creep and the swelling of the fuel remain. As a consequence, the pellet and cladding lose contact immediately after the return to normal operating conditions, and the crack opening decreases (see the right end of Fig. 4-2a). As

the normal operating conditions continue, contact eventually occurs again owing to swelling of the fuel and creep-down of the cladding, the local hoop stress at the inner surface of the cladding near the crack edge is compressive until another power ramp occurs. With a second power ramp of the same magnitude, the crack-mouth opening increases again to a value similar to that during the previous power ramp.

During operation, increase in the temperature of helium gas and the release of fission gases from the fuel can increase the internal pressure within the fuel rod [64]. Calculations using an increased helium pressure of 16 MPa showed that this leads to a delayed onset of PCI, due to the reduced rate of cladding creep-down. Fuel densification also delays the initiation of PCI. However, neither of these phenomena affects the sign of the local singular hoop stress induced by the interaction between the cracked fuel and cladding.

4.3.1.2 Evolution of the hoop stress at the inner surface of the cladding

Figure 4-4 shows the hoop stresses at the inner surface of the cladding at different times during normal operation after contact occurs. The deformation of the pellet associated with the presence of the crack leads to a gradual contact along the inner surface of the cladding. The contact is initiated next to the crack mouth (Fig. 4-4a); it then occurs near the center of the fuel fragment (Fig. 4-4c), and, finally, the two regions meet up (Fig. 4-4d). The far-field hoop stress away from the crack edge, increases owing to the fuel swelling. Since this sharp corner slips relative to the cladding in a direction that reduces the crack-mouth opening, the local hoop stresses are singular and compressive.

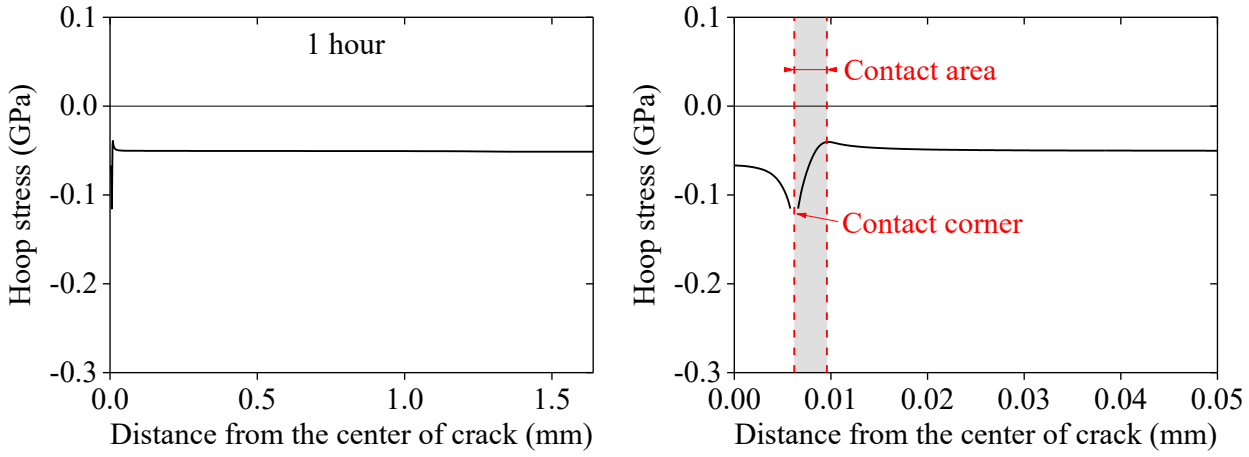
1 hour
Hoop stress (GPa)
Distance from the center of crack (mm)
Contact area
Contact corner

(a)

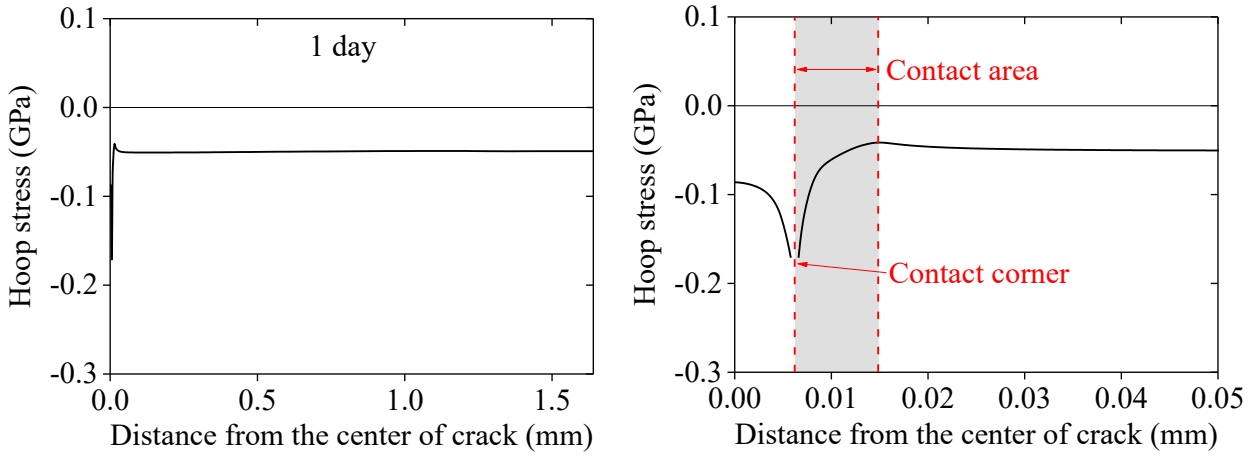
1 day
Hoop stress (GPa)
Distance from the center of crack (mm)
Contact area
Contact corner

(b)

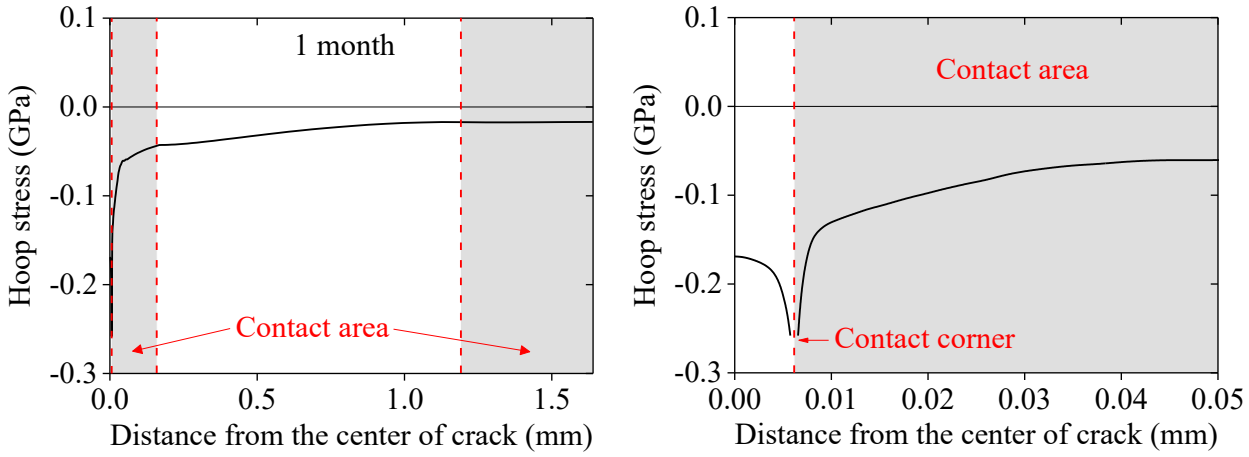
1 month
Hoop stress (GPa)
Distance from the center of crack (mm)
Contact area
Contact area
Contact corner

(c)

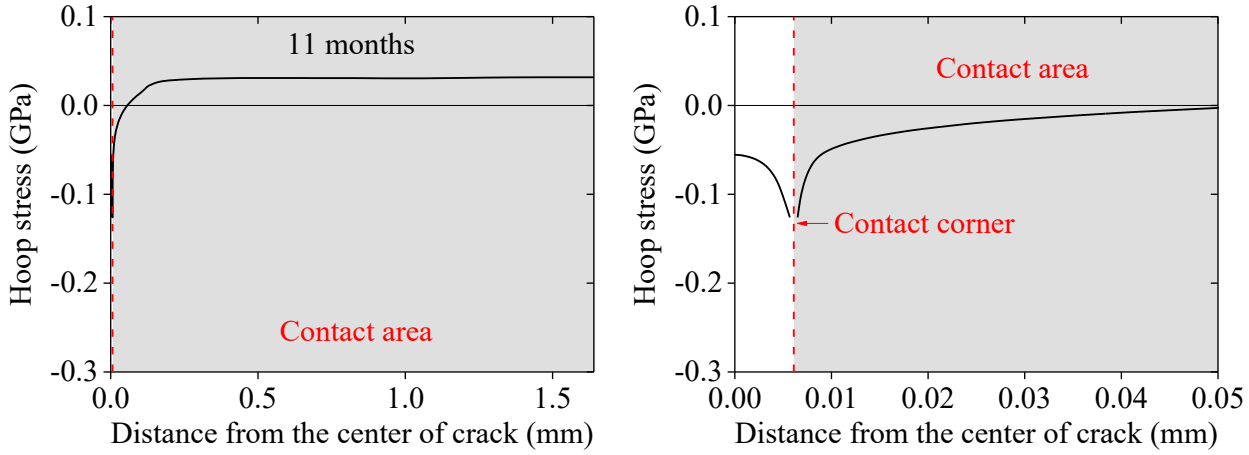

(d)

Figure 4-4: The distribution of the hoop stress at the inner surface of the cladding at different times after contact occurs under normal operating conditions. The figures to the right show details near the edge of the contact with the crack mouth. These figures correspond to (a) 1 hour, (b) 1 day, (c) 1 month, and (d) 11 months (immediately before the onset of the power ramp). The stresses at the edge of the crack are singular, as expected for contact with a creeping solid, so the stresses are shown as being discontinuous in that region.

When power ramping occurs, the thermal expansion of the pellet greatly increases the hoop stress in the cladding, as the pellet pushes the cladding radially outward, as in Fig. 4-5a. Note that the far-field hoop stress is not uniform along the cladding surface because the opening crack induces a non-uniform contact pressure on the inner surface of the cladding. The local hoop stress at the inner surface of the cladding around the vicinity of the crack mouth becomes tensile (positive) immediately after power ramping is established. It is associated with the opening of the crack owing to an increase in the thermal gradient within pellet, which agrees with previous simulation results [72]–[75].

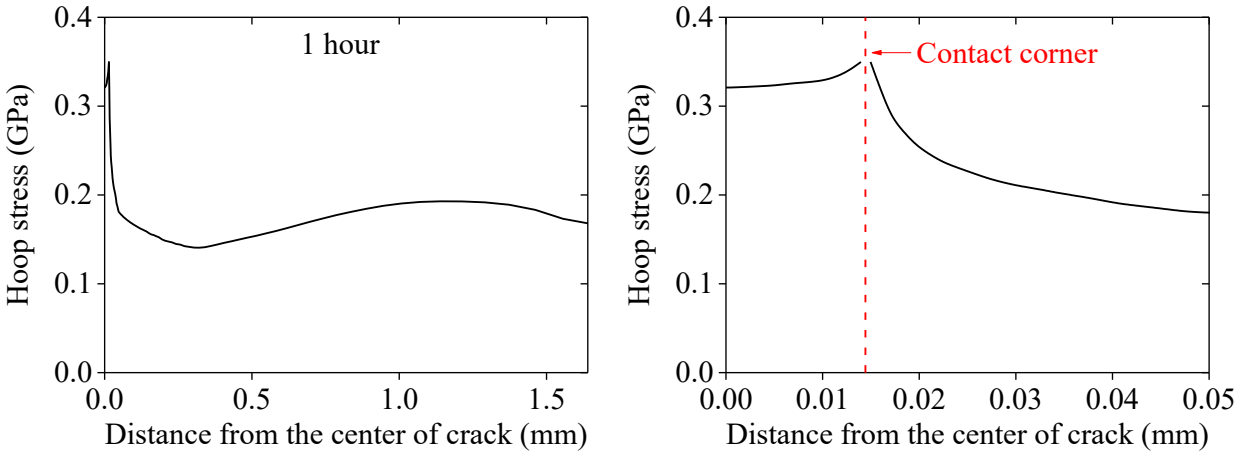
1 hour
Hoop stress (GPa)
Distance from the center of crack (mm)
Contact corner
Hoop stress (GPa)
Distance from the center of crack (mm)

(a)

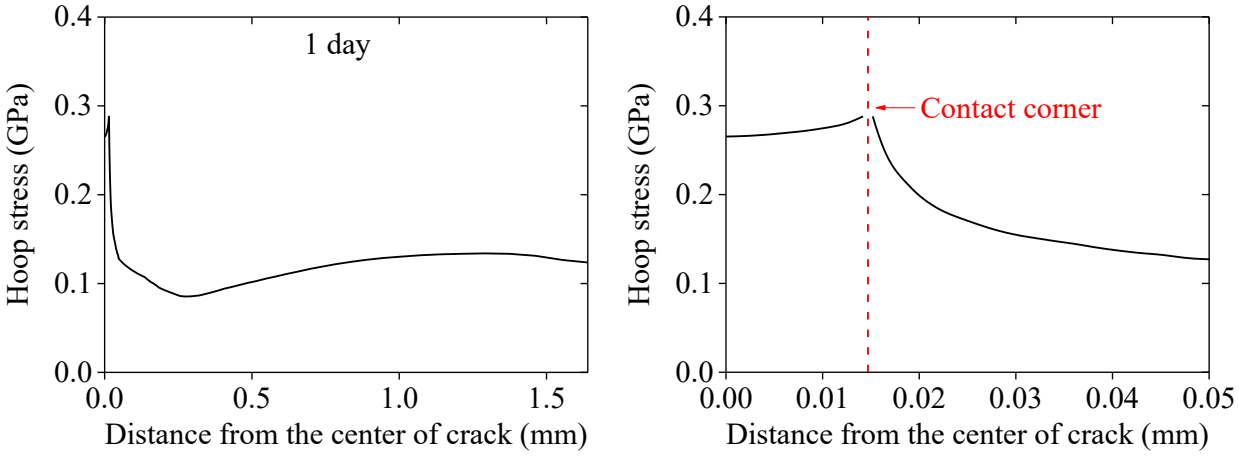
1 day
Hoop stress (GPa)
Distance from the center of crack (mm)
Contact corner
Hoop stress (GPa)
Distance from the center of crack (mm)

(b)

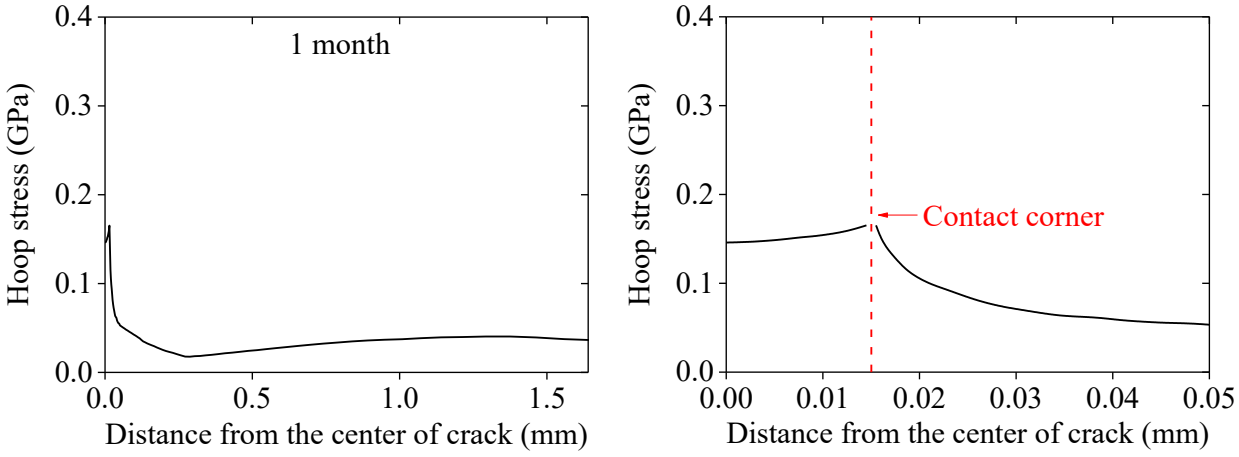
1 month
Hoop stress (GPa)
Distance from the center of crack (mm)
Contact corner
Hoop stress (GPa)
Distance from the center of crack (mm)

(c)

Figure 4-5: The distribution of hoop stresses at the inner surface of the cladding at (a) 1 hour, (b) 1 day, and (c) 1 month after the onset of a power ramp, with the power history of Fig. 4-2. The figures on the right show details near the crack mouth.

The far-field hoop stress relaxes with time, as shown by the plots of the hoop-stress distribution at different times in Fig. 4-5. This arises because the outward creep of the cladding relaxes the hoop stress more than the fuel swelling increases it. Also, both the strengths of the singularities for the hoop stresses and their magnitude decrease with time, owing to creep of the cladding.

During the transient period of power ramping, the deformation of the cladding is predominantly elastic, and the creep zone (the region where the creep strain exceeds the elastic strain) is confined to a very small region at the crack tip. However, the creep zone grows larger during steady-state power generation. Therefore, brittle failure might be anticipated during the transient period, whereas failure during the steady state is more likely to be associated with creep.

4.3.2 Power ramping before contact

If power ramping occurs before contact occurs during normal operation, PCI may be initiated either during the initial thermal transient period of the power ramp, or after the system reaches the thermal steady state of the power ramp, depending on the gap at the time when the power is ramped. We will investigate both cases in the following sections.

4.3.2.1 Contact occurring during the thermal transient of a power ramp

We first consider the case where contact is established during the thermal transient associated with power ramping. To model this scenario, we assumed that the fuel rod is subjected to eighteen months of normal operation (LHR = 20 kW/m), followed by a power ramp (LHR = 40 kW/m) for one month, and then continued operation at a normal level.

Under the conditions described above, contact first occurs during the transient period of power ramping (Fig. 4-6a). In contrast to the previous case where contact spreads with time along the inner surface of the cladding, contact occurs almost immediately (within a minute) after the onset of the power ramp as a result of rapid thermal expansion of the fuel pellet (Fig. 4-6b). In addition, an increased thermal gradient within the pellet causes the crack to open. This continues after contact occurs at a reduced rate owing to frictional interaction with the cladding. After the system reaches a thermal steady state, the crack-mouth opening continues to increase, as the cladding creeps radially outward (see section 4.3.1.1).

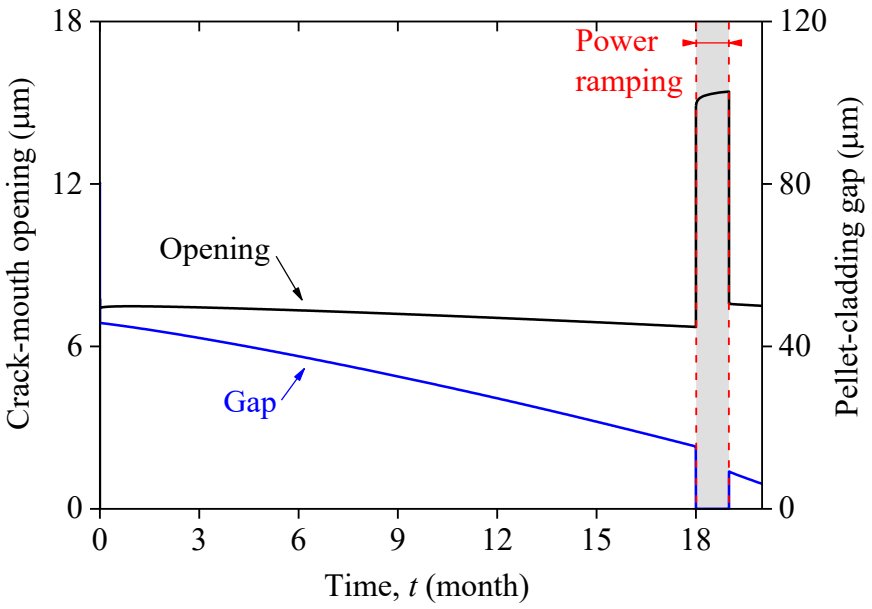

(a)

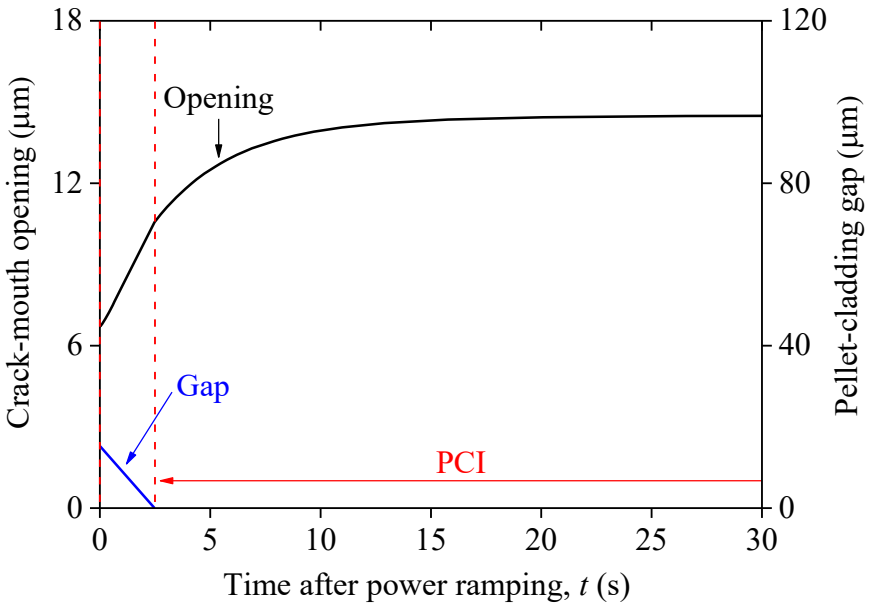

(b)

Figure 4-6: (a) The opening of the crack-mouth as a function of time for a cycle consisting of normal operation (LHR = 20 kW/m) for 18 months, a power ramp (LHR = 40 kW/m) for 1 month, and a return to normal operation. The shaded region shows power ramping. (b) A plot of crack-mouth opening as a function of time immediately after the beginning of the power ramp.

After a return to normal operation, the gap between the pellet and cladding again opens up owing to the thermal contraction of the pellet (Fig. 4-6a). The gap after the power ramp is smaller than it was before the power ramp because fuel swelling, which reduces the gap, dominates over creep of the cladding, which increases the gap. The crack-mouth opening decreases when normal operating conditions are restored owing to the decreased thermal gradient in the pellet (see section 4.3.1).

Figure 4-7 shows the evolution of the hoop stress at the inner surface of the cladding after contact occurs. Since the crack keeps on opening, the local hoop stress is tensile. The result is qualitatively similar to that described for the previous scenario (section 4.3.1 and Fig. 4-5).

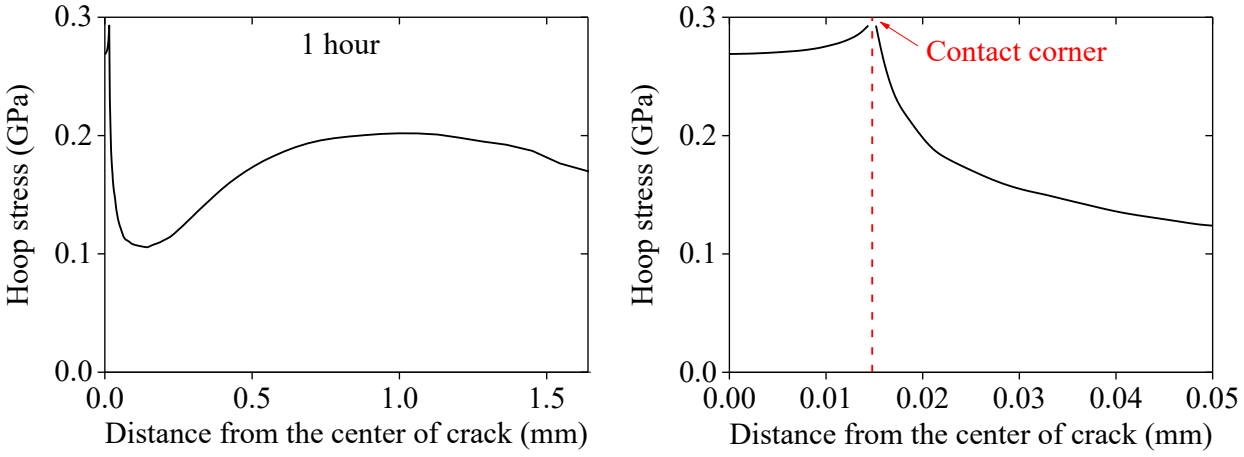
1 hour
Hoop stress (GPa)
Distance from the center of crack (mm)
Contact corner
Hoop stress (GPa)
Distance from the center of crack (mm)

(a)

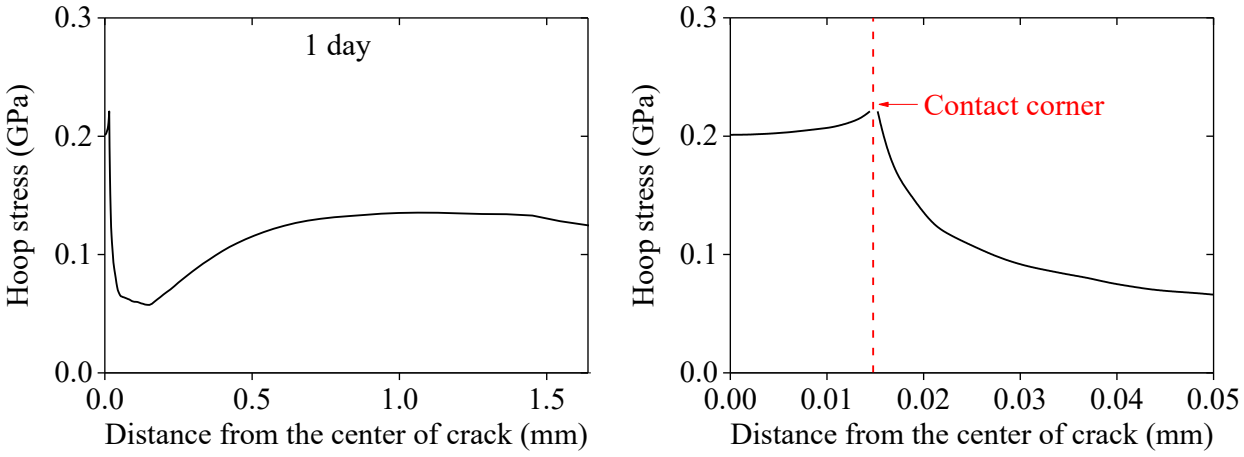
1 day
Hoop stress (GPa)
Distance from the center of crack (mm)
Contact corner
Hoop stress (GPa)
Distance from the center of crack (mm)

(b)

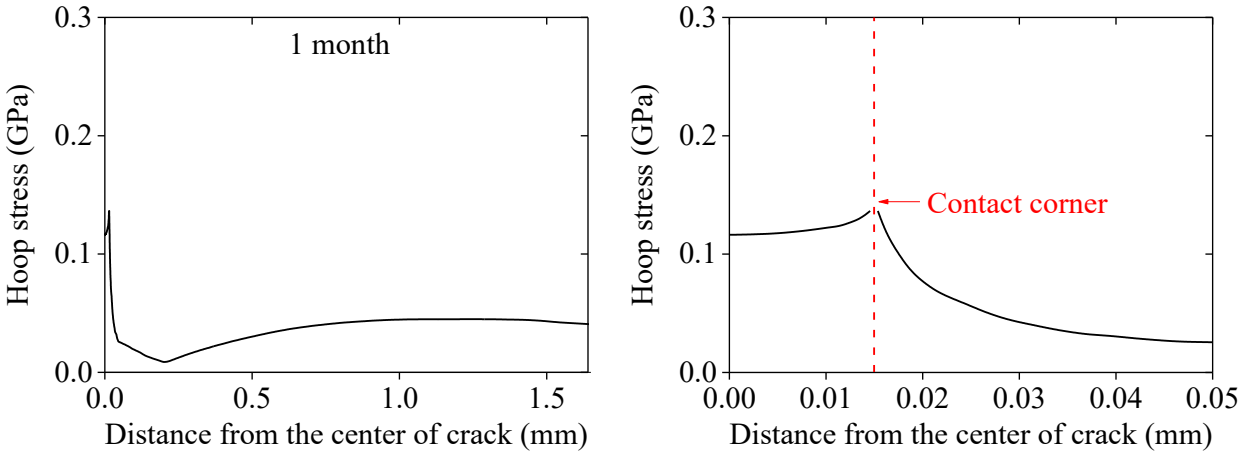
1 month
Hoop stress (GPa)
Distance from the center of crack (mm)
Contact corner
Hoop stress (GPa)
Distance from the center of crack (mm)

(c)

Figure 4-7: The distribution of hoop stresses at the inner surface of the cladding at (a) 1 hour, (b) 1 day, and (c) 1 month after the onset of a power ramp, with the power history of Fig. 4-6. The figures on the right show details near the crack mouth.

4.3.2.2 Contact occurring during thermal steady state of a power ramp

We finally consider the case where PCI is initiated during the thermal steady state of a power ramp. For PCI not to occur during the transient period, the gap at the instant of power ramping needs to be large enough, as would be the case if the power ramp occurs very early during operation, such as 9 months after the initial start-up.

Figure 4-8a shows that while a power ramp may not be big enough to close the gap between the pellet and cladding, it does causes a large decrease in the gap within a few seconds (Fig. 4-8b). The gap is subsequently closed by further swelling of the fuel and by the increased creep rate of the cladding associated with the higher temperatures of a power ramp. After contact, the crack closes because of the fuel swelling. After normal operating conditions are restored, the gap between the pellet and cladding opens up again, and the crack closes, as before (section 4.3.1.1).

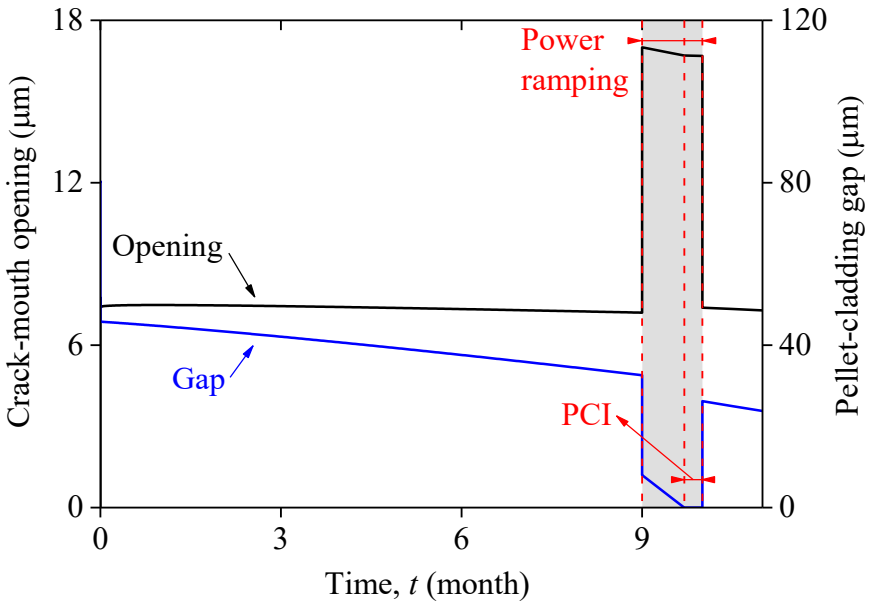

(a)

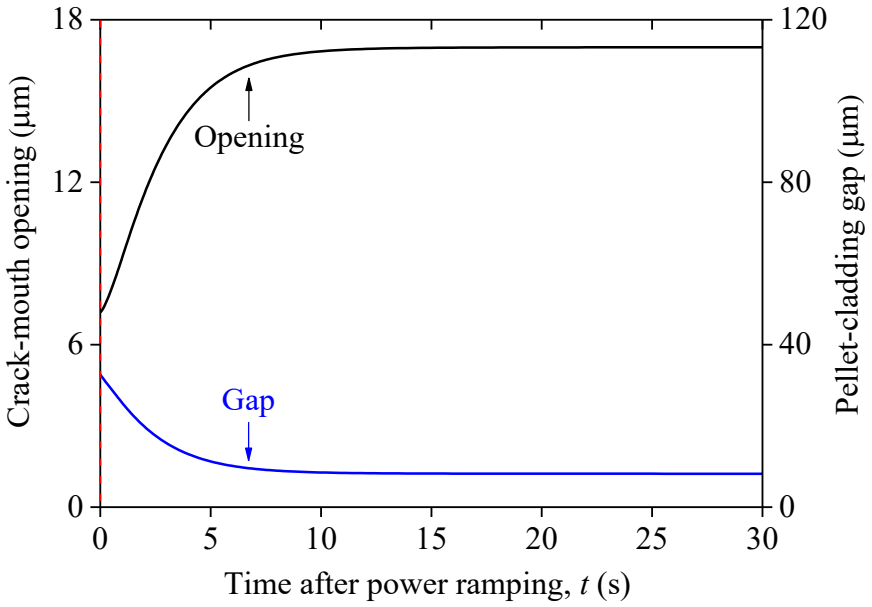

(b)

Figure 4-8: (a) The opening of the crack-mouth as a function of time for a cycle consisting of normal operation (LHR = 20 kW/m) for 9 months, a power ramp (LHR = 40 kW/m) for 1 month, and a return to normal operation. The shaded region shows power ramping. (b) A plot of crack-mouth opening as a function of time immediately after the beginning of the power ramp.

In this case, the local hoop stress remains compressive, regardless of the dwell time (Fig. 4-9). We note that the result is qualitatively similar to that of the previous scenario (section 4.3.1 and Fig. 4-4). The local compressive hoop stresses help to suppress PCI failure. Therefore, if failure occurs under this condition, it is possible only in regions away from the crack, and is caused by the far-field tensile hoop stress induced by fuel swelling.

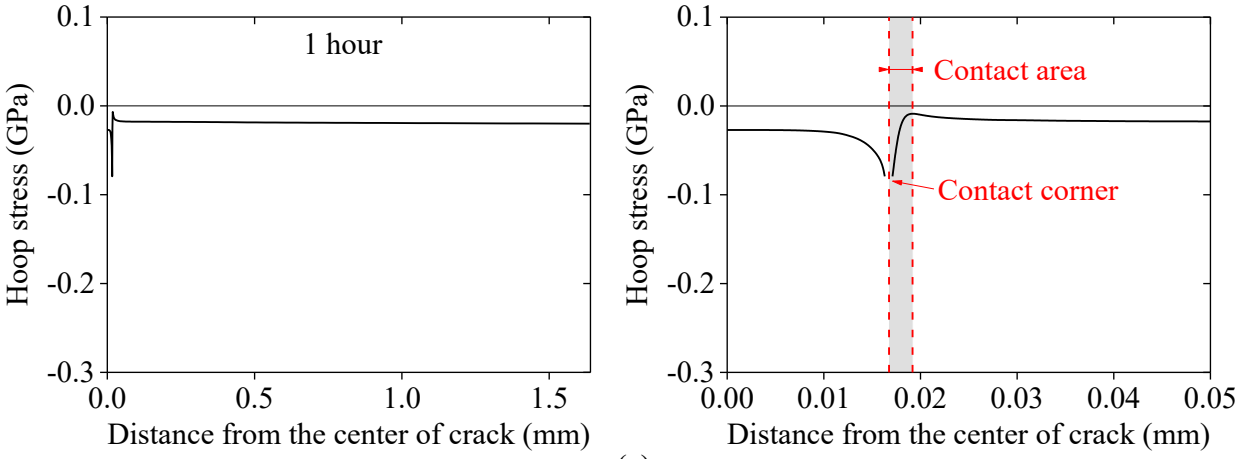
1 hour
Hoop stress (GPa)
Distance from the center of crack (mm)
Contact area
Contact corner

(a)

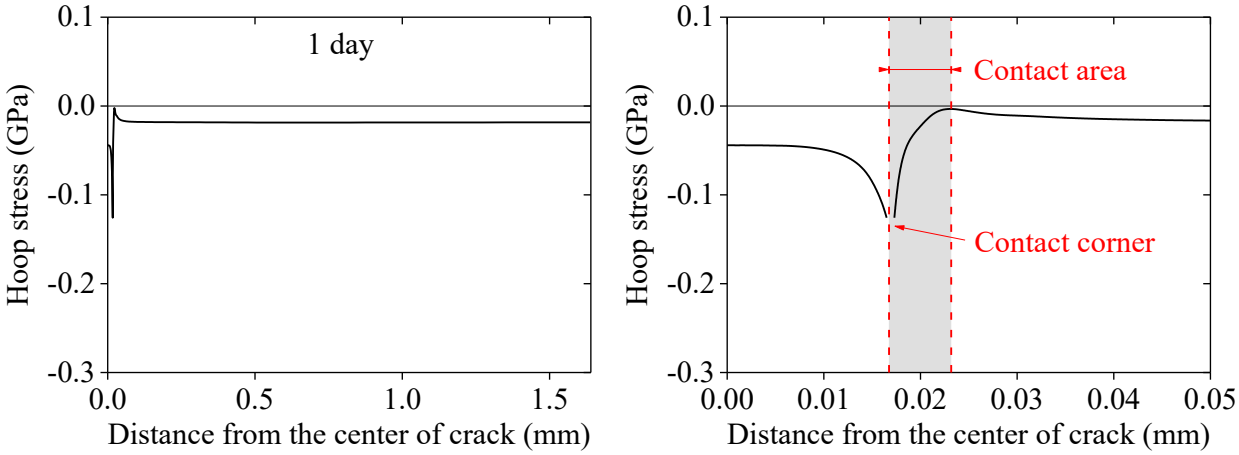
1 day
Hoop stress (GPa)
Distance from the center of crack (mm)
Contact area
Contact corner

(b)

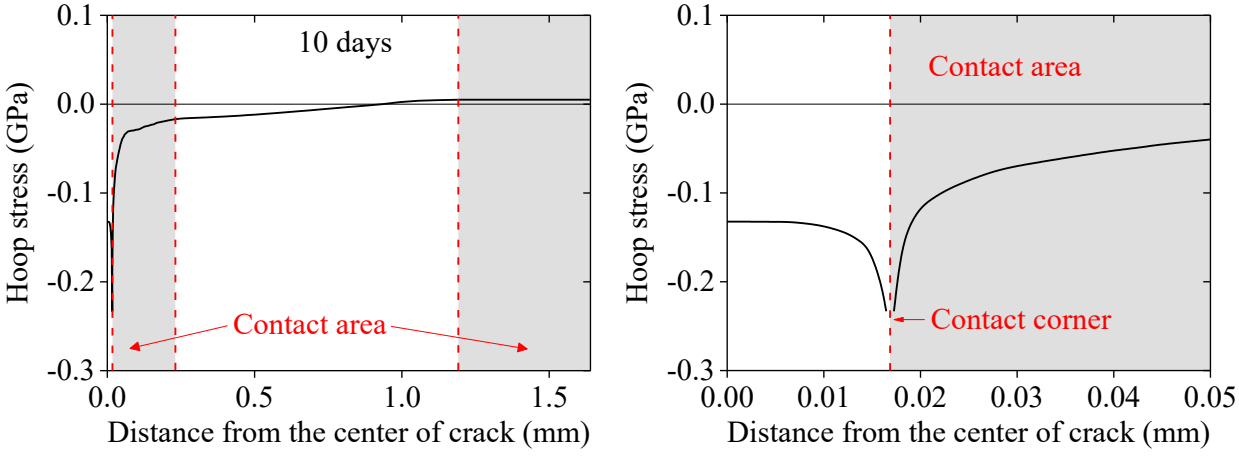
10 days
Hoop stress (GPa)
Distance from the center of crack (mm)
Contact area
Contact area
Contact corner

(c)

Figure 4-9: The distribution of hoop stresses at the inner surface of the cladding at (a) 1 hour, (b) 1 day, and (c) 10 days after the onset of a power ramp, with the power history of Fig. 4-8. The figures on the right show details near the crack mouth.

4.4 Conclusions

We have investigated conditions at which PCI failure may occur by considering some of representative power histories. The results can give an insight into developing safety criteria for operation of reactors. Finite-element models have been developed to study the evolution of the hoop stresses at the inner surface of the cladding for different power histories. The power history significantly affects possible PCI failure. It has been found that the local stresses in the vicinity of the crack can be tensile or compressive depending on when contact between the cladding and pellet occurs. During the thermal transient period of a power ramp, PCI occurs in such a way that the crack-mouth opens up in response to the increased temperature gradient within the pellet. The crack continues to open further, even after the system reaches a thermal steady state (during the power ramp), owing to enhanced creep of the cladding. The result is valid regardless of when contact is initiated, before or during power ramping. However, PCI initiated during the thermal steady state for either a power ramp or normal operation leads to crack opening decrease controlled by fuel swelling.

Based on results of this chapter, we can conclude that high local tensile hoop stresses are induced if an interaction between the pellet and cladding is initiated either before power ramping or during the transient period of a power ramps. Conversely, local compressive hoop stresses are induced if the interaction is during the steady state portions of normal operation or a power ramp. Therefore, PCI failure near the crack tip might be anticipated (by either brittle failure during the

transient power ramp or failure during the steady-state power ramp) in the former case, while it is expected to be suppressed in the latter case.

Chapter 4 is reproduced from the publication:

K. Hong, J. R. Barber, M. D. Thouless and W. Lu, “Effect of power history on pellet-cladding interaction”, Nuclear Engineering and Design (under review)

Chapter 5 Asymptotic Stress Fields for Complete Contact Between Dissimilar Materials

5.1 Introduction

If an elastic body with a sharp corner is pressed against an elastic half-plane, the stress field near the corner can be characterized by an asymptotic or eigenfunction series

$$\sigma_{ij}(r,\theta) = \sum_{n=1}^{\infty} K_n r^{\lambda_n - 1} f_{ij}^n(\theta) \tag{5.1}$$

[81], where the coordinate system (r,θ) is defined in Fig. 5-1(a), and the constants K_n [often called 'generalized stress-intensity factors'] depend on the far-field loading of the bodies. The eigenvalues, λ_n, and the corresponding eigenfunctions, $f_{ij}^n(\theta)$, are obtained by considering a single term of the series, and solving the resulting elasticity problem with traction-free conditions at the exposed edges and appropriate contact conditions at the interface $\theta = 0$.

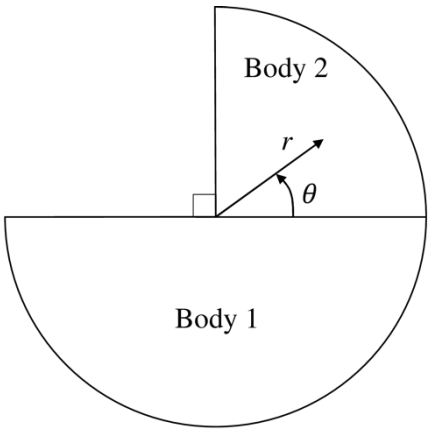

(a)

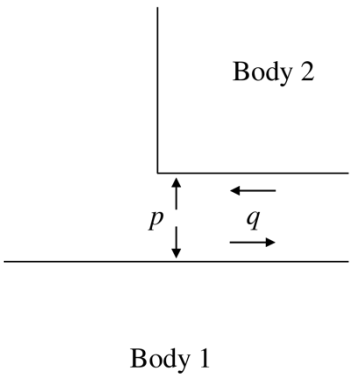

(b)

Figure 5-1: **(a)** A quarter-plane [right-angle wedge] indenting a half-plane. **(b)** Sign convention for normal traction p and shear traction q. At a trailing edge, $q = fp$ and at a leading edge, $q = -fp$.

Energetic considerations restrict admissible eigenvalues to the range $\lambda_n > 0$, or if complex, $\Re(\lambda_n) > 0$. Conventionally, the eigenvalues are arranged in order of ascending real part, so the stress field very near the corner is dominated by the first term in equation (5.1). In particular, if a quarter-plane is pressed onto a half-plane as shown in Fig. 5-1(a), the frictional [shear] traction $q(r)$ and the contact pressure $p(r)$ near the corner can be approximated as

$$p(r) = -\sigma_{\theta\theta}(r,0) \approx -K_1 r^{\lambda_1 - 1} f^1_{\theta\theta}(0);$$
$$q(r) = \sigma_{\theta r}(r,0) \approx K_1 r^{\lambda_1 - 1} f^1_{\theta r}(0), \tag{5.2}$$

where the sign convention for p and q is shown in Fig. 5-1(b). Important features of the contact problem can often be deduced by considering this term alone [82]. We define the eigenfunctions such that $f^1_{\theta\theta}(0) > 0$, so the unilateral contact condition $p > 0$ is satisfied only for $K_1 < 0$. This is in accordance with the sign convention used in fracture mechanics.

The form of the eigenfunction series (5.1) depends on whether or not interface slip occurs near the edge. We shall identify the two cases by the superscripts (s) [slip] and (a) [adhered] respectively. In the case of slip, $q = \pm fp$ where f is the friction coefficient, and the sign depends on the direction of slip. The motion is described as trailing-edge slip if body 2 moves to the right in Fig. 5-1(b), and leading-edge slip if it moves to the left [83]. The frictional tractions must oppose the slip motion, and hence, $q > 0$ at a trailing edge and $q < 0$ at a leading edge. These inequalities can be used to characterize the edge conditions even in the case where there is no slip. It must be emphasized that this terminology relates to asymptotic conditions at the corner, and is not necessarily connected to the macroscopic conditions of the problem. For example, if a rectangular block is pressed against a half-plane and then subjected to normal and shear loads P, Q

respectively, it might seem more natural to define leading and trailing edges with reference to the direction of Q. However, the asymptotic arguments presented here can be applied to more complex geometries where such a definition would be impractical.

If there is no slip at the edge, the ratio of the shear and normal tractions in the K_1-dominated zone is defined by

$$\frac{q(r)}{p(r)} = -f_a \qquad \text{where} \qquad f_a = \frac{f_{\theta r}^{1(a)}(0)}{f_{\theta\theta}^{1(a)}(0)} \tag{5.3}$$

and is independent of $K_1^{(a)}$ and r. Churchman and Hills [82] showed that $f_a = 0.543$ for the case where the materials have the same elastic properties and argued that if the coefficient of friction at the interface $f > f_a$ there can be no slip in the corner [*regardless of the far-field loading or geometry*]. If $K_1^{(a)} > 0$, the corner must separate, whereas if $K_1^{(a)} < 0$, it will be in contact with no slip and the shear traction $q < 0$ in Fig. 5-1(b), which by the above convention defines a leading edge. By contrast, if $f < f_a$, 'stick' is impossible, and the corner must either slip or separate.

Further information about the local fields can be obtained by including the second term in the asymptotic series (5.1). Since $\lambda_1^{(a)} \neq \lambda_2^{(a)}$, the constants $K_1^{(a)}$, $K_2^{(a)}$ involve different dimensions of length and hence we can define a problem-specific length scale

$$d_0 = \left(\frac{K_1^{(a)}}{K_2^{(a)}}\right)^{\frac{1}{\lambda_2^{(a)} - \lambda_1^{(a)}}} \tag{5.4}$$

[84]. This gives some indication of the range $r < d_0$ in which the first term in the series is likely to be dominant, but in partial slip problems with $f < f_a$, it also allows us to estimate the length of the slip zone at the edge of the contact, as a multiple of d_0, that depends only on the coefficient of friction [84]. Many of these results were extended to the case of dissimilar materials by Kim *et al.* [85].

Notice that these effects are typically characterized by the adhered asymptotic series, even in cases where stick is impossible in the corner. In that case, we anticipate the existence of $K_1^{(a)}$-dominated zone *away* from the edge, with an embedded corner zone involving slip and/or separation, whose properties are determined by the first two terms of the surrounding asymptotic series. The situation is analogous to that in LEFM, where we anticipate a small region of non-linear deformation near the crack tip whose characteristics are determined by the mode I and mode II stress-intensity factors.

If slip extends to the corner, the local field (5.1) will be determined by the slip asymptotic, with the leading term defining the tractions as

$$p(r) \approx -K_1^{(s)} r^{\lambda_1^{(s)}-1};$$

$$q(r) \approx \pm f K_1^{(s)} r^{\lambda_1^{(s)}-1}, \tag{5.5}$$

where the sign depends on the direction of slip. Here, we have chosen to normalize the eigenfunctions such that $f_{\theta\theta}^{1(s)}(0) = 1$. Karuppanan *et al.* [83] considered the case where an elastic block slides over a half-plane, so that $q = \pm fp$ in any contact zone. For the trailing edge, they identified two critical friction coefficients, f_b and f_c, such that for $f < f_b$, the first 'slip' eigenvalue $\lambda_1^{(s)} < 1$ and hence the asymptotic stress field is singular, whereas for $f_b < f < f_c$, $\lambda_1^{(s)} > 1$ and the field is bounded, with stresses and tractions tending to zero in the corner. For $f > f_c$ [$> f_b$], $\lambda_1^{(s)}$ becomes complex, implying oscillatory tractions near the corner. There will then exist regions where the contact pressure is negative, which violates the Signorini contact inequalities. It was argued that this implies slip at the trailing edge is impossible, and, therefore, a small region near the trailing edge must separate. Karuppanan *et al.* [83] verified this by solving the edge contact problem under unilateral conditions, using a distribution of climb and glide dislocations to model

the displacement discontinuities. Also, finite-element studies of particular contact problems confirm these conclusions.

At a leading edge, the first eigenvalue $\lambda_1^{(s)}$ is real for all friction coefficients and defines a singular stress field. However, if $f > f_a$ [defined in equation (5.3)], leading-edge slip can only occur under gross-slip [sliding] conditions. For contacts involving partial slip, a leading edge must either stick or separate if $f > f_a$.

Except for [85], the above studies were all restricted to the case of elastically similar materials, but, in practice, complete contact problems are frequently encountered between engineering components with different elastic properties. For example, in nuclear reactors a complete contact can occur between a fragmented fuel pellet and cladding during a power transient [5]. This induces high tensile hoop stresses at the contact edges, leading to a pellet-cladding interaction (PCI) failure. In the present chapter, we therefore propose to examine the effect of elastic mismatch on the nature of the eigenvalues in equation (5.1) and on the critical coefficients of friction $f_a,\ f_b,\ f_c$. Hence, we can anticipate the qualitative behaviour of a contact edge under both partial-slip and gross-slip conditions.

5.2 Asymptotic analysis

Plane-strain contact problems involving dissimilar materials are most efficiently characterized in terms of the Dundurs bimaterial parameters, α and β, defined as

$$\alpha = E^* \left[\frac{(1-\nu_1)}{2G_1} - \frac{(1-\nu_2)}{2G_2} \right];$$

$$\beta = E^* \left[\frac{(1-2\nu_1)}{4G_1} - \frac{(1-2\nu_2)}{4G_2} \right] \tag{5.6}$$

[66], where G, ν denote the shear modulus and Poisson's ratio respectively, the indices refer to the materials of bodies 1 and 2 in Fig. 5-1, and the contact modulus E^* is defined such that

$$\frac{1}{E^*} = \left[\frac{(1-\nu_1)}{2G_1} + \frac{(1-\nu_2)}{2G_2}\right]. \tag{5.7}$$

With this notation, the characteristic equation defining the eigenvalues $\lambda_i^{(s)}$ for the slipping interface is [86], [87]

$$(1+\alpha)\cos(\lambda\pi)\left[\sin^2\left(\frac{\lambda\pi}{2}\right) - \lambda^2\right] + \frac{1-\alpha}{2}\sin^2(\lambda\pi)$$

$$\pm f sin(\lambda\pi)\left\{(1-\alpha)\lambda(1+\lambda) - 2\beta\left[\sin^2\left(\frac{\lambda\pi}{2}\right) - \lambda^2\right]\right\} = 0, \tag{5.8}$$

where the positive sign should be taken for trailing-edge slip and the negative sign for leading-edge slip.

In order to determine the critical friction coefficient f_a, below which slip must occur at the corner of a leading edge, from equation (5.3), we also need the characteristic equation for the eigenvalues $\lambda_i^{(a)}$ for the adhered interface, which is [77], [85]

$$A\beta^2 + B\alpha\beta + C\alpha^2 - B\beta + 2D\alpha + F = 0, \tag{5.9}$$

where

$$A = 4\left[\sin^2\left(\frac{\lambda\pi}{2}\right) - \lambda^2\right]\sin^2(\lambda\pi)\,;$$

$$B = 4\lambda^2\sin^2(\lambda\pi); \quad C = \sin^2\left(\frac{\lambda\pi}{2}\right) - \lambda^2\,;$$

$$D = (2\lambda^2 - 1)\sin^2(\lambda\pi) + \sin^2\left(\frac{\lambda\pi}{2}\right) - \lambda^2\,;$$

$$F = \sin^2\left(\frac{3\lambda\pi}{2}\right) - \lambda^2\,. \tag{5.10}$$

5.2.1 Nature of the eigenvalue $\lambda_1^{(s)}$ for edge slip

If Poisson's ratio is restricted to the range $0 \leq \nu_1, \nu_2 \leq 0.5$, the values of α, β must lie within the parallelograms shown in Fig. 5-2. These figures show the nature of the first eigenvalue $\lambda_1^{(s)}$ of equation (5.8) for four different coefficients of friction. In each region, the first term refers to $\lambda_1^{(s)}$ at a trailing edge and the second to that at a leading edge. For example, for the far left region of each figure, $\lambda_1^{(s)}$ is oscillatory and the stress field is bounded [i.e. $\Re(\lambda_1^{(s)}) > 1$] at a trailing edge, and real and singular [$\lambda_1^{(s)} < 1$] at a leading edge.

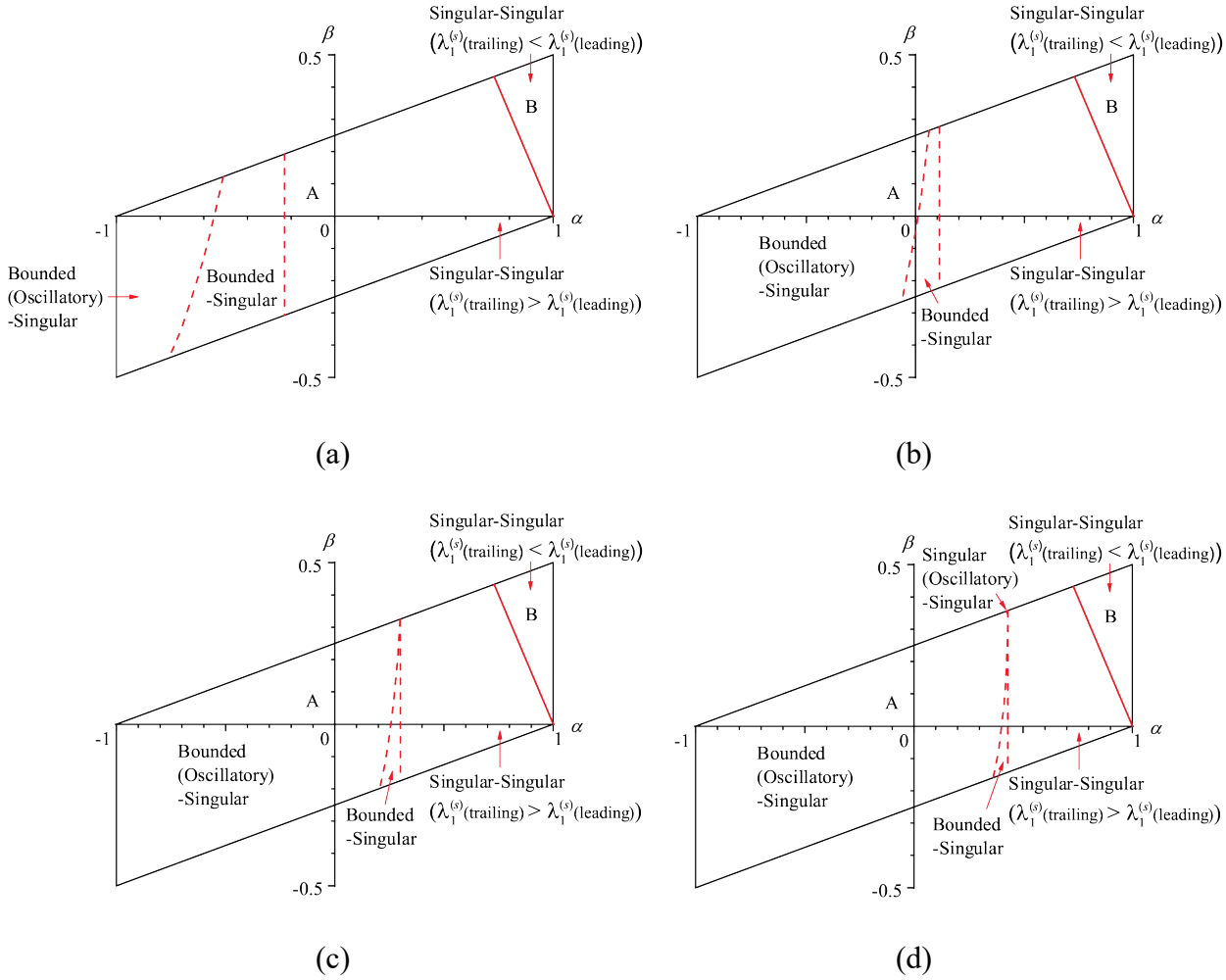

Figure 5-2: Characteristics of the first slip eigenvalue $\lambda_1^{(s)}$ [trailing edge – leading edge] with different friction coefficients: (a) $f = 0.2$, (b) $f = 0.4$, (c) $f = 0.6$, (d) $f = 0.8$.

In region *B* on the right side of these figures, $\lambda_1^{(s)}$ is real, and the stress field is singular at both edges for all friction coefficients. The eigenvalue is a continuous monotonic function of f, but $\lambda_1^{(s)}$(trailing) $< \lambda_1^{(s)}$(leading) in region B, whereas $\lambda_1^{(s)}$(trailing) $> \lambda_1^{(s)}$(leading) in region *A* as long as $\lambda_1^{(s)}$ is real. The boundary between these regions is independent of the friction coefficient.

In region A, the characteristics of the eigenvalues depend on the coefficient of friction as well as the material properties, as shown in Fig. 5-2. The case of similar materials [$\alpha = \beta = 0$] lies within this region, so it is convenient to start by summarizing the behaviour in this case [82], [83], to serve as a reference for the more general case.

5.2.2 Similar materials

Figure 5-3 shows the dependence of the first slip eigenvalue $\lambda_1^{(s)}$ on f, including the real and imaginary parts in the range where $\lambda_1^{(s)}$ is complex. In this figure, we identify the critical friction coefficients f_b, f_c and f_a, the last being determined from the eigenfunctions of the adhered equation (5.9). Recall that f_a characterizes the behaviour of a leading edge and f_b, f_c characterize that of a trailing edge.

At a leading edge, the asymptotic field is always singular and it will involve slip if $f < f_a$. For $f > f_a$, the leading edge must stick [except in the case of gross slip] and the corresponding eigenvalue is determined from equation (5.9). Notice that if the tangential load is increased towards the gross slip limit with $f > f_a$, the leading edge must remain stuck until this limit is reached, when there will be a discontinuous change to a sliding solution, since the slip eigenvalue is then lower than that for stick. The transition to full sliding was examined by Flicek *et al.* [83] using a finite-element solution.

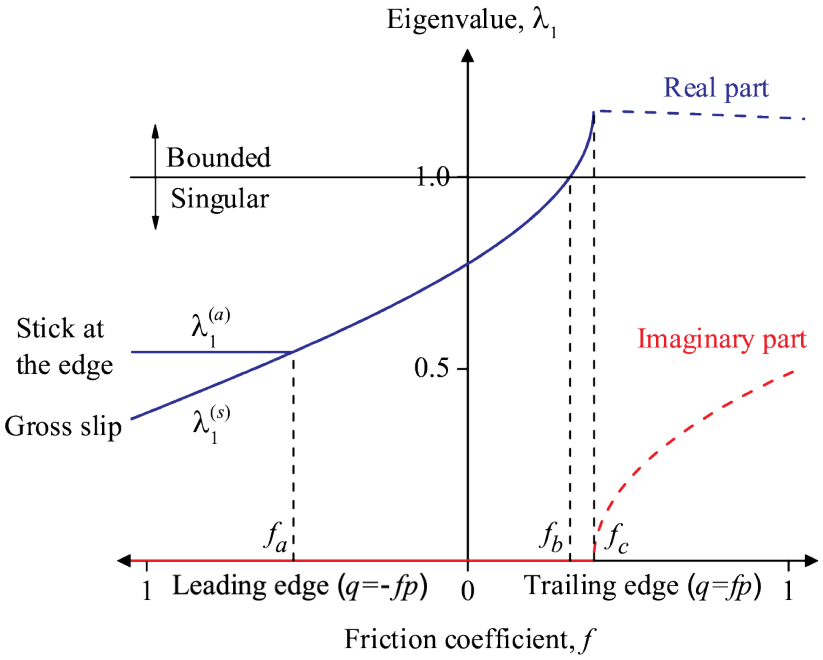

Figure 5-3: Lowest eigenvalue .vs friction coefficient for contact between elastically similar materials ($\alpha = \beta = 0$).

At a trailing edge, stick is impossible for all values of f and we must have either slip or separation depending on the sign of $K_1^{(s)}$ in the *slip* asymptotic series. In the case of slip, the asymptotic stress field is then singular for $f < f_b$ and bounded for $f_b < f < f_c$. Finally, for $f > f_c$, we always obtain separation in the corner.

5.2.3 Dissimilar materials

In the more general case of dissimilar materials, the principal effect of the bimaterial parameters α, β is to change the values of the critical friction coefficients f_a, f_b, f_c. However, as long as these three coefficients are defined, the qualitative behaviour of the system remains the same as for similar materials, and all the statements in Section 5.2.2 remain true. This applies throughout the region labelled A_1 in Fig. 5-4, where the Dundurs' parallelogram is partitioned depending on the relative magnitudes of the critical friction coefficients in cases where these can be defined.

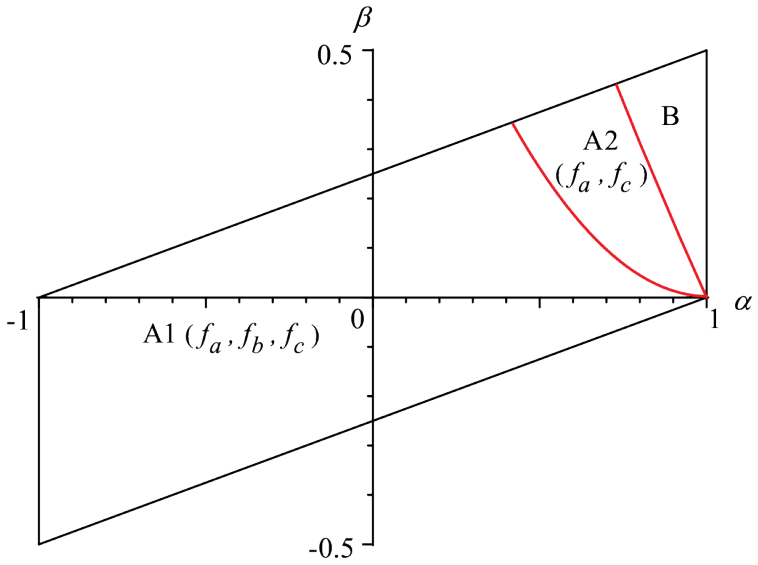

Figure 5-4: Partition of the Dundurs parallelogram.

For material combinations in region A_2, the slip eigenvalue becomes complex before reaching unity, so f_b is not defined. Since f_a and f_c are still defined, the contact edge behaviour is qualitatively similar to that in region A_1, except that in the case of slip, the local stress field is always singular regardless of friction coefficient. Recall that throughout region A $[A_1 \cup A_2]$, $\lambda_1^{(s)}$(trailing) $> \lambda_1^{(s)}$(leading) for $f < f_c$.

In region B, $\lambda_1^{(s)}$ is real and the stress field is singular for all friction coefficients and $\lambda_1^{(s)}$(trailing) $< \lambda_1^{(s)}$(leading). Region B also defines the range of values of (α, β) in which the first eigenvalue of the *adhered* characteristic equation (5.9) is complex, so for these material combinations, stick at the contact edge is impossible for any coefficient of friction. If the applied loads are insufficient to support gross slip, we then anticipate either a region of edge slip or a region of separation, depending on the sign of $K_1^{(s)}$. A special case is that where body 2 is rigid, giving $\alpha = 1, \beta = (1 - 2\nu_1)/2(1 - \nu_2)$, which defines the right edge of the parallelograms in Fig. 5-2.

The problem of normal indentation of an elastic half-plane by a rigid flat punch was solved by Spence [88], who demonstrated the existence of edge slip zones whose extent depends on both f and β. It is interesting to note that Spence's solution implies that finite [albeit small] slip zones are predicted for arbitrarily large coefficients of friction.

5.2.3.1 Determination of the critical friction coefficients

In section 5.2.1, we discussed the nature of the eigenvalues for different coefficients of friction. Here, we determine the critical coefficients of friction for which the nature of the eigenvalues changes.

The critical friction coefficients can be obtained from the characteristic equations (5.8, 5.9). For example, f_b is the value at which the first eigenvalue of (5.8) reaches unity. Since $\lambda = 1$ satisfies this equation for all values of the parameters, we have to apply L'Hôpital's rule, from which we obtain

$$f_b = \frac{1}{\pi}\left(\frac{1+\alpha}{1-\alpha}\right), \tag{5.11}$$

which we note is independent of β.

The coefficient f_c is the value of f at which the first root of (5.8) becomes complex, or equivalently at which the first two real roots coincide. It was determined numerically and a contour plot inside the Dundurs' parallelogram is shown in Fig. 5-5(a).

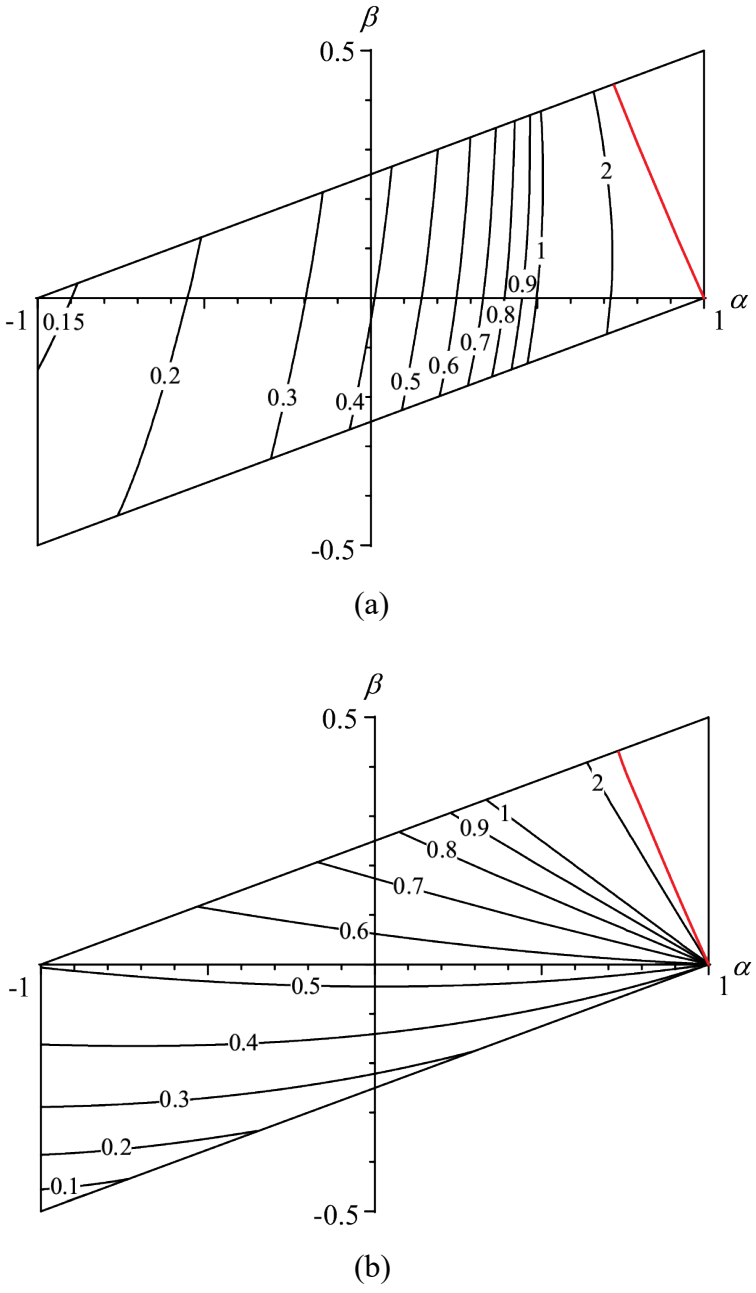

Figure 5-5: Contour plots of the critical friction coefficients: (a)f_c, (b)f_a.

The coefficient f_a can be determined as the ratio of the [adhered] eigenfunctions $f_{\theta r}^{1(a)}(0)$, $f_{\theta\theta}^{1(a)}(0)$ in equation (5.2). Kim *et al.* [85] used this method to make a contour plot of f_a in the Dundurs parallelogram. This requires calculation of the eigenfunctions and hence entails

significant additional algebraic manipulations. However, the case $f = f_a$ essentially represents a pivot between the stick and slip asymptotics, so for this friction coefficient the same functions satisfy both equations (5.9) and (5.8). A simpler calculation method is therefore to determine the first eigenvalue from (5.9), substitute it into the slip characteristic equation (5.8) and then use the resulting equation to solve for f_a. Figure 5-5(b) shows a contour plot for the magnitude of f_a. We note that both the magnitude of f_a and f_c increase without limit as we approach the boundary between regions *A* and *B*.

5.2.4 Non-monotonic loading

Frictional contact problems are inherently history-dependent in that the current state of a system can depend on the previous loading scenario. The 'memory' of the system resides in the slip displacements locked in any region which transitions from slip or separation to stick [89]. In particular, the detailed history of loading affects the instantaneous state of the system when a slip zone 'advances' into a stick zone [90].

5.2.4.1 Region A

Suppose that two contacting bodies with material properties corresponding to region *A* are loaded in such a way that the adhered stress-intensity factors $K_1^{(a)}$, $K_2^{(a)} < 0$ and $\left|K_1^{(a)}\right|$ increases monotonically. For $f < f_a$, as explained in Section 5.2.3, we anticipate a slip zone near the corner whose size scales with d_0 from equation (5.4), and for this zone to be non-decreasing we therefore also require that $K_1^{(a)}/K_2^{(a)}$ be non-decreasing. Under these conditions, the embedded field very close to the corner will be described by the leading-edge slip asymptotic and the corresponding local normal and tangential tractions can be expressed as equation (5.5) with the positive sign.

Suppose now that $K_1^{(a)}$ reaches a maximum negative value and then increases by $\Delta K_1^{(a)}$. In many frictional problems, if the tangential loading rate changes sign, the entire interface sticks instantaneously at the maximum load, after which reversed slip zones of growing magnitude are developed. We therefore start with the provisional assumption that the entire contact interface will stick instantaneously in which case the previous tractions would be modified by the adhered asymptotic to

$$p(r) \approx -K_1^{(s)} r^{\lambda_1^{(s)}-1} - \Delta K_1^{(a)} r^{\lambda_1^{(a)}-1} f_{\theta\theta}^{1(a)}(0);$$

$$q(r) \approx f K_1^{(s)} r^{\lambda_1^{(s)}-1} + \Delta K_1^{(a)} r^{\lambda_1^{(a)}-1} f_{\theta r}^{1(a)}(0), \tag{5.12}$$

where the first term defines the first term in the slip asymptotic series when $K_1^{(a)}$ reaches its maximum negative value. Since $\lambda_1^{(s)} > \lambda_1^{(a)}$, the contact edge behaviour is dominated by the $\Delta K_1^{(a)}$ term and therefore the edge separates [$\Delta K_1^{(a)} > 0$] with an adjacent 'trailing-edge' slip zone [82]. The sizes of these zones will vary continuously with $\Delta K_1^{(a)}$ and by analogy with (5.4) should scale with

$$d_1 = \left(\frac{\Delta K_1^{(a)}}{K_1^{(s)}} \right)^{\frac{1}{\lambda_1^{(s)} - \lambda_1^{(a)}}} \tag{5.13}$$

We next consider the case where $K_1^{(a)}$ is negative and decreases monotonically, but $K_1^{(a)}/K_2^{(a)}$ reaches a maximum and then decreases. Equation (5.4) would then imply a decrease in d_0 and hence in the extent of the slip zone, but this defines a state of advancing stick, where we expect the solution to depend on the precise relation between $K_1^{(a)}$ and $K_2^{(a)}$ during this phase of the loading. Problems of this kind can only be solved using an incremental formulation.

5.2.4.2 Region B

For material combinations in region B, the first eigenvalue $\lambda_1^{(a)}$ and stress-intensity factor $K_1^{(a)}$ are complex, implying oscillatory fields at the corner, which violate both the frictional and Signorini inequalities. We anticipate a small region of leading-edge slip adjacent to the corner, embedded in the surrounding oscillatory asymptotic field. The extent of this region will remain constant if $\left|K_1^{(a)}\right|$ increases monotonically and $\arg\{K_1^{(a)}\}$ remains constant. The extent of the slip zone is a monotonic function of $\arg\{K_1^{(a)}\}$ and hence this solution also remains valid if $\arg\{K_1^{(a)}\}$ increases monotonically. As in Section 5.2.4.1, the tractions very close to the corner can then be characterized by the first term in the slip asymptotic.

If $\arg\{K_1^{(a)}\}$ is constant and $\left|K_1^{(a)}\right|$ increases monotonically to a maximum and then decreases, we again assume instantaneous stick, leading to tractions of the form (5.12), except that the contribution from $\Delta K_1^{(a)}$ is now oscillatory. However, $\Re\{\lambda_1^{(a)}\} < \lambda_1^{(s)}$(leading) for all $f > 0$ [they are equal for $f = 0$] so the change in the field is dominated by $\Delta K_1^{(a)}$ and we therefore anticipate a region of separation at the corner and an adjacent region of trailing-edge slip.

Turner [91] considered the problem where an axisymmetric rigid flat punch is pressed into an elastic half space by a normal force which is first increased to a maximum value and then decreased. During the monotonic loading phase, Spence [88] determined the [constant] size of the leading-edge slip zone as a function of f and β. During unloading, Turner found that leading-edge slip penetrated further away from the edge, but was surrounded by an annulus of stick until the normal load had been reduced to about half its maximum value, after which a further annulus of trailing-edge slip is developed. This conclusion violates the present asymptotic arguments, since we now know that stick at the corner is impossible under any loading conditions. We must

conclude that Turner's numerical solution was insufficiently refined to detect the inevitable small regions of slip and separation once unloading commences.

5.3 Conclusion

In this chapter, we have investigated the influence of material dissimilarity on the corner traction fields for contact between an elastic right-angle wedge and an elastic half-plane. The material parameters define a point in the Dundurs parallelogram of Fig. 5-4 and qualitatively distinct behaviour is predicted depending on whether this point lies in region *A* or region *B* of this figure.

For material combinations in region *A*, the behaviour is qualitatively similar to that for the case where the materials are the same, but the critical friction coefficients identified by Karuppanan *et al.* [83] and Churchman and Hills [82] are changed. Contour plots of these coefficients are presented in Fig. 5-5.

For material combinations in region *B*, the behaviour is qualitatively similar to that for the case where the wedge is rigid and the half-plane is elastic. If an initial period of monotonic loading is followed by a load reversal, the initial behaviour can be predicted based on the relative strengths of the singularities associated with the locked-in shear tractions and the incremental stick asymptotic.

The results give insight into the high local stresses at the edge of a contact between elastically dissimilar bodies, such as those involved in PCI failure [5]. They can also be used to evaluate corresponding finite element models, in particular to determine whether the mesh is sufficiently refined near the corner to recover the appropriate analytically predicted asymptotic behaviour.

Chapter 5 is reproduced from the publication:

K. Hong, M. D. Thouless, W. Lu and J. R. Barber, “Asymptotic stress fields for complete contact between dissimilar materials”, Journal of Applied Mechanics, 86(1), 011009, 2019

Chapter 6 Corner Stress Fields in Sliding at High Friction Coefficients

6.1 Introduction

If an elastic body with a sharp corner is pressed against an elastic half-plane as shown in Fig. 6-1, the stress field near the corner can be expanded as an asymptotic series of the form

$$\sigma_{ij}(r,\theta) = \sum_{n=1}^{\infty} K_n r^{\lambda_n - 1} f_{ij}^n(\theta) \tag{6.1}$$

[81], [92], where λ_n and $f_{ij}^n(\theta)$ are eigenvalues and eigenfunctions respectively, (r,θ) are polar coordinates centered on the corner, and K_n are a set of coefficients depending on the far-field loading. The eigenvalues are generally arranged in order of ascending real part, so the local stress field close to the corner is dominated by the first term of equation (6.1). In particular, if the field is singular, the strength of the singularity is determined by λ_1 and K_1 plays the rôle of a generalized stress-intensity factor.

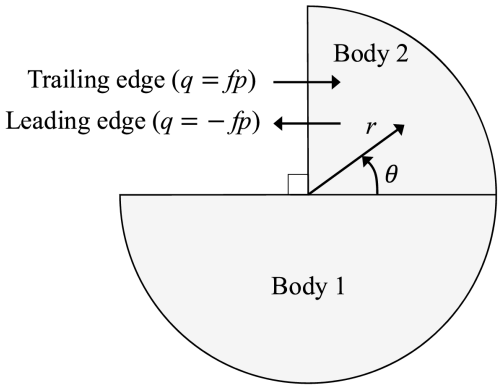

Figure 6-1: A quarter-plane indenting a half-plane. At a trailing edge [body 2 slipping relatively to the right], $q = fp$ and at a leading edge [body 2 slipping relatively to the left], $q = -fp$.

If the upper body (6.2) in Fig. 6-1 slides over the lower body (6.1), and if Amontons' friction law is assumed, the local contact pressure $p(r)$ and the shear traction $q(r)$ must satisfy the condition $q = \pm fp$, where the sign depends on the direction of sliding. Here, the sign is positive when body 2 slides to the right [trailing-edge slip] and negative when it slides to the left [leading-edge slip]. It is then convenient to normalize the first term of equation (6.1) in the form

$$p(r) \approx -K_1 r^{\lambda_1 - 1};$$

$$q(r) \approx \pm f K_1 r^{\lambda_1 - 1}, \tag{6.2}$$

Karuppanan *et al.* [83] studied the case where body 2 has a right-angle corner and the two bodies are of similar materials. The first two eigenvalues are shown as a function of f in Fig. 6-2. These comprise a complex-conjugate pair for trailing-edge slip with $f > f_c$, but these bifurcate into two distinct real eigenvalues for $f < f_c$, including negative values corresponding to leading-edge slip.

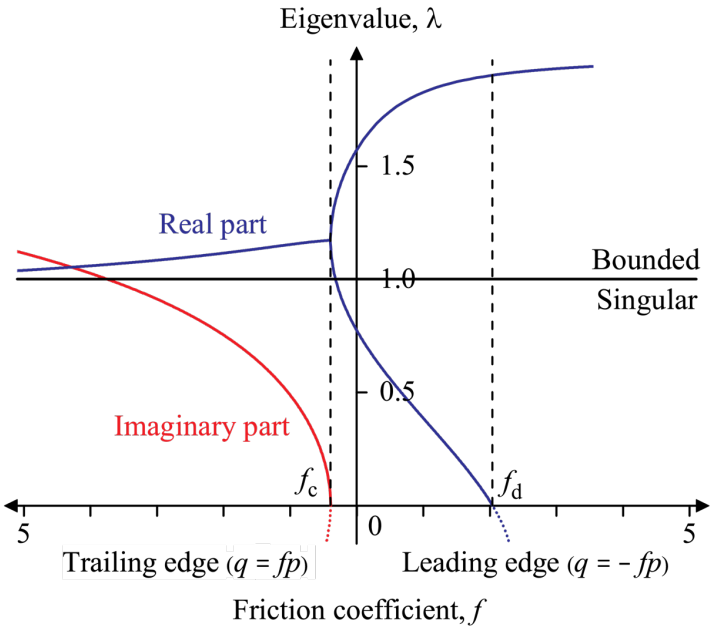

Figure 6-2: Slip eigenvalues as a function of friction coefficient for the contact between elastically similar materials.

Notice, in particular, that in leading-edge slip, the lowest eigenvalue decreases with increasing f and goes to zero at $f = f_d = 2.04$. Energetic considerations restrict the eigenvalues to the range $\Re(\lambda_n) > 0$ for all n, so conventional wisdom would say that for $f > f_d$, the corner field would be determined by the first positive eigenvalue, implying bounded stresses at the corner. However, this implies a discontinuous change in leading- edge behaviour over an infinitesimal change of friction coefficient near $f = f_d$, which seems counter-intuitive. This is the question which we explore in the present chapter.

Of course, coefficients of friction in this range are rare, so the question might be deemed rather academic, but we would like to know the answer in the interests of mathematical completeness. Also, we shall show that with dissimilar materials the same effect can occur with coefficients as low as 1.57, and there do exist material combinations where such values are obtainable. For example, the coefficient of friction between a UO_2 fuel pellet and Zircaloy cladding under irradiation can be as large as 3 depending on the operating condition [93], [94]. Also, rubbers in contact with other materials, such as glass or silicon carbide, can yield coefficients larger than 2 [95].

6.2 A finite-element model

To explore this question in more detail, we developed a finite-element model of the system shown in Fig. 6-3, in which a rectangular strip is pressed against a body with a plane surface by a uniform pressure p applied to the upper surface. This surface was also subjected to a small uniform leftward displacement d sufficient to ensure slip at all contact nodes, since the alternative imposition of shear traction boundary conditions would leave a rigid-body degree of freedom. Hard contact boundary conditions were used at the interface with the direct method to ensure no interpenetration, and a classical Coulomb model was implemented for the tangential behavior,

using the augmented-Lagrangian method. Initially, following Karuppanan *et al.* [83], we used similar elastic properties for the two bodies, but later we shall report results for the more general case.

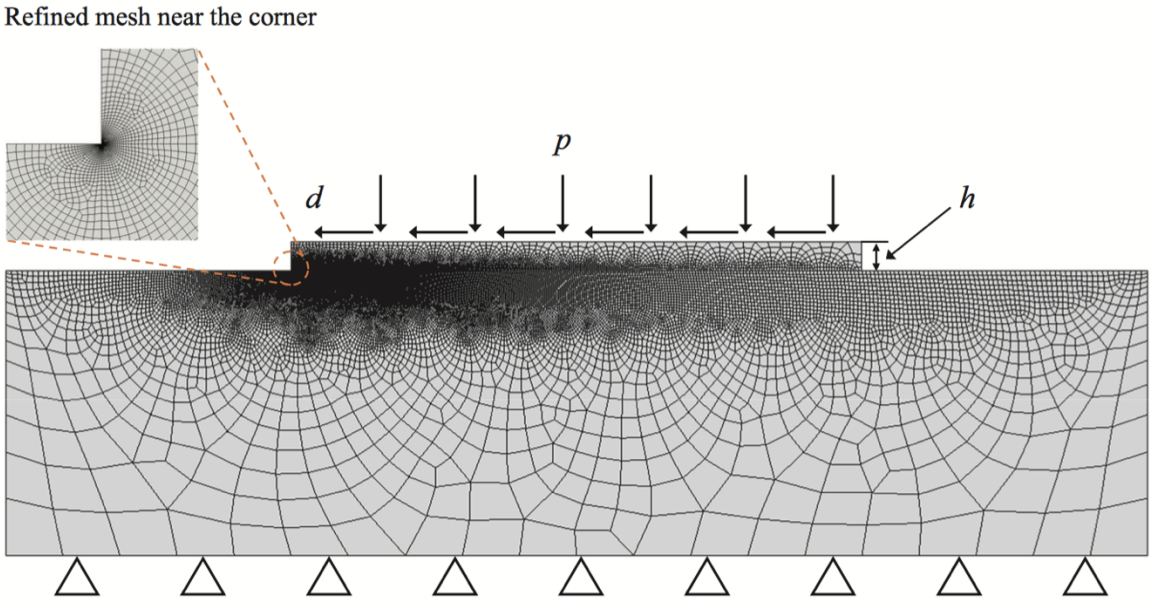

Figure 6-3: Plane-strain finite-element model to evaluate the asymptotic behaviour at the leading edge (left-hand corner).

Since we are interested specifically in the leading-edge behaviour, we refined the mesh near the left-hand corner. The adequacy of this mesh refinement was tested by comparing the strength of the stress singularity $[\lambda_1 - 1]$ from the asymptotic analysis with the slope of a log-log plot of the finite-element stresses along the interface for $f < f_d$. Good agreement was obtained when the ratio of the smallest elements to the height of body 2 [the smallest linear dimension of the object] was set to be 0.001.

6.2.1 Results for $f \leq f_d$

The finite-element results show that there exists a critical friction coefficient f_e such that for $f_e < f < f_d$, an interior separation region $a < r < b$ develops adjacent to the slip region at the corner, as shown in Fig. 6-4. For similar materials $f_e = 1.66$ and $f_d = 2.04$. For a given value of

f in this range, the dimensions a, b scale with the height h of the upper body, showing that these features are determined by the macroscopic dimensions and loading of the system.

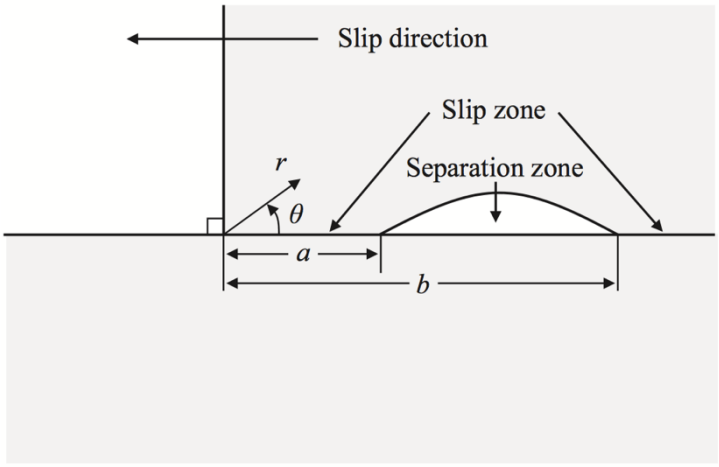

Figure 6-4: Slip and separation zones developed at the leading edge for $f_e < f < f_d$.

As $f \to f_d$, $a \to 0$, whereas b tends to a non-zero constant depending on the macroscopic conditions. Thus, in the limit $f = f_d$ we essentially have a point contact at the corner. This is of course consistent with an eigenvalue of zero, since the stress field is then proportional to r^{-1} as in the classical Flamant solution.

To ensure that this point contact is not an artifact of the necessarily finite mesh size, a technique was developed which enables us to obtain results for a highly refined mesh, which in the original model would lead to a very large ratio between the dimensions of the largest and smallest elements. The procedure is as follows:-

1. Run the simulation with the original model as in Fig. 6-5 (right).

2. Consider a small circular region centered on the corner and capture the stress or displacement field [σ or u] along the circular boundary.

3. Build a new model comprising only the circular region, and apply the obtained field along the boundary as in Fig. 6-5 (left).

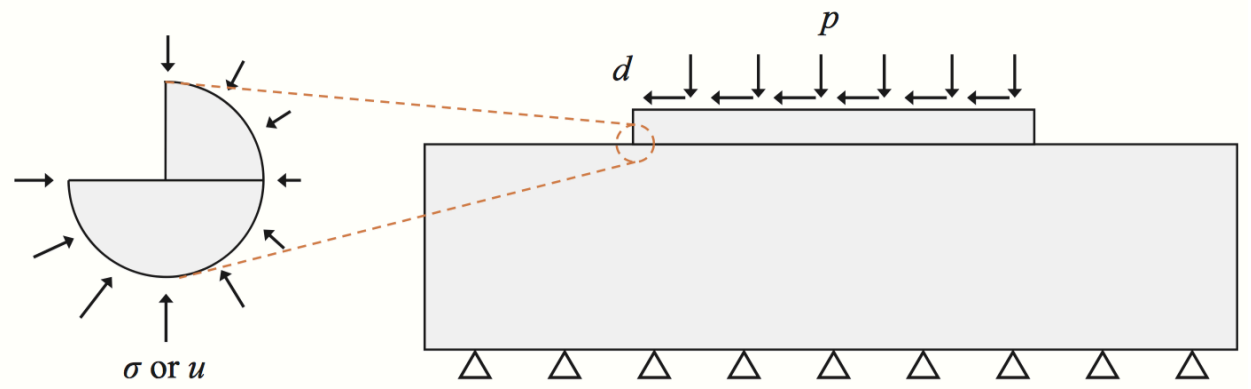

Figure 6-5: Schematic of a finite-element simulation technique to implement a highly refined mesh near the corner of interest.

This procedure can be repeated if necessary to achieve any desired level of mesh refinement in the corner. In the present case, we used it to obtain results for a corner element dimension of $10^{-10}h$, for which we still obtained only a single node in contact at $f = f_d$. Also, with each level of refinement, the tractions and displacements on the circular boundary approached more closely to the sinusoidal asymptotic form, and the concentrated force on the corner node was insensitive to mesh refinement beyond that used in the original model.

6.2.2 Results for $f > f_d$

We next conducted simulations to investigate the leading-edge behaviour for $f > f_d$, for which a conventional asymptotic argument based on Fig. 6-2 would predict bounded stresses in the corner. Instead, we once again obtained single-node [point] contact at the corner with an adjacent separation zone. Also, the magnitude of this force and the size of the separation zone increase with increasing f, for given macroscopic geometry and loading conditions.

This raises the question "Why does the system not follow the asymptotic form suggested by Fig. 6-2 for $f > f_d$?" To answer this, we must remember that the first term in an asymptotic

series is a good approximation to the actual field only at values of r that are small compared with the other dimensions in the contact geometry. In other words, there must exist a 'K_1-dominated region'. Now Fig. 6-2 is based on the assumption that we have contact with slip adjacent to the corner, so a K_1-dominated region [$r \ll a$] can be found for the configuration of Fig. 6-4 if and only if the extent of the leading slip zone $a > 0$. If we have point contact at the corner [$a = 0$], no such region exists. It is of course possible to develop an alternative asymptotic solution for the case where a slipping point contact at the corner abuts a separation zone, but unsurprisingly this would yield stresses varying with r^{-1}, corresponding to $\lambda_1 = 0$.

6.2.3 A hyperelastic solution

Point contacts and the associated asymptotic fields are strictly inadmissible in linear elasticity, since the strain energy in a small circular region surrounding the singular point is then logarithmically unbounded. Also, the displacement field is logarithmically unbounded in the corner, which is reflected in the finite-element solution by corner displacements that continue to increase as the mesh is refined, even though the stress field converges.

Clearly the assumptions of linear elasticity will break down sufficiently near the corner [this is true even for admissible singularities] due to non-linearities in the kinematics and possibly also in the constitutive law, and it is natural to expect these effects to distribute the concentrated force over a finite contact region. Since the mathematical objection to the linear elastic solution is associated with unbounded strain energy, we chose to explore the non-linear solution using a hyperelastic model, since in this context, energy is still conserved. For a hyperelastic material, the strain energy density is defined as a function of the invariants of the deformation tensor. In this analysis, we used the Generalized Neo-Hookean model [96] which incorporates a range of 'hardening' characteristics, represented by an exponent n [$> 1/2$], in the Neo-Hookean model [for

which $n = 1$]. The effect of n is to change the rate of strain hardening in response to uniaxial tension [97].

Surprisingly [at least to the present authors], the non-linear results continue to show contact at a single node at the corner. Also, the contact force remains essentially constant with mesh refinement, with a value that is only slightly [less than 1%] lower than that of the linear solution. This implies, incidentally, that a good approximation to the nonlinear solution could be obtained by using the two-stage procedure of Fig. 6-5, where the simpler linear solution is used for the first [coarse mesh] step. More generally, the nonlinear solution of Fig. 6-5 (left) could be patched into the corner field of any linear contact problem exhibiting a concentrated corner force.

6.2.3.1 Energetic considerations

Equilibrium arguments show that the components of the Cauchy stress due to a concentrated force must still vary with r^{-1}, but in contrast to linear elasticity, this singularity is physically admissible in the framework of nonlinear elasticity and indeed has been reported in hyperelastic problems involving cracks [98], [99]. If the local stress components vary with r^{-1}, the corresponding displacements have the form $r^{1-1/(2n)}$, and are therefore bounded as $r \to 0$. The strain energy density then involves an r^{-1} singularity, and hence the total strain energy in a small circle surrounding the singular point is also bounded.

6.3 Dissimilar materials

If the materials of the two bodies are different, the eigenvalues λ_n of equation (6.1) during sliding satisfy the equation

$$(1+\alpha)\cos(\lambda\pi)\left[\sin^2\left(\frac{\lambda\pi}{2}\right)-\lambda^2\right]+\frac{1-\alpha}{2}\sin^2(\lambda\pi)$$

$$\pm f sin(\lambda\pi)\left\{(1-\alpha)\lambda(1+\lambda)-2\beta\left[\sin^2\left(\frac{\lambda\pi}{2}\right)-\lambda^2\right]\right\}=0, \tag{6.3}$$

[86], [87], where α, β are Dundurs' bimaterial parameters [66], and as before we take the negative sign for leading-edge slip. Equation (6.3) has a trivial root $\lambda = 0$ for all α, β, f, so to determine the critical coefficient of friction f_d, we use L'Hôpital's rule to determine the condition for there to be a second non-trivial root. We obtain

$$f_d = \frac{\pi}{2} - \frac{\pi^2-4}{4\pi}\left(\frac{\alpha+1}{\alpha-1}\right) = \frac{\pi}{2} + \frac{\pi^2-4}{4\pi}\left(\frac{1-\nu_1}{1-\nu_2}\right)\frac{G_2}{G_1}, \tag{6.4}$$

where G_i, ν_i are respectively the shear modulus and Poisson's ratio for body i. The minimum value is $f_d = 1.57$, which occurs when $\alpha = -1$, or $G_2/G_1 \to 0$ — i.e. when the half-plane has a much larger elastic modulus than the body with the corner.

6.4 Conclusions

We have shown that if an elastic body with a right-angle corner slides over an elastic half-plane, there exists a critical coefficient of friction f_d above which a concentrated point contact occurs at the leading edge, with an adjacent separation region. This appears to contradict the asymptotic analysis of Karuppanan *et al.* [83] which predicts a bounded asymptotic field for $f > f_d$, but this result depends on the existence of a K_1-dominated slip region which does not exist if contact occurs only at a point.

In linear elasticity, the corresponding $1/r$ singularity implies infinite strain energy in a finite corner region and hence is strictly inadmissible. However, we show that a hyperelastic solution of the problem resolves this issue and also predicts a concentrated corner force whose magnitude is almost identical to that in the linear solution.

Chapter 6 is reproduced from the publication:

K. Hong, W. Lu, M. D. Thouless and J. R. Barber, “Corner stress fields in sliding at high friction coefficients”, European Journal of Mechanics / A Solids, 76, 308-311, 2019

Chapter 7 Conclusions and Outlook

In this dissertation, various generic problems occurring in pressurized-water reactors (PWRs) associated with the possible failure of the cladding have been studied: (i) the cracking and spalling of oxide layer developed at the outer surface of the cladding during normal operation, (ii) the cracking within the coating layer of Cr-coated Zircaloy cladding (ATF cladding), (iii) the pellet-cladding interaction (PCI) considering various power histories, (iv) the fundamental contact mechanics related to the PCI problem.

The oxide layer formed during normal operation exhibits a tensile hoop stress at the outer surface after reaching a critical thickness. The tensile stress results in possible cracking within oxide layer, which could be classified into three cases depending on the thickness and toughness of the oxide: (i) radial cracking without channeling, (ii) channel cracking within the oxide, and (iii) channel crack through the entire oxide and possibly penetrating into the metal. Fracture-mechanics analysis indicated that the spalling will leave a thin layer of oxide adhered to the metal, which were occasionally observed experimentally.

A uniform tensile hoop stress is developed in the coating layer of Cr-coated Zircaloy cladding, where its magnitude depends on the operating conditions. The maximum hoop stress increases with the ramped power and reaches a plateau. The crack channeling analysis showed that the steady-state energy-release rate increases almost linearly with the thickness of the coating layer. Critical coating thickness, above which cracking would occur, was obtained as a function of ramped power, which should be considered for the design of Cr-coated Zircaloy cladding. A design

protocol was also proposed which allows fracture analysis of the coating to be simply done using existing PCI codes.

Power history significantly affects possible PCI failure due to the multiple mechanisms with different time-scales that are involved in the PCI problem. It was found that the local stresses in the vicinity of the crack can be tensile or compressive depending on when contact is established between the cladding and pellet. If PCI is initiated either before power ramping or during the transient period of a power ramps, the local hoop stress becomes tensile, which may lead to PCI failure (by either brittle failure during the transient power ramp or failure during the steady-state power ramp). On the other hand, if PCI occurs during the normal operation or steady state portions of a power ramp, the local hoop stress becomes compressive which suppresses the possible PCI failure.

Being closely related to the PCI problem, asymptotic stress field near the corner of contact between an elastic right-angle wedge and an elastic half-plane was studied. First, the effect of material dissimilarity on the corner traction fields was investigated, where the Dundurs parallelogram could be divided into region A and B as in Fig. 5-4 depending on the distinct contact edge behavior. The behaviour of region A is qualitatively similar to that for the case where the materials are the same, while the critical friction coefficients, f_a, f_b, and f_c, which characterize the behavior change depending on material combinations. The behaviour of region B is qualitatively similar to that for the case where the wedge is rigid and the half-plane is elastic. I also found that there exists a critical coefficient of friction f_d above which a concentrated point contact occurs at the leading edge, with an adjacent separation region. In linear elasticity, the corresponding $1/r$ singularity indicates that the strain energy in a finite corner region is infinite, which is not physically admissible.

The work presented in this dissertation provides guidelines in the design of fuel rods in PWRs in many different aspects. For the analyses, High-fidelity computational codes and models were developed, which are applicable to analyze reactor designs, including analysis of issues related to structural mechanics and safety. In addition, computational constitutive models of new fuels, such as Cr-coated Zircaloy cladding (ATF cladding) were developed, applicable to evaluate their safety under severe conditions. These researches could be used to improve the understanding of physical phenomena related to the failure of fuel rods, allowing the safety of the reactor system to be enhanced.

In future, the above analyses on PCI failure can be reproduced by considering design-basis accident (DBA), including loss-of-coolant accident (LOCA) or reactivity-initiated accident (RIA), to ensure the safety of the reactor system under the severe loading conditions. The models on the cracking in the coating layer and oxide layer can be further developed by introducing the concept of periodic cracking. It will enhance the understanding on the multiple channel cracks observed on the surfaces of the above layers. Besides, I can explore the effect of oxide or coating layer on other mechanical problems in PWRs, for example, the grid-to-rod fretting (GTRF) wear which may lead to the fuel leakage.

Bibliography

[1] K. Une and S. Ishimoto, "Dissolution and precipitation behavior of hydrides in Zircaloy-2 and high Fe Zircaloy," *J. Nucl. Mater.*, vol. 322, no. 1, pp. 66–72, 2003.

[2] A. M. Garde, G. P. Smith, and R. C. Pirek, "Effects of hydride precipitate localization and neutron fluence on the ductility of irradiated Zircaloy-4," *Zircon. Nucl. Ind. Elev. Int. Symp. ASTM Int.*, 1996.

[3] J. C. Thornley and A. S. Wronski, "The grain size dependences of the failure mode and ductility transition temperatures of melted chromium and tungsten," *Met. Sci. J.*, vol. 6, pp. 113–118, 1972.

[4] S. Arsene, J. Bai, and P. Bompard, "Hydride embrittlement and irradiation effects on the hoop mechanical properties of pressurized water reactor (PWR) and boiling-water reactor (BWR) Zircaloy cladding tubes: Part III. Mechanical behavior of hydride in stress-relieved annealed and recrystall," *Metall. Mater. Trans. A*, vol. 34, no. 3, pp. 579–588, 2003.

[5] B. Cox, "Pellet-clad interaction (PCI) failures of zirconium alloy fuel cladding – a review," *J. Nucl. Mater.*, vol. 172, no. 3, pp. 249–292, 1990.

[6] V. Georgenthum, J. Desquines, and V. Bessiron, "Influence of outer zirconia transient cracking and spalling on thermomechanical behaviour of high burnup fuel rod submitted to RIA," *J. Nucl. Sci. Technol.*, vol. 43, no. 9, pp. 1089–1096, 2006.

[7] K. Hong, J. R. Barber, M. D. Thouless, and W. Lu, "Cracking and spalling of the oxide layer developed in high-burnup Zircaloy-4 cladding under normal operating conditions in a PWR," *J. Nucl. Mater.*, vol. 512, pp. 46–55, 2018.

[8] K. A. Terrani, "Accident tolerant fuel cladding development: Promise, status, and challenges," *J. Nucl. Mater.*, vol. 501, pp. 13–30, 2018.

[9] H. Kim, I. Kim, J. Park, and Y. Koo, "Application of coating technology on zirconium-based alloy to decrease high-temperature oxidation," *Zircon. Nucl. Ind. 17th Vol. ASTM Int.*, pp. 346–369, 2015.

[10] H. Kim, I. Kim, Y. Jung, D. Park, J. Park, and Y. Koo, "Adhesion property and high-temperature oxidation behavior of Cr- coated Zircaloy-4 cladding tube prepared by 3D laser coating," *J. Nucl. Mater.*, vol. 465, pp. 531–539, 2015.

[11] S. J. Zinkle and L. L. Snead, "Designing radiation resistance in materials for fusion energy," *Annu. Rev. Mater. Res.*, vol. 44, pp. 241–267, 2014.

[12] C. Tang, M. Stueber, H. J. Seifert, and M. Steinbrueck, "Protective coatings on zirconium-based alloys as accident-tolerant fuel (ATF) claddings," *Corros. Rev.*, vol. 35, no. 3, pp. 141–165, 2017.

[13] J. Bischoff, C. Delafoy, C. Vauglin, P. Barberis, D. Perche, D. Duthoo, F. Schuster, J. C. Brachet, E. W. Schweitzer, and K. Nimishakavi, "AREVA NP's enhanced accident-tolerant fuel developments: Focus on Crcoated M5 cladding," *Nucl. Eng. Technol.*, vol. 50, no. 2,

pp. 223–228, 2018.
[14] A. Wu, J. Ribis, J. C. Brachet, E. Clouet, F. Leprłtre, E. Bordas, and B. Arnal, “HRTEM and chemical study of an ion-irradiated chromium/Zircaloy-4 interface,” *J. Nucl. Mater.*, vol. 504, pp. 289–299, 2018.
[15] M. Oguma, “Cracking and relocation behavior of nuclear fuel pellets during rise to power,” *Nucl. Eng. Des.*, vol. 76, no. 1, pp. 35–45, 1983.
[16] W. J. Penn, R. K. Lo, and J. C. Wood, “CANDU fuel – power ramp performance criteria,” *Nucl. Technol.*, vol. 34, no. 2, pp. 249–268, 1977.
[17] H. M. Chung and T. F. Kassner, “Cladding metallurgy and fracture behavior during reactivity-initiated accidents at high burnup,” *Nucl. Eng. Des.*, vol. 186.3, no. December, pp. 411–427, 1998.
[18] F. Schmitz and J. Papin, “High burnup effects on fuel behaviour under accident conditions: the tests CABRI REP-Na,” *J. Nucl. Mater.*, vol. 270, no. 1, pp. 55–64, 1999.
[19] J. Papin, B. Cazalis, J. M. Frizonnet, J. Desquines, F. Lemoine, V. Georgenthum, F. Lamare, and M. Petit, “Summary and interpretation of the CABRI REP-Na program,” *Nucl. Technol.*, vol. 157, no. 3, pp. 230–250, 2007.
[20] N. J. Petch, “The cleavage strength of polycrystals,” *J. Iron Steel Inst.*, vol. 174, pp. 25–28, 1953.
[21] J. Desquines, V. Georgenthum, F. Lemoine, and B. Cazalis, “The fracture and spallation of zirconia layers in high burnup PWR fuel claddings submitted to RIA transients,” *18th Int. Conf. Struct. Mech. React. Technol. C*, vol. 3, pp. 444–453, 2005.
[22] A. B. Johnson, E. R. Gilbert, and R. J. Guenther, “Behavior of spent nuclear fuel and storage system components in dry interim storage,” *PNL-4189, Prep. U. S. Dep. Energy under Contract DE-AC06-76RLO 1830, Pacific Northwest Lab.*, 1982.
[23] D. Rozzia, M. Adorni, A. Del Nevo, and F. D. Auria, “Capabilities of TRANSURANUS code in simulating power ramp tests from the IFPE database,” *Nucl. Eng. Des.*, vol. 241, no. 4, pp. 1078–1086, 2011.
[24] N. Baba, “Aspects of electrochemistry, chemistry, physics, and applications of ‘Less-Common Metals,’” *J. Less Common Met.*, vol. 43, pp. 295–301, 1975.
[25] Y. Kim, Y. Jeong, and J. Jang, “Stress measurements during thin film zirconium oxide growth,” *J. Nucl. Mater.*, vol. 412, no. 2, pp. 217–220, 2011.
[26] C. Roy and G. David, “X-ray diffraction analyses of zirconia films on zirconium and Zircaloy-2,” *J. Nucl. Mater.*, vol. 37, no. 1, pp. 71–81, 1970.
[27] P. Platt, E. Polatidis, P. Frankel, M. Klaus, M. Gass, R. Howells, and M. Preuss, “A study into stress relaxation in oxides formed on zirconium alloys,” *J. Nucl. Mater.*, vol. 456, pp. 415–425, 2015.
[28] J. Godlewski, P. Bouvier, G. Lucazeau, and L. Fayette, “Stress distribution measured by Raman spectroscopy in zirconia films formed by oxidation of Zr-based alloys,” *Zircon. Nucl. Ind. Twelfth Int. Symp. ASTM Int.*, pp. 877–900, 2000.
[29] A. T. Motta, A. Couet, and R. J. Comstock, “Corrosion of zirconium alloys used for nuclear fuel cladding,” *Annu. Rev. Mater. Res.*, vol. 45, no. 1, pp. 311–343, 2015.
[30] E. Hillner, “Corrosion of zirconium-base alloys—an overview,” *ASTM Int.*, 1977.
[31] E. Hillner, D. G. Franklin, and J. D. Smee, “Long-term corrosion of Zircaloy before and

after irradiation," *J. Nucl. Mater.*, vol. 278, no. 2, pp. 334–345, 2000.
[32] H. Wang, Z. Hu, W. Lu, and M. D. Thouless, "A mechanism-based framework for the numerical analysis of creep in Zircaloy-4," *J. Nucl. Mater.*, vol. 433, pp. 188–198, 2013.
[33] H. J. Frost and M. F. Ashby, *Deformation mechanism maps: the plasticity and creep of metals and ceramics*. 1982.
[34] M. J. Roddy, W. R. Cannon, G. Skandan, and H. Hahn, "Creep behavior of nanocrystalline monoclinic ZrO2," *J. Eur. Ceram. Soc.*, vol. 22, no. 14, pp. 2657–2662, 2002.
[35] A. H. Chokshi, "Diffusion, diffusion creep and grain growth characteristics of nanocrystalline and fine-grained monoclinic , tetragonal and cubic zirconia," *Scr. Mater.*, vol. 48, no. 6, pp. 791–796, 2003.
[36] D. M. Owen and A. H. Chokshi, "The high temperature mechanical characteristics of superplastic 3 mol% yttria stabilized zirconia," *Acta Mater.*, vol. 46, no. 2, pp. 667–679, 1998.
[37] L. J. Siefken, E. W. Coryell, E. A. Harvego, and J. K. Hohorst, "SCDAP/RELAP5/MOD 3.3 Code Manual: MATPRO—A Library of Materials Properties for Light-Water-Reactor Accident Analysis," *Idaho Natl. Eng. Environ. Lab.*, 2001.
[38] M. S. Hu, M. D. Thouless, and A. G. Evans, "The decohesion of thin films from brittle substrates," *Acta Metall.*, vol. 36, no. 5, pp. 1301–1307, 1988.
[39] J. Beuth, "Cracking of thin bonded films in residual tension," *Int. J. Solids Struct.*, vol. 29, no. 13, pp. 1657–1675, 1992.
[40] A. Bravo-Leon, Y. Morikawa, M. Kawahara, and M. J. Mayo, "Fracture toughness of nanocrystalline tetragonal zirconia with low yttria content," *Acta Mater.*, vol. 50, no. 18, pp. 4555–4562, 2002.
[41] J. Kondoh, H. Shiota, K. Kawachi, and T. Nakatani, "Yttria concentration dependence of tensile strength in yttria-stabilized zirconia," *J. Alloys Compd.*, vol. 365, no. 1–2, pp. 253–258, 2004.
[42] B. MUSSLER, M. V. Swain, and N. Claussen, "Dependence of fracture toughness of alumina on grain size and test technique," *J. Am. Cermaic Soc.*, vol. 65, no. 11, pp. 566–572, 1982.
[43] M. D. Thouless, "Cracking and delamination of coatings," *J. Vac. Sci. Technol. A Vacuum, Surfaces, Film.*, vol. 9, no. 4, pp. 2510–2515, 1991.
[44] M. D. Thouless, E. Olsson, and A. Gupta, "Cracking of brittle films on elastic substrates," *Acta Metall. Mater.*, vol. 40, no. 6, pp. 1287–1292, 1992.
[45] J. W. Hutchinson and Z. Suo, "Mixed mode cracking in layered materials," *Adv. Appl. Mech.*, vol. 29, pp. 63–191, 1991.
[46] V. B. Shenoy, A. F. Schwartzman, and L. B. Freund, "Crack patterns in brittle thin films," *Int. J. Fract.*, vol. 109, no. 1, pp. 29–45, 2001.
[47] M. D. Thouless, A. G. Evans, M. F. Ashby, and J. W. Hutchinson, "The edge cracking and spalling of brittle plates," *Acta Metall.*, vol. 35, no. 6, pp. 1333–1341, 1987.
[48] P. Bossis, D. Pecheur, L. Hanifi, J. Thomazet, and M. Blat, "Comparison of the high burn-up corrosion on M5 and low tin Zircaloy-4," vol. 3, no. 1, pp. 494–525, 2006.
[49] A. M. Garde, S. R. Pati, M. A. Krammen, G. P. Smith, and R. K. Endter, "Corrosion behaviour of Zircaloy-4 cladding with varying tin content in high temperature pressurised

water reactors," *Zircon. Nucl. Ind.*, vol. 10, no. ASTM STP 1245, pp. 760–778, 1994.
[50] G. . Sabol, R. J. Comstock, R. Weiner, P. Larouere, and R. . Stanutz, "In-reactor corrosion performance of ZIRLO and Zircaloy-4," *Zircon. Nucl. Ind. Tenth Int. Symp.*, pp. 724–744, 1994.
[51] A. M. Garde, G. Pan, A. J. Mueller, and L. Hallstadius, "Oxide surface peeling of advanced zirconium alloy cladding after high burnup irradiation in pressurized water reactors," *Zircon. Nucl. Ind. 17th Int. Symp.*, vol. ASTM STP 1, pp. 673–692, 2015.
[52] Y. Lee, J. I. Lee, and H. C. No, "Mechanical analysis of surface-coated Zircaloy cladding," *Nucl. Eng. Technol.*, vol. 49, no. 5, pp. 1031–1043, 2017.
[53] M. Wagih, B. Spencer, J. Hales, and K. Shirvan, "Fuel performance of chromium-coated zirconium alloy and silicon carbide accident tolerant fuel claddings," *Ann. Nucl. Energy*, vol. 120, pp. 304–318, 2018.
[54] B. Yang, K. Zhang, G. Chen, G. Luo, and J. Xiao, "Measurement of fracture toughness and interfacial shear strength of hard and brittle Cr coating on ductile steel substrate," *Surf. Eng.*, vol. 24, no. 5, pp. 332–336, 2008.
[55] J. C. Brachet, M. Le Saux, M. Le Flem, S. Urvoy, E. Rouesne, T. Guilbert, C. Cobac, F. Lahogue, J. Rousselot, M. Tupin, and P. Billaud, "On-going studies at CEA on chromium coated zirconium based nuclear fuel claddings for enhanced accident tolerant LWRs fuel," *TopFuel 2015, Zurich, Switz.*, pp. 31–38, 2015.
[56] J. D. Hales, R. L. Williamson, S. R. Novascone, G. Pastore, B. W. Spencer, D. S. Stafford, K. A. Gamble, D. M. Perez, and W. Liu., "BISON theory manual the equations behind nuclear fuel analysis," 2016.
[57] J. Park, H. Kim, J. Park, Y. Jung, D. Park, and Y. Koo, "High temperature steam-oxidation behavior of arc ion plated Cr coatings for accident tolerant fuel claddings," *Surf. Coat. Technol.*, vol. 280, pp. 256–259, 2015.
[58] D. J. Park, H. G. Kim, Y. Il Jung, J. H. Park, J. H. Yang, and Y. H. Koo, "Behavior of an improved Zr fuel cladding with oxidation resistant coating under loss-of-coolant accident conditions," *J. Nucl. Mater.*, vol. 482, pp. 75–82, 2016.
[59] U. Holzwarth and H. Stamm, "Mechanical and thermomechanical properties of commercially pure chromium and chromium alloys," *J. Nucl. Mater.*, vol. 300, pp. 161–177, 2002.
[60] E. O. Hall, "The deformation and ageing of mild steel: III discussion of results," *Proc. Phys. Soc. Sect. B*, vol. 64, no. 9, pp. 747–753, 1951.
[61] C. P. Brittain, R. W. Armstrong, and G. Smith, "Hall-Petch dependence for ultrafine grain size electrodeposited chromium," *Scr. Mater.*, vol. 19, no. 1, pp. 89–91, 1985.
[62] U. S. D. of Energy, *DOE Fundamentals Handbook: Material Science*, vol. 2, no. 72. 1993.
[63] M. Ševeček, A. Gurgen, A. Seshadri, Y. Che, M. Wagih, B. Phillips, V. Champagne, and K. Shirvan, "Development of Cr cold spray-coated fuel cladding with enhanced accident tolerance," *Nucl. Eng. Technol.*, vol. 50, no. 2, pp. 229–236, 2018.
[64] R. L. Williamson, J. D. Hales, S. R. Novascone, M. R. Tonks, D. R. Gaston, C. J. Permann, D. Andrs, and R. C. Martineau, "Multidimensional multiphysics simulation of nuclear fuel behavior," *J. Nucl. Mater.*, vol. 423, no. 1–3, pp. 149–163, 2012.
[65] K. Hong, J. R. Barber, M. D. Thouless, and W. Lu, "Effect of power history on pellet-

cladding interaction," *Nucl. Eng. Des.*, 2019.
[66] J. Dundurs, "Discussion on 'Edge-bonded dissimilar orthogonal elastic wedges under normal and shear loading,'" *J. Appl. Mech.*, vol. 36, no. 3, pp. 650–652, 1969.
[67] Y. Rashid, R. Dunham, and R. Montgomery, "Fuel analysis and licensing code: FALCON MOD01," *EPRI Report, 1011308.*, 2004.
[68] J. H. Gittus, "Theoretical analysis of the strains produced in nuclear fuel cladding tubes by the expansion of cracked cylindrical fuel pellets," *Nucl. Eng. Des.*, vol. 18, no. 1, pp. 69–82, 1972.
[69] J. T. A. Roberts, E. Smith, N. Fuhrman, and D. Cubicciotti, "On the pellet-cladding interaction phenomenon," *Nucl. Technol.*, vol. 35, no. 1, pp. 131–144, 1977.
[70] J. C. Wood, B. A. Surette, I. M. London, and J. Barid, "Environmentally induced fracture of Zircaloy by iodine and cesium: the effects of strain rate, localized stresses and temperature," *J. Nucl. Mater.*, vol. 57, no. 2, pp. 155–179, 1975.
[71] H. S. Rosenbaum, R. A. Rand, R. P. Tucker, B. Cheng, R. B. Adamson, J. H. Davies, J. S. Armijo, and S. B. Wisner, "Zirconium-barrier cladding attributes," *Zircon. Nucl. Ind. ASTM Int.*, 1987.
[72] B. Michel, J. Sercombe, G. Thouvenin, and R. Chatelet, "3D fuel cracking modelling in pellet cladding mechanical interaction," *Eng. Fract. Mech.*, vol. 75, no. 11, pp. 3581–3598, 2008.
[73] N. Marchal, C. Campos, and C. Garnier, "Finite element simulation of Pellet-Cladding Interaction (PCI) in nuclear fuel rods," *Comput. Mater. Sci.*, vol. 45, no. 3, pp. 821–826, 2009.
[74] J. Sercombe, I. Aubrun, and C. Nonon, "Power ramped cladding stresses and strains in 3D simulations with burnup-dependent pellet–clad friction," *Nucl. Eng. Des.*, vol. 242, pp. 164–181, 2012.
[75] B. Michel, C. Nonon, J. Sercombe, F. Michel, V. Marelle, C. Nonon, J. Sercombe, F. Michel, and V. M. Simulation, "Simulation of pellet-cladding interaction with the pleiades fuel performance software environment," *Nucl. Technol.*, vol. 182, no. 2, pp. 124–137, 2013.
[76] J. C. Wood, B. A. Surette, I. Aitchison, and W. R. Clendening, "Pellet cladding interaction—evaluation of lubrication by graphite," *J. Nucl. Mater.*, vol. 88, no. 1, pp. 81–94, 1980.
[77] D. Bogy, "Two edge-bonded elastic wedges of different materials and wedge angles under surface tractions," *J. Appl. Mech.*, vol. 38, no. 2, pp. 377–386, 1971.
[78] H. Mogard and N. Kjaer-Pedersen, "A review of Studsvik's international power ramp test projects," *Studsvik AB Atomenergi. Rep. Studsvik-85/6.*, 1985.
[79] M. G. Cooper and B. B. M. and M. M. Yovanovich, "Thermal Contact Conductance," *Int J. Heat Mass Transf.*, vol. 12, no. 3, pp. 279–300, 1969.
[80] J. R. Barber, J. Dundurs, and M. Comninou, "Stability considerations in thermoelastic contact," *J. Appl. Mech.*, vol. 47, no. 4, pp. 871–874, 1980.
[81] M. L. Williams, "Stress singularities resulting from various boundary conditions in angular corners of plates in extension," *J. Appl. Mech.*, vol. 19, no. 4, pp. 526–528, 1952.
[82] C. M. Churchman and D. A. Hills, "General results for complete contacts subject to

oscillatory shear," *J. Mech. Phys. Solids*, vol. 54, no. 6, pp. 1186–1205, 2006.
[83] S. Karuppanan, C. M. Churchman, D. A. Hills, and E. Giner, "Sliding frictional contact between a square block and an elastically similar half-plane," *Eur. J. Mech.*, vol. 27, no. 3, pp. 443–459, 2008.
[84] C. M. Churchman and D. A. Hills, "Slip zone length at the edge of a complete contact," *Int. J. Solids Struct.*, vol. 43, no. 7–8, pp. 2037–2049, 2006.
[85] H. Kim, D. A. Hills, and R. J. H. Paynter, "Asymptotic analysis of an adhered complete contact between elastically dissimilar materials," *J. Strain Anal. Eng. Des.*, vol. 49, no. 8, pp. 607–617, 2014.
[86] E. E. Gdoutos and P. S. Theocaris, "Stress concentrations at the apex of a plane indenter acting on an elastic half plane," *J. Appl. Mech.*, vol. 42, no. 3, pp. 688–692, 1975.
[87] M. Comninou, "Stress singularity at a sharp edge in contact problems with friction," *Zeitschrift für Angew. Math. und Phys. ZAMP*, vol. 27, no. 4, pp. 493–499, 1976.
[88] D. A. Spence, "An eigenvalue problem for elastic contact with finite friction," *Math. Proc. Cambridge Philos. Soc.*, vol. 73, no. 1, pp. 249–268, 1973.
[89] J. R. Barber, M. Davies, and D. A. Hills, "Frictional elastic contact with periodic loading," *Int. J. Solids Struct.*, vol. 48, no. 13, pp. 2041–2047, 2011.
[90] J. Dundurs and M. Comninou, "An educational elasticity problem with friction: Part 1: Loading, and unloading for weak friction," *J. Appl. Mech. Trans. ASME*, vol. 48, no. 4, pp. 841–845, 1981.
[91] J. R. Turner, "The frictional unloading problem on a linear elastic half-space," *IMA J. Appl. Math. (Institute Math. Its Appl.*, vol. 24, no. 4, pp. 439–469, 1979.
[92] D. B. Bogy, "Edge-bonded dissimilar orthogonal elastic wedges under normal and shear loading," *J. Appl. Mech.*, vol. 35, no. 3, pp. 460–466, 1968.
[93] Y. V. Bozhko, A. M. Bolobolichev, A. V. Kostochka, and V. M. Shchavelin, "Coefficient of static friction of the uranium dioxide-zirconium alloy pair under irradiation," *Sov. At. Energy*, vol. 71, no. 5, pp. 945–948, 1991.
[94] V. M. Shchavelin, A. V. Kostochka, A. A. Kuznetsov, I. S. Golovnin, and Y. K. Bibilashvili, "In-reactor study of the friction characteristics of reactor materials," *Sov. At. Energy*, vol. 61, no. 3, pp. 175–178, 1986.
[95] K. A. Grosch, "The relation between the friction and visco-elastic properties of rubber," *Proc. Roy. Soc. Lond. A*, vol. 274, no. 1356, pp. 21–39, 1963.
[96] J. K. Knowles, "The finite anti-plane shear field near the tip of a crack for a class of incompressible elastic solids," *Int. J. Fract.*, vol. 13, no. 5, pp. 611–639, 1977.
[97] P. H. Geubelle and W. G. Knauss, "Finite strains at the tip of a crack in a sheet of hyperelastic material: I. Homogeneous case," *J. Elast.*, vol. 35, no. 1–3, pp. 61–98, 1994.
[98] J. K. Knowles and E. Sternberg, "Large deformations near a tip of an interface-crack between two Neo-Hookean sheets," *J. Elast.*, vol. 13, no. 3, pp. 257–293, 1983.
[99] P. H. Geubelle, "Finite deformation effects in homogeneous and interfacial fracture," *Int. J. Solids Struct.*, vol. 32, no. 6–7, pp. 1003–1016, 1995.